HHS Public Access

Author manuscript

Chem Rev. Author manuscript; available in PMC 2018 January 31.

Published in final edited form as:

Chem Rev. 2015 October 14; 115(19): 10690–10724. doi:10.1021/cr500698d.

Recent Developments in Magnetic Diagnostic Systems

Hakho Lee[1], **Tae-Hyun Shin**[2], **Jinwoo Cheon**[2], and **Ralph Weissleder**[1,3]

[1]Center for Systems Biology, Massachusetts General Hospital, Harvard Medical School, Boston, MA 02114

[2]Department of Chemistry, Yonsei University, Seoul, 120-749, Korea

[3]Department of Systems Biology, Harvard Medical School, Boston, MA 02114

1. Introduction

Rapid point-of-care (POC) diagnostics that enable specific cellular and molecular detection are currently being developed while some have already become clinical reality. These diagnostics are often based on portable, handheld instruments and reagent-containing test kits. Overall, the development has largely been driven by technological advances, medical needs and cost-saving initiatives. For example, POC systems allow care providers to obtain test results quicker[1], which in turn enables immediate clinical management decisions, elimination of costly delays to result in better care. The introduction of POC systems into primary and home care will ultimately preempt unnecessary hospitalization, improve inefficiencies associated with expensive hospital-based medical care and reduce dependence on large, centralized clinics for routine diagnosis.[2, 3] POC technologies are also expected to have major impacts in resource-limited settings and low/middle income countries where access to healthcare is often limited.[4]

POC technologies were first developed to address basic medical needs. Currently available devices include those for blood glucose testing,[5] blood gas and electrolyte analysis,[6] coagulation testing,[2] cardiac marker diagnostics,[7, 8] drug-abuse screening,[9] pregnancy testing,[10] fecal occult blood analysis,[11] hemoglobin diagnostics,[12] cholesterol screening,[13] and limited infectious disease testing.[14, 15] With increasing demands to address more clinical needs, the last few years have seen an explosive growth of different POC sensing approaches[16-19] based on electrical impedance,[20] colorimetric,[21] optical,[22] and magnetic[23-25] sensing strategies. Particularly for cellular, molecular and genetic testings, there remain challenges with many of these techniques. These challenges include further improving sensitivity and specificity, increasing complexity of tests, needs for complicated upfront purification (and possibility of precious sample loss), unique issues associated with low volume testing, higher training needs, higher quality control costs, regulatory burden, and expense.

*Corresponding author: R. Weissleder, MD, PhD, Center for Systems Biology, Massachusetts General Hospital, 185 Cambridge St, CPZN 5206, Boston, MA, 02114, 617-726-8226, rweissleder@mgh.harvard.edu.

RW is a founder and consultant of T2Biosystems. The other authors declare no competing financial interest.

Irrespective of the specific approach, a major limitation to most techniques remains sample purification and enrichment for scarce targets (molecular, genetic, and pathogens). Magnetic sensing offers many advantages as human samples are naturally devoid of ferromagnetic materials (unlike electrical and optical technologies where interferents abound). Magnetic nanoparticles (MNPs) are also extensively used in biomedical separation technologies[26-30] and for imaging[31-34], and are generally innocuous to human cells and other samples. Finally, new generations of miniaturized magnetic detectors have recently become available to utilize advanced magnetic nanomaterials for molecular testing. This article reviews recent advances in such magnetic POC devices, requirements for magnetic materials and advanced conjugation chemistries.

2. POC assay systems using magnetic nanoparticles

Magnetic POC systems exploit the following advantages of MNPs to achieve highly selective and sensitive detection (Fig. 1).

By conjugating affinity ligands onto their surface, MNPs can be used to selectively label biological targets. The binding efficiency is higher than that of single ligand alone, because MNPs offers multiple binding sites.[35]

MNPs can enhance or amplify the analytical signal. By tagging targets with MNPs, one can achieve high contrast against the background, which leads to higher detection sensitivities.[36] In nuclear magnetic resonance (NMR) detection where the relaxation of ^{1}H protons is measured, each MNP influences millions of surrounding water molecules, a most effective amplification strategy.[23]

MNPs facilitate selective manipulation and sorting of targets, as only MNP-labeled targets will respond to the external magnetic field and experience mechanical force. This principle is extensively used in MNP-based cell sorting and enrichment.

This section reviews various MNP-based bioassay systems. We broadly categorized them as magnetic sensors and actuators, according to their primary use of MNPs, and discuss representative examples in each category.

2.1. Magnetic detection

Signals from MNP-labeled biological objects are often measured by magnetometers.[37] Based on the detection mechanism, magnetometers can be categorized into volumetric or surface-based sensors.[38] The volumetric sensors measure analytical signals coming from the entire detection volume, which makes assays simple and fast. The sensors' resolving power, however, can be restricted, because the acquired signal is an ensemble average of the whole volume. Representative examples of volumetric sensors include NMR devices, magnetic susceptometors, and conventional superconducting-quantum-interference-devices (SQUIDs). Surface-based sensors directly detect individual magnetic objects near the sensing elements. These sensors generally achieve higher sensitivity and finer resolution than volumetric ones, but target samples should be placed in close proximity of the sensor surface. Such an arrangement limits the assay configuration, and typically causes the assays to be more time-

consuming. To date, many different types of magnetometers (*e.g.*, magnetoresistance sensors, Hall effect sensors) have been developed as surface-based biosensors.

2.1.1. MicroNMR (μNMR) system—NMR detects MNP-labeled targets by measuring ^{1}H proton signal. The local dipole fields generated by MNPs perturb the precession of nuclear spins in water protons. Samples containing MNP-labeled targets thus display faster signal decay (higher transverse relaxation rate) than non-targeted samples (Fig. 2a).[39] Because each MNP can affect large number of its surrounding water molecules, NMR-based detection benefits from an intrinsic signal amplification to achieve high detection sensitivity.[23]

Significant progresses have been made towards miniaturizing NMR detection systems for POC diagnostics. These advancements include designing new NMR grade magnets,[40] miniaturizing NMR electronics into integrated circuit (IC) chips,[41], and implementing smaller NMR coils.[42-44] These miniaturized microNMR (μNMR) systems are not only portable, but also display higher sensitivity than conventional systems. Figure 2b shows a recently developed μNMR system (Fig. 2b) optimized for clinical operations.[45] The system used disposable tubes (diameter, 1.2 mm) as a sample container to prevent system contamination and to facilitate the sample-loading (Fig. 2c). The NMR electronics could be programmed to execute many different pulse sequences (Fig. 2d). In particular, the system can automatically compensate for drifts in the NMR frequency caused by temperature fluctuations, which enabled robust NMR detection. This system has been used in many clinical trials, detecting various biological entities, including tumor cells,[16, 46, 47] pathogens,[48-52], and extracellular vesicles.[43, 53]

2.1.2. Magnetic susceptometers—Magnetic susceptometers measures the responses of MNPs exposed to alternating-current (AC) magnetic field. The most-widely used sensing scheme is to detect Brownian relaxation of MNPs.[54, 55] MNPs in solution undergo thermal rotation with a timescale (τ_B) that scales with the particle's hydrodynamic volume (see Section 3.4 for details). This thermal motion affects the AC magnetic susceptibility (χ) of the MNPs. Specifically, the quadrature component of χ, which has 90° phase difference with respect to the AC field, has its maximum value when the excitation frequency is equal to $1/\tau_B$. Changes in the hydrodynamic diameter, due to target binding to MNPS, would shift the peak position. Compared to the μNMR that requires a highly uniform magnetic field, the magnetic susceptometry could be performed with a simpler setup. For example, Park *et al.* implemented a compact magnetic susceptometer to measure Brownian relaxation of MNPs (Fig. 3a).[56] The magnetic susceptometry, however, has lower sensitivity than the μNMR, as the sensing lacks the inherent signal amplification mechanism.

Magnetic susceptometry has been used to detect various biological targets, such as soluble proteins,[57] DNA,[55] and bacteria[58] with signals measured either by induction coils or SQUID under AC magnetic field excitation. By using AC magnetic susceptibility as a unique signature, the device could differentiate multiple types of MNPs based on their different hydrodynamic size (Fig. 3b).

2.1.3. Magnetoresistance sensors—Magnetoresistance sensors detect their changes in electrical resistance when exposed to external magnetic fields. The most widely used magnetoresistance sensor type is the giant magnetoresistance (GMR) magnetometer. The GMR effect is caused by the electron spin-dependent scattering of conduction electrons in magnetic layers.[59] The phenomenon occurs in an artificial magnetic structure comprising multiple layers of ferromagnetic and non-magnetic materials (Fig. 4a). External magnetic fields change the relative angle between layers' magnetizations. Accordingly, electrons passing through the layers experience a different level of scattering (Fig. 4b). For biosensor applications, GMR sensors are typically used in association with a sandwich assay format, wherein molecular targets are immobilized on the sensor surface and labeled with magnetic probes.

The initial GMR biosensor used micrometer-sized magnetic beads as a probe.[60] However, the considerable size disparity between the probes and the molecular targets was a limiting factor in the assay speed and sensitivity.[61] The use of MNPs helped overcome such limitations and enabled sensitive detection of low amounts of proteins.[25, 61, 62] Furthermore, GMR sensor arrays, with each sensor functionalized with different antibodies, were developed for parallel detection. These sensors achieved the detection limit of ~50 aM), and displayed high dynamic ranges.[25] To provide massively parallel sensing, a hybrid GMR sensor was recently constructed by juxtaposing two different chips: a 256 GMR array and a complementary metal-oxide-semiconductor (CMOS) chip for signal processing (Fig. 4c).[59] Compared to other magnetic detectors, GMR sensors are usually more difficult to implement, as they require specialized magnetic wafers.

2.1.4. MicroHall (μHall) sensors—When a current-carrying electrical conductor is placed in a magnetic field, a voltage difference is developed across the conductor, transverse to the current direction. This phenomenon, called the classical Hall effect, is caused by the accumulation of the moving charges to the sides of the conductor. Compared to MR-bases sensors, the Hall-effect sensors have a lower magnetic-field sensitivity. However, they display an excellent signal linearity at high magnetic fields (>2 T) that can fully magnetize MNPs. Furthermore, the sensor fabrication is compatible with CMOS processing, which enables on-chip integration of a large array of Hall sensors and other auxiliary electronics. Various types of micrometer-scale Hall (microHall; μHall) sensors have been developed and applied for molecular detection.[63-66] Gambini *et al.* advanced this technology by developing a large (64 × 160) sensor array via CMOS technology (Fig. 5a).[67] The chip also contained a signal processing circuit and micro-electromagnets to temporarily magnetize magnetic beads (Fig. 5b). The system measured the remnant magnetic field (B_{bead}) coming from the beads immediately after the polarizing magnetization field (B_0) was switchedoff (Fig. 5c).[68] In this way, the weak B_{bead} from the magnetic beads could be distinguished from much stronger B_0 (10^2 to 10^5 times larger). In a titration experiment with magnetic beads (Dynabead M280, Invitrogen), the sensor showed the resolution of 25 particles per array, which was equivalent to a 0.1% coverage of the sensing area (0.64 mm^2).[67]

More recently, Issadore *et al.* introduced a new μHall system that can profile cells in a flow condition (magnetocytometry).[24, 69] The sensor detected magnetic fields from MNP-labeled cells. The measured Hall voltage (V_H) was proportional to the MNP numbers per cell, which

in turn enabled quantitative molecular profiling (Fig. 5d). For a given number of MNP, the detection sensitivity improved by using MNPs with high magnetic moments (*e.g.*, doped ferrite, Fe-based particles). Because the sensor measured time-varying signals from flowing cells, it could operate in the AC-coupling mode to block interference from the static external magnetic field (B_0). In addition, eight 8 × 8 μm^2 Hall elements were laid out as an overlapping 2 × 4 array (Fig. 5e). This arrangement ensured that cells inside the fluidic channel would be detected by at least two Hall sensors to improve the accuracy.[24] When cancer cells were profiled for surface markers, the μHall results agreed well with those from flow cytometry (Fig. 5f). The μHall detection, however, did not require washing or purification steps, and could be performed in complex biological media. With such a capacity, the μHall was ideally suited to detect rare cells in native biological samples. For example, the μHall was able to detect circulating tumor cells in cancer patient blood samples, even in those tested negative with clinical standards (CellSearch).[24]

2.1.5. Diamond magnetometer—Magnetometry based on nitrogen-vacancy (N-*V*) center diamonds is an emerging new technology for ultrasensitive magnetic detection.[70-73] The N-*V* center is an association of a nitrogen atom and a vacancy inside a diamond crystal lattice (Fig. 6a). The center has a ground-state energy with spin-triplet (m_S = 0 and ±1). The m_S = 0 state spontaneously split from m_S = ±1 (zero-field splitting) state, with an energy difference of 2.87 GHz. In the presence of external magnetic fields, the energy levels of m_S = ±1 would further split according to Zeeman effects (Fig. 6b). The energy differences between m_S = ±1 and m_S = 0 can be measured spectroscopically to determine the strength of external magnetic fields.

One readout method is based on continuous optical and microwave excitation.[74] In this approach, a N-*V* system is optically polarized, through 532 nm excitation, into the excited state of m_S = 0; the spontaneous decay of m_S = 0 level from the excited to the ground states generates red fluorescence. A concurrent microwave excitation can induce transition from m_S = 0 to m_S = ±1 at the ground state, and the fluorescence intensity decreases as fewer m_S = 0 spins are available. By measuring the florescent intensity at sweeping microwave frequency, the relative change of m_S = 0 population can be measured. Without external magnetic fields, only a single dip in the fluorescence intensity is observed due to m_S = ±1 degeneracy. With external magnetic fields on, the Zeeman effect removes the degeneracy, and splits the single dip into two; the inter-dip distance is linearly proportional to the field strength (Fig. 6c).

N-*V* diamonds could be an excellent biosensing platform. They assume ultrahigh detection sensitivity (3 nT/√Hz)[71], and yet operate at ambient conditions. In addition, standard microscopy is used for signal acquisition, offering a possibility for wide-field imaging. For example, Sage *et al.* used a N-*V* sensor to magnetically image magnetotactic bacteria (Fig. 6d).[75] Magnetic fields, coming from chains of magnetosomes inside the bacteria, were measured, and their vector maps were generated at a sub-cellular resolution (400 nm). More recently, N-*V* diamond sensors have also been adopted as a NMR reader.[76, 77] The sensor demonstrated exquisite sensitivity, detecting NMR signal from 10^4 nuclear spins from nanometer scale samples.[77]

2.2. Magnetic actuation

Magnetic actuation uses MNPs as a remote handle to exert mechanical forces on target objects. As in magnetic detection, the operation is highly selective even in complex, turbid samples[29], due to the inherently negligible magnetic susceptibility of biological objects, and can be performed in a parallel and high-throughput fashion.[28, 78] Furthermore, by employing microfabrication, magnetic actuators can be integrated with sensing elements into an easy-to-use, microfluidic cartridge.[79, 80]

Biological objects labeled with MNPs assume induced the magnetic moment (**m**) when subjected to external magnetic fields. The magnetic force $\mathbf{F_m}$ due to the external magnetic field induction $\mathbf{B_0}$ is given as[81]

$$\mathbf{F_m} = \frac{1}{2}\nabla(\mathbf{m}\cdot\mathbf{B}_0). \quad (1)$$

For an ensemble of MNPs, the induced magnetic moment can be expressed as $\mathbf{m} = nV\chi_0\mathbf{B_0}/\mu_0$, where n is the particle number, V is the particle volume, χ_0 is the volume magnetic susceptibility, and μ_0 is the vacuum permeability (see Section 3.3 for details). Eq. 1 can be rewritten as

$$\mathbf{F_m} = \frac{nV\chi_0}{\mu_0}(\mathbf{B}_0\cdot\nabla)\mathbf{B}_0. \quad (2)$$

The force magnitude ($F_m = |\mathbf{F_m}|$) therefore can be increased by using MNPs with strong magnetization (hence large χ_0) and optimizing their labeling methods (large n); this topic is further discussed in Sections 4. On the device level, F_m is enhanced by designing magnetic structures that can generate strong (large B_0) as well as highly localized magnetic fields (large ∇B_0).

Various types of micro-magnetic structures have been developed and integrated with microfluidic systems to improve the efficiency of magnetic actuation.[26, 82, 83] For example, lithographically-patterned magnets that consist of either ferromagnetic elements[84-90] (*e.g.*, Ni or Permalloy) or electromagnets[79, 81, 91-93] have been implemented. These micrometer-scale structures are ideal in producing highly localized magnetic fields ($\nabla B_0 \sim 100$ T m^{-1}), and the resulting magnetic forces can be large enough (100 pN to 10 nN on 1 μm magnetic beads) to enable high-throughput sorting.[88]

We discuss two major modes of magnetic actuation in the following section: magnetic separation and magnetic manipulation. Magnetic separation refers to the sorting operation that identifies and collects target objects, whereas magnetic manipulation actuates the precise spatial and temporal control of target objects.

2.2.1. Magnetic separation system—Magnetic separation can be an efficient preparatory tool to enrich biological targets from heterogeneous mixtures.[94] According to their operation modes, the separation systems can be further grouped as a retention device or an in-flow filter device.[26] In the retention device, magnetically-labeled targets are captured and kept in designated areas, while the rest of samples are separated and removed; the captured targets can be subsequently retrieved by removing the external magnetic field. In the in-flow device, spatial trajectories of magnetically-labeled targets are deflected through the application of external magnetic fields, and targets are eventually collected in separate fluidic ports. The retention-based separation is generally fast and easy to operate, although care should be taken not to overwhelm the separation capacity of the device. In contrast, the in-flow filtration can process a large volume of samples without being saturated. The device implementation and operation, however, often require a more sophisticated and balanced coordination between the fluidic flow and the magnetic force.

2.2.1.1. Retention device: Retention devices can generate large magnetic forces to securely capture targets against the flow. As such, magnets are designed to create short-ranged, large-gradient fields. For example, Tibbe *et al.* used a combination of macro and microscopic magnets to capture individual cells.[90] The device had a two-stage magnet system consisting of a pair of external magnets and a lithographically-patterned array of Ni lines (Fig. 7a). The external magnets had a wedge-shape to produce a field gradient in the vertical direction. The Ni lines were magnetized by the uniform horizontal field from the external magnets, and produced highly localized magnetic field on the device surface. MNP-labeled cells in the sample chamber would migrate upwards due to the global field gradient by the external magnets. When close to the device surface, these cells were trapped between the Ni-lines where the magnetic field flux is highly concentrated. As the captured cells aligned along the interstitial space of Ni-lines, they could be easily observed by optical systems (Fig. 7b). Indeed, the device was further integrated with a translation stage and a compact-disk optics to enable multiplexed single-cell analyses in whole blood.[90, 95]

High magnetic field gradient can also be achieved through the alternating arrangement of magnetic dipoles (Fig. 7c).[96, 97] This configuration creates near fields with their maxima tightly confined on top of each dipole. Analytical modeling[98] showed that the field is indeed short-ranged, decaying exponentially away from the dipoles. The leading term in the field magnitude is written as

$$B \approx B_d e^{\frac{2\sqrt{2}\pi}{a}|z|} \left| \cos\frac{2\pi}{a}x \cdot \cos\frac{2\pi}{a}y \right|, \quad (3)$$

where a is the pitch between adjacent dipoles and B_d is the field from a single dipole. Eq. 3 also shows that the effective distance [$\sim a/(2^{1.5}\cdot\pi)$] that the field extends from a dipole can be engineered for specific applications simply by controlling a. Issadore *et al.* used a magnetic self-assembly to create the desired dipole arrangement (Fig. 7d): permanently magnetized materials tend to form antiparallel configuration of moments to minimize magnetic energy. Specifically, NdFeB grains were suspended polydimethylsiloxane (PDMS) polymer, and the

mixture was slowly cured (~1 hour) to allow for the self-assembly of the NdFeB grains. A microfluidic channel (height: 50 μm) was then directly built on top of the cured magnets (Fig. 7e).[97] The device had two magnetic sections for efficient magnetic capture. At the entry port, the magnetic layer was made of bigger NdFeB particles ($a \approx 125$ μm). This layer thus created a magnetic field that extended throughout the microfluidic channel height. Further along the channel, the grain size was reduced ($a \approx 8$ μm) to firmly trap magnetic objects. The device was used to enrich circulating tumor cells in blood by immunomagnetically depleting leukocytes (Fig. 7f). The operation enriched the population of tumor cells to leukocytes by a factor of $>10^3$. The recovery ratio, the fraction of tumor cells that pass through the system, was ~90 %.

2.2.1.2. In-flow separation device: In-flow separation is achieved by applying magnetic fields, typically perpendicular to the direction of the fluidic flow.[82, 99] The magnetic force changes the trajectories of magnetically-labelled targets along the stream lines, continuously separating target objects from others whose trajectories remain unaffected. This scheme has a less stringent requirement for high field gradients, a necessity in the retention systems, and potentially affords higher throughput operation. The device by Inglis *et al.* used microfabricated Ni-lines for cell separation.[86] Unlike the trapping system (Fig. 7a), the Ni-lines were aligned at an angle θ to the flow direction. The net force on a magnetic object is the vector sum of the magnetic force ($\mathbf{F_m}$) and the drag force ($\mathbf{F_d}$; Fig. 8a). If the $\mathbf{F_d}$ component perpendicular to the Ni lines is smaller than $|\mathbf{F_m}|$, the object will flow along the Ni lines, altering its direction in flow.[89] The criterion for such events is $|\mathbf{F_d}| \cdot \sin\theta < |\mathbf{F_m}|$; balanced control on the fluidic flow is thus important. This device was used to separate MNP-labeled leukocytes from whole blood (Fig. 8b). The concept has been further extended for differential sorting[88]. With a set of magnetic wires, each inclined at a different angle θ, multiple targets could be sorted according to their magnetic moments.

By using Y-shaped fluidic devices, samples can be separated without touching the magnetic structures. These devices have separate fluidic ports for introducing the sample and buffer solution; flow injection generates two laminar streams inside the fluidic channel. The magnets are located on the buffer side to pull MNP-labeled targets and collect them on the buffer outlet. As the magnets are detached from the fluidics, the system is easy to manufacture and cost-effective. The magnetic force can also be controlled *in situ* by changing the magnet position. Extending from this simple design, Kang *et al.* developed a blood-cleansing system that removed MNP-labeled pathogens from blood (Fig. 8c).[100] This fluidic system mimicked the architecture of a spleen, consisting of two fluidic channels interconnected with a series of open slits: one channel functioned as an arterial vessel for blood flow, and the other contained slow-flow saline buffer, acting like venous sinusoids. Bacteria targets were labeled by MNPs conjugated with an engineered human opsonin (mannose-binding lectin) that captures a broad range of pathogens (Fig. 8c, **inset**). Under a continuous flow, MNP-labeled bacteria were removed into the venous channel through the magnetic pulling. The device achieved a high separation efficiency (>90%) with the flow rate reaching up to 1.25 liter per hour.

2.2.2. Magnetic manipulation system—Magnetic manipulation is an elegant micro-manipulation strategy to transport single cells or other small objects to desired locations through dynamic control of the magnetic fields. Lithographically patterned electromagnets are widely used as a field source, and can provide fine spatiotemporal resolution in field control. A planar coil is the most efficient geometry, as it can concentrate the magnetic flux. The field strength produced by electromagnets, however, is much weaker than that by permanent magnets. Most magnetic manipulation is thus performed under static conditions, *i.e.*, without flow.

Several different types of devices have been reported for magnetic manipulation.[79, 81, 85, 91, 101] In particular, advanced IC chips have been developed by applying the CMOS technology in device fabrication. For example, Dupont *et al.* implemented a linear array of microcoils integrated with optical detectors (single photon avalanche diodes) at the center of each coil, which allowed for on-chip manipulation and detection of individual magnetic particles (Fig. 9a).[80] Lee *et al.* implemented an IC chip containing a matrix of microcoils, current sources and control electronics (Fig. 9b); the device was used to control the motion of individual biological cells with microscopic resolution.[102]

Fluidic droplets represent another technology used for magnetic manipulation. In this strategy, droplets are formed by encapsulating aqueous solution of MNPs in mineral oil. Magnetic particles serve a dual function, both as a force mediator and a solid substrate for biochemical reaction. By using a two-dimensional microcoil array, implemented in a printed circuit board, Lehmann *et al.* moved a droplet through a sequence of buffer solutions to purify DNA from cell lysates.[103] Pipper *et al.* introduced a POC device for avian flu detection (Fig. 9c), by combining magnetic actuation with on-chip polymerase chain reaction (PCR).[104] In this system, the magnetic droplets were manipulated by moving the permanent magnet. Sequential processes were performed on-chip, including viral RNA isolation, purification, pro-concentration, and further amplification through real-time reverse transcription PCR (RT-PCR). Because of the small sample volume (<50 μL), the assay benefited from fast diffusion and low thermal mass, enabling the entire procedure to be completed in less than 30 min.

Magnetic manipulation was also employed to perform key steps in diagnostic assays.[105-107] For example, the Magnetotech sensor (Philips) used magnetic actuation to speed up immunomagnetic detection (Fig. 9d).[108] In this system, a pair of electromagnets sandwiched a microfluidic cartridge whose surface was functionalized with antibodies. Samples and immunomagnetic particles were mixed and injected to the cartridge. Activating the bottom electromagnet concentrated magnetic particles to the sensor surface, accelerating their binding kinetics to the surface. Subsequently, the top electromagnet was turned on to remove free and non-specifically bound particles (magnetic wash). The final particle-binding to surface was optically readout through reflection measurements.

3. Key Magnetic properties of magnetic nanoparticles

Table 1 compares key magnetic properties required for different detection modalities. The most important MNP property is the magnetic moment (m_p). The utilities of MNPs are

generally commensurate with their magnetic moment (m_p), because higher m_p can result in larger force and more pronounced detection signals. m_p is a product of the magnetization (M) and the particle volume (V). Significant efforts thus have been made to synthesize large MNPs using magnetically stronger materials.

3.1. Saturation magnetization

When a magnetic material has n_d atomic magnetic dipoles per unit volume and each dipole has the magnetic moment m_d, the saturation magnetization M_0 is defined as $M_0 = n_d m_d$. This value is an unique material property, and sets a maximum M achievable for a given magnetic material. Table 1 lists the bulk M_0 values of representative magnetic crystals.[109] Element iron, cobalt or doped-ferrite are the most widely-used MNP constituents, as the material assumes high M_0 and can be synthesized into MNPs. Magnetization of MNPs increases with particle size, because the surface effect (e.g., spin-canting) is reduced in larger particles (Fig. 10a). The saturation magnetization of MNPs, however, is generally smaller than that of bulk material, since the high surface energy of MNPs can hinder the perfect alignment of atomic magnetic dipoles.[110, 111] For a spherical MNP, its saturation magnetization (M_p) can be estimated as $M_p = M_0 \cdot [(r - \Delta)/r]^3$, where M_0 is the saturation magnetization of the bulk material, r is the particle radius, and Δ is the thickness of magnetically frustrated (spin-canting) surface layer.[112] The surface effect can be reduced by modifying the particle shape. For example, cube-shaped MNPs were shown to have larger M_p than spherical ones with the same magnetic volume, because more magnetic dipoles can align parallel in the cubic geometry (Fig. 10b).[113, 114]

3.2. Superparamagnetism

A unique feature of MNPs is the paramagnetic behavior of an ensemble of MNPs, termed superparamagnetism.[115] Individual MNPs have a single magnetic domain with the magnetization aligned in a particular direction defined by magnetic anisotropy. However, thermal energy can activate the random reversal of magnetization over the anisotropy barrier.[116] Without external magnetic fields, an ensemble of MNPs consequently display negligible remnant magnetic moments, but the magnetic moments grow with increasing external magnetic fields. This property is critical both in magnetic sensing and actuation, as (i) MNPs can be stably suspended in solution without aggregation to enhance their labeling efficiency, and (ii) MNP-labeled biological targets, once collected by external magnets, can be released by removing the external fields.

The superparamagnetism is highly dependent on the particle size. When the external magnetic field is removed, the average magnetic moment of a MNP relaxes to zero through thermal fluctuation. The corresponding relaxation time (τ_N) is estimated by the Néel-Brown model,[117]

$$\tau_N = \tau_0 \exp \frac{K \cdot V}{k_B T}, \quad (4)$$

where τ_0 is a time factor in the order of 10^{-9} sec, K is the anisotropy energy constant of the material, k_B is the Boltzmann constant, and T is the temperature. MNPs are considered superparamagnetic when $\tau_N < 10^2$ sec at room temperature, and this condition sets the maximum particle size ($V = 25\ k_B \cdot T/K$) for superparamagnetism (Table 1).[118] These values, however, represent a general guideline, as many factors can affect the relaxation behavior of MNPs. For examples, the anisotropy energy constant is affected by the particle size and shape[114, 119]; magnetic interaction among particles could lock their magnetic moments; and electrical charges on the particle surface can exert repulsive force to effectively increase the inter-particle distance. Importantly, MNPs in suspension can lose their effective moment through another route, the Brownian relaxation. For a particle with a hydrodynamic volume V_h, the Brownian relaxation time is given by

$$\tau_B = \frac{3\eta V_h}{k_B T}, \quad (5)$$

where η is the fluid viscosity.[54] Since the magnetic moments can relax through either of these independent mechanisms, the effective relaxation rate is given as $1/\tau_N + 1/\tau_B$. The effective relaxation time (τ) of MNPs is therefore[120]

$$\tau = \frac{\tau_N \cdot \tau_B}{\tau_N + \tau_B}. \quad (6)$$

Note that for $\tau \approx \tau_B$ for larger MNPs, as τ_N is increasing more rapidly than τ_B with the particle size (Fig. 11a).

3.3. Average magnetic moment

At a given temperature and under an external magnetic induction field (B_0), the magnetization of superparamagnetic MNPs can be expressed using the Langevin function[115]

$$M_{\text{avg}} = M_p \left[\coth\left(\frac{M_p V \cdot B_0}{k_B T}\right) - \left(\frac{M_p V \cdot B_0}{k_B T}\right)^{-1} \right]. \quad (7)$$

For a MNP population with a size distribution $f(r)$, the magnetic moment of MNPs is obtained through a size-weighted ensemble averaging:[121]

$$m_{\text{avg}} = \left[\int_0^\infty M_{\text{avg}} V \cdot f(r) dr\right] / \left[\int_0^\infty f(r) dr\right]. \quad (8)$$

At low external magnetic fields (≤ 0.1 T), the magnetization of MNPs is linearly proportional to the external fields. The direct-current (DC) volume magnetic susceptibility χ_0 for a monodisperse MNPs is given as

$$\chi_0 = \frac{\mu_0 M_{\mathrm{avg}}}{B_0}\Big|_{B_0 \to 0} = \frac{\mu_0 M_{\mathrm{avg}}^2 V}{3 k_B T}, \quad (9)$$

where μ_0 is the magnetic permeability of vacuum. For a MNP population, χ_{avg} is obtained by ensemble-averaging χ_0.

3.4. AC magnetic susceptibility

When subjected to alternating current (AC) magnetic fields, MNPs may show delayed response due to the finite rate of magnetization changes. This property can be modeled by a complex magnetic susceptibility, $\chi = \chi' + i\chi''$, where χ' and χ'' respectively denote the in-phase and the out-of-phase components with respect to the AC field. For MNPs with the DC susceptibility of χ_0 and the effective relaxation time τ,[54]

$$\chi' = \frac{\chi_0}{1 + (\omega\tau)^2}, \quad (10)$$

and

$$\chi'' = \frac{\chi_0 \cdot \omega\tau}{1 + (\omega\tau)^2}, \quad (11)$$

where ω is the frequency of the applied field (Fig. 11b). Note that χ'' has its maximum when $\omega = \tau^{-1}$; the shift in the peak frequency thus can be exploited to measure specific binding of target molecules to MNPs (**Section 2.1.2**).

The out-of-phase component χ'' also has significant implications in magnetic fluid hypothermia, as it represents the energy loss through magnetic relaxation. With the external field strength H_0, the specific loss power (P) for monodisperse MNPs is given by[122]

$$P = \frac{1}{2}\mu_0 H_0^2 \chi'' \omega. \quad (12)$$

To achieve maximum heating, MNPs should be monodisperse at the optimum particle size, satisfying $\omega = \tau^{-1}$.

3.5. Relaxivity

In NMR-based sensing, ideal properties of MNPs are better represented by relaxivity. When placed in an external field, each MNP creates a local magnetic field, which efficiently destroys the coherence in the spin-spin relaxation of water protons. The net effect is a shortening of the longitudinal (T_1, spin-lattice) and transverse (T_2, spin-spin) relaxation of NMR signal.[123, 124] The capacities of MNPs to decrease T_2 and T_1 are respectively defined as the transverse (r_2) and the longitudinal (r_1) relaxivities. MNPs are mainly used as a T_2-modulating agent, because $r_2 \geqq r_1$.[125] MNPs with higher r_2 are desirable to improve the detection sensitivity.

The r_2 values increase with the particle size (r) and the magnetization (M_p). The relationship, however, follows a different scaling law, depending on the particle size. When particles are small (e.g., $r < 13$ nm for $MnFe_2O_4$ MNPs at the NMR frequency 20 MHz), the diffusional motion of water molecules is fast enough to average out the magnetic fields produced by MNPs. In this regime, called motional averaging, the r_2 value (per metal) is proportional to $M_p^2 \cdot \tau_d$.[126] With $\tau_d \sim r^2/D$, where D is the diffusion coefficient, τ_d signifies the duration when water protons are under the influence of a MNP. As τ_d increases further with growing particle size, the averaging effect diminishes and MNPs appear to water protons as randomly-distributed, stationary objects.[127] The corresponding relaxation mechanism, known as static dephasing, predicts that r_2 relaxivity is only proportional to M_p.

Figure 11c shows the measured r_2 values of $MnFe_2O_4$ MNPs.[128] With increasing particle size, the observed r_2 increased as predicted by the motional averaging relaxation. Further improving r_2 in a single-core particle format, however, turned out challenging, as the particles became non-superparamagnetic and no longer stable in suspension. Yoon *et al.* took an alternative approach by assembling small MNPs into a single multicore particle.[128] Such a configuration, akin to that of magnetic beads, allowed particles to remain superparamagnetic, while further increasing r_2 through the static dephasing relaxation mechanism. Indeed, the r_2 values of multicore particles were higher than those of single-core MNPs, and could be fitted to the static dephasing model.

4. Synthesis of Core magnetic nanoparticles

Typically consisting of a surface coating and versatile targeting molecules at the surface, the magnetic properties of MNPs are dictated by their core magnetic materials (Fig. 12a). Cores can be produced from different materials and have a controlled size, shape, and crystallinity.[37, 129-133] Generally, core MNPs are either made of pure metals (*e.g.*, Co, Fe, and Ni)[134-139] or their oxides.[134, 140-142] Transition metal-doped oxides and metal alloys, including $CoPt_3$, FePt, and FeCo, are also good candidates.[143-148] Among this variety of core MNP libraries, iron-based MNPs are considered to be one of the most attractive candidates for biological application, owing to their biocompatibility.[133, 149] In particular, iron oxide MNPs are degraded into non-toxic iron and oxygen components, and their utilization as magnetic resonance imaging (MRI) contrast agents had been approved by the US Food and Drug Administration (FDA) and the European Medicines Agency (EMA) at different time points.[150-155] In this section, representative core MNPs, including ferrite-based MNPs, elemental

iron-based MNPs, and iron-based bimetallic alloy MNPs and their synthetic methods, will be discussed.

4.1. Ferrite-based MNPs

Ferrites are complex magnetic oxides derived from iron oxides, such as magnetite (Fe_3O_4) and maghemite (γ-Fe_2O_3), that are chemically combined with one or more metallic elements.[156] The ferrites have a general composition of MFe_2O_4, where M is a divalent transition metal cation, such as Co, Mn, Fe, Ni, and Zn. Ferrite MNPs can be produced by either physical top-down approaches or chemical bottom-up strategies.[157, 158] However, the latter are more adequate for producing high-quality MNPs with a controlled size distribution and uniform composition.[132, 158, 159] A variety of colloidal chemical methods, including co-precipitation, thermal decomposition, micelle synthesis, hydrothermal synthesis, and electrochemical synthesis, are directed at the fabrication of MNPs.[159] This section will focus on the co-precipitation and thermal decomposition synthesis because they are the most relevant method for preparing MNPs for POC devices. The former results in biocompatible MNPs for *in vivo* use, and the latter results in highly monodisperse MNPs with high magnetic properties, which are generally used for *in vitro* applications. Other synthetic methods have been thoroughly reviewed by Laurent *et al.*[159]

4.1.1. Co-precipitation method—Ferrite MNPs are commonly synthesized by the co-precipitation of stoichiometric amounts of ferrous (Fe^{2+}) and ferric (Fe^{3+}) salts in an alkaline solution. This technique is usually performed in the presence of water-soluble surface coating materials, such as dextran,[160] starch,[161] polyethylene glycol (PEG),[162] polyacrylic acid (PAA),[163] or polyvinyl alcohol (PVA),[164] to provide colloidal stability and biocompatibility *in situ*. During this reaction, MNPs are formed by sequential reaction steps, including monomer generation, nucleation, and growth (Fig. 12b). According to the LaMer mechanism, a short burst of nucleation followed by a slow growth of particles without any significant additional nucleation is required to produce monodisperse ferrite MNPs.[165] Therefore, optimizing the reaction conditions to achieve a complete separation of the nucleation and growth process is critical for generating high-quality MNPs.[166] In co-precipitation synthesis, the reaction can be controlled by adjusting parameters, such as the pH, ionic strength, temperature, types of the iron salts, and $[Fe^{2+}]/[Fe^{3+}]$ ratio. The influences of these parameters on the size and magnetic properties of MNPs have been extensively explored in a number of studies.[167-171] However, MNPs synthesized by co-precipitation usually have a large size distribution because the growth of crystal is only governed by kinetic factors (Fig. 12c).[159]

One unique ferrite MNP, synthesized by co-precipitation method, is monocrystalline iron oxide nanoparticle (MION), which consists of a 3–5 nm magnetite and/or maghemite core surrounded by a biocompatible surface coating material (*i.e.*, dextran).[172] MIONs are synthesized following the addition of concentrated base to an aqueous mixture of di- and trivalent iron chloride salts and dextran. The overall average hydrodynamic size of the MIONs usually falls within the 20–45 nm range. Owing to the biocompatible nature of ferrite and dextran surface coating and adequate hydrodynamic size, MIONs are widely utilized as a platform material for POC diagnostics.[160, 172, 173] Several variations of mono-

or polycrystalline iron oxides have been used as MRI contrast agents (*e.g.*, Feridex I.V.®, Combidex®, and Resovist®; though FDA-approved, some of these products have been withdrawn from the market for commercial reasons).[150-154, 174, 175] In the case of one specific MION-46, the core size is ~4.6 nm, saturation magnetization value is ~68 emu g^{-1}; r_1 and r_2 are 16.5 $mM^{-1}s^{-1}$ and 34.8 $mM^{-1}s^{-1}$ ([Fe], 0.47 T, 37 °C), respectively.[172] Therefore, MIONs generate negative (T_2) contrast by decreasing the MRI signal of the target lesion, and they can be effectively used to image reticuloendothelial system organs, such as the liver and spleen.

However, these ferrite MNPs suffer from dissociation of the surface coating materials under certain biological conditions because of the weaker non-covalent binding interaction between the core ferrite and dextran coating. To prevent such coating dissociation, MIONs are further treated with chemical compounds that promote covalent cross-linkages between surface dextrans.[160, 176-181] Epichlorohydrin is often used as a cross-linker. Upon treatment with base, the hydroxyl groups of dextran are deprotonated into their anions, which act as nucleophiles in an S_N2 reaction with epichlorohydrin. Each epichlorohydrin molecule can react with two molecules of dextran, first by S_N2 displacement of the chloride ion and then by a base-catalyzed epoxide ring opening reaction. These reactions finally result in cross-linked iron oxide nanoparticles (CLIOs). Followed by treatment with ammonia, primary amine functional groups are easily introduced viaopening of the unreacted oxirane ring of epichlorohydrin. The primary amines on the surface of the nanoparticle endow CLIOs with an increased capacity for the conjugation of multiple targeting molecules, additional imaging agents, and therapeutics.[182] Amine-terminated CLIOs (CLIO-NH_2) have an average hydrodynamic size of 25–40 nm, approximately 40–80 amines per nanoparticle, and a r_2 of 50 $mM^{-1}s^{-1}$ [Fe].[160, 176] Their unique coating makes CLIOs biocompatible and exceedingly robust for use in many bio-medical applications.[182] More recently, alternative carboxymethyl dextran has been used for MION coating because its multiple carboxyl groups exhibit enhanced binding to the surfaces of the MNPs, which results in much higher coating stability. An example of an FDA-approved clinical preparation to treat iron deficiency is ferumoxyol (Feraheme®), and which can also be used for MR imaging.[34, 153]

4.1.2. Non-hydrolytic thermal decomposition method—Although ferrite MNPs fabricated by the co-precipitation method are primarily used for *in vivo* imaging, the larger size distribution and poor crystallinity are a limitation for their use in POC devices.[183] As a result, non-hydrolytic thermal decompositions methods have been developed. In general, ferrite MNPs synthesized by different non-hydrolytic routes have excellent crystallinity and homogenous size distribution and shape (Fig. 12c).[119, 141, 143, 184-186]

Two different types of organometallic precursor systems can be used, (i) single source precursors that possess organic ligands and metal-oxygen bonds (*e.g.*, iron cupferronate, iron acetylacetonate, and iron oleate complexes), or (ii) dual source systems where metallic precursors and additional oxidizers (*e.g.*, $(CH_3)_3NO$)) are introduced for controlled oxidation. The precursors are mixed with non-hydrolytic organic solvents containing stabilizing surfactants and are then heated for thermal decomposition. As a result, monomers are generated and, when their concentration is above a supersaturation level, the nucleation and subsequent growth of crystalline nanoparticles are induced (Fig. 12b).[187] The size of

MNPs can be finely controlled by varying the reaction condition, such as the types of solvent, heating rate, surfactant, and reaction time, or by seed-mediated growth process.

In one typical study by Sun *et al.*, the preparation of monodisperse Fe_3O_4 MNPs with an average size of 4 nm (less than 10% standard deviation) is reported. In their study, iron (III) acetylacetonate ($Fe(acac)_3$) precursors in phenyl ether are decomposed at a high temperature (260 °C) in the presence of a mixture of surfactants (oleic acid and oleylamine) and reducing agent (1,2-hexadecanediol).[188] When the reaction solvent is changed from phenyl ether (boiling point, B.P. = 259 °C) into benzyl ether (B.P. = 298 °C), larger MNPs with a diameter of 6 nm are obtained. The size of the MNPs can be further increased up to 20 nm through a seed-mediated growth using 3–4 nm Fe_3O_4 MNPs as seeds. Regardless of the size of the MNPs, the heating rate is an important parameter for determining the size distribution of the MNPs. Typically, for highly monodisperse MNPs, the mixture is first heated up to 200 °C and it remains at that temperature for some time (ageing) and is then finally heated up to 260–300 °C. When the mixture is directly heated up to a reflux temperature, the resultant MNPs have a wide size distribution from 4 to 15 nm.

Cheon and colleagues demonstrated size-controlled syntheses of single-crystalline maghemite MNPs by modulating the amount and type of surfactants as well as the reaction times.[186] The size of the synthesized MNPs was increased from 12 to 50 nm by increasing the surfactant-to-metal precursor ratio and reaction time. When sufficiently large amounts of surfactant are introduced, surfactants are reversibly coordinated to the MNP surface, allowing for further growth. The long reaction time provides sufficient opportunity for the Ostwald ripening process during which large MNPs grow larger at the expense of smaller MNPs.[189] The same researchers also showed the surfactant effects on the shape of MNPs. The morphological structure of maghemite is mostly governed by three surfaces, (100), (110), and (111). Therefore, the shape can be controlled by modulating the degrees of truncation along those surfaces. For example, at a low surfactant concentration, surfactants mostly bind to the highest-energy (111) surfaces and growth along the [111] direction is restricted. The resulting (111) truncated MNPs can have diverse shapes, including sphere, diamond, and prism. When the surfactant concentration increases significantly, (111) and the next highest-energy (110) surfaces are covered by surfactants providing hexagon-shaped MNPs.

To produce highly monodisperse MNPs, Hyeon *et al.* took advantage of an iron-oleate complex.[119, 184] First, they prepared an iron-oleate complex ($Fe(oleate)_3$) by reacting iron chloride with sodium oleate; then, they slowly heat the complex up to 310 °C in the presence of organic solvent and surfactants. According to the study, nucleation occurs at 200–240 °C when one oleate ligand is dissociated from $Fe(oleate)_3$ and growth occurs at about 300 °C by the dissociation of remaining two oleate ligands from the iron-oleate complex. Owing to this nature of the iron-oleate complex, the nucleation and growth process can be effectively separated, which is a key requirement for preparing uniformly sized MNPs. By modulating the decomposition temperature and ageing time, the MNP size is controlled from 5 to 22 nm. Additionally, all of the MNPs are monodisperse with a size distribution of less than 4 %.

These non-hydrolytic thermal decomposition approaches can be further extended to the syntheses of transition metal-doped ferrite MNPs (MFe_2O_4, M = Co, Fe, Ni, Mn, and Zn) simply by using additional divalent transition metal precursors, such as $M(acac)_2$ or MCl_2 (M = Mn, Fe, Co, Ni, and Zn).[147, 148, 185] Such substitution of Fe^{2+} into transition metals offers an opportunity to precisely control the magnetic properties of ferrite MNPs to enhance the saturation magnetization. Ferrite MNPs have an inverse spinel crystal structure with the oxygen anions arranged in a face-centered cubic close-packed lattice.[130] The tetrahedral (T_d) sites are occupied by Fe^{3+} ions and octahedral (O_h) sites are filled with Fe^{3+} and Fe^{2+} ions. Under an external magnetic field, the magnetic spins of the metal ions at the O_h sites align parallel to the external magnetic field, while those at the T_d sites align antiparallel to the field. Therefore, each magnetic spin of one octahedral Fe^{3+} and the other tetrahedral Fe^{3+} is canceled out, and only the magnetic spins of octahedral Fe^{2+} with a high spin d6 configuration induce a total magnetic moment per unit of 4 μ_B (Bohr magneton; 9.27×10^{-24} J/T).[147, 190] In this sense, it is possible to control the net magnetic moment by replacing octahedral Fe^{2+} with divalent transition metal ions.

Following the report on the syntheses of monodisperse metal-doped ferrite MNPs by Sun *et al.*,[185] Lee *et al.* demonstrated the dopant effects on magnetism and MRI contrast effects.[147] A series of 12 nm metal-doped ferrite MNPs, including $MnFe_2O_4$, $FeFe_2O_4$, $CoFe_2O_4$, and $NiFe_2O_4$, are fabricated. The reaction is performed by heating an octyl ether solution containing divalent metal chloride (MCl_2, M = Mn^{2+}, Fe^{2+}, Co^{2+}, and Ni^{2+}), iron (III) acetylacetonate, oleic acid, and oleylamine. As a result of the electron spin configurations of the metal-doped ferrite MNPs, their net magnetic moment per unit $MnFe_2O_4$, $FeFe_2O_4$, $CoFe_2O_4$, and $NiFe_2O_4$ is estimated as 5 μ_B, 4 μ_B, 3 μ_B, and 2 μ_B, respectively. Reflecting those estimations, the M_0 values of those MNPs are measured as 110 emu g^{-1} ([Mn + Fe]), 101 emu g^{-1} ([Fe]), 99 emu g^{-1} ([Co + Fe]), and 85 emu g^{-1} ([Ni + Fe]). Recently, Jang *et al.* synthesized Zn-doped ferrite MNPs ($(Zn_{0.4}Fe_{0.6})Fe_2O_4$) and Zn-/Mn-doped ferrite MNPs ($(Zn_{0.4}Mn_{0.6})Fe_2O_4$) with high M_0 of 161 emu g^{-1} ([Zn + Fe]) and 175 emu g^{-1} ([Zn + Mn + Fe]).[148] The Zn^{2+} doping level, a key-parameter for a high M_0 value, is precisely controlled by varying the molar ratio between metal precursors. Another example of metal-doped ferrite MNPs utilizes not only the doping but also the sizing strategies to achieve a high magnetization. Lee *et al.* synthesized metal-doped ferrite MNPs by reacting the mixture of $Fe(acac)_3$, $Mn(acac)_2$, and 1,2-hexadecanediol at a high temperature of 300 °C.[44] The size of the resultant $MnFe_2O_4$ MNPs (10 nm) is further increased to 12 nm, 16 nm, or 22 nm through a seed-mediated growth strategy. In particular, the MNPs with a size of 16 nm show excellent MRI T_2 contrast effects with an r_2 of 420 $mM^{-1}s^{-1}$, which is about 7-fold higher than that of MIONs.

4.2. Elemental Iron-based MNPs

Monometallic MNPs, such as cobalt, iron, and nickel, have been extensively studied due to their prominent magnetic properties.[132, 137, 191] Monometallic MNPs exhibit superior magnetization than their corresponding oxides, making them an ideal choice for bio-applications including highly sensitive detection of biomolecules and molecular MRI.[134-139] The elemental iron-based MNPs are especially attractive, owing to their high saturation magnetization value (218 emu g^{-1}) as well as biocompatibility originating from the non-

toxic nature of iron.[192] Therefore, the controlled synthesis of elemental iron-based MNPs has been an important goal in magnetic nanomaterial science. The non-hydrolytic thermal decomposition is the most common method for preparing elemental iron MNPs.[139, 193, 194] However, there still remain challenges to obtaining pure monometallic iron MNPs because iron nanoparticles are extremely reactive and readily oxidized, resulting in undesired changes in the magnetic properties. Therefore, elemental iron-based MNPs require passivation by an oxidatively inert protection layer, such as carbon,[195] metal oxide,[44, 128, 196, 197] noble metal,[198, 199] polymers,[200] and silica[201].

The most representative strategy for producing such stable MNPs is non-hydrolytic thermal decomposition synthesis of elemental iron MNPs followed by a controlled oxidation process to form a protective iron oxide layer.[44, 128, 196, 197] According to a method provided by Cabot *et al.*, an iron pentacarbonyl precursor is thermally decomposed in air-free octadecene solvent containing oleylamine as a surfactant.[196] The as-synthesized iron nanoparticles are then heated in the presence of oxygen, resulting in a core-shell structured Fe@Fe_3O_4 MNPs. The size of the nanoparticles can vary from 5 to 18 nm by adjusting reaction parameters, such as the surfactant level, temperature, and time. The thickness of a surface iron oxide layer can also be precisely tuned by controlling the reaction temperature because the shell growth is dependent on iron diffusivities which are exponentially affected by the temperature. Under air exposure at room temperature, an oxide shell that is only a few nanometers thick is formed on the surface MNPs. When the reaction temperature increases up to 350 °C, the thickness of the shell reaches up to 10 nm, while simultaneously leaving vacancy behind the Fe core. This vacancy formation can be explained by the Kirkendall effect. As the reaction proceeds, iron atoms are continuously diffused outward from the core, resulting in a growth of oxide shell on the surface of nanoparticle and inducing a void at the core. Therefore, to generate stable core-shell structured MNPs without void, it is crucial to optimize the reaction conditions with an adequate temperature and air exposure time.

Regardless of the thickness, the iron oxide shell in the as-synthesized nanoparticles has poor crystallinity.[196, 197] This is problematic because the amorphous iron oxide shell cannot effectively protect the metallic Fe core from deep oxidation. For example, as-synthesized MNPs with a 2.5 nm Fe_3O_4 shell and 4 nm Fe core are naturally oxidized at room temperature within 4 h of their exposure to air, leading to a thicker shell of 3.5 nm and a smaller core of 3 nm.[197] This oxidation process reduces the M_0 value of MNPs from 123.5 emu g^{-1} to 99.4 emu g^{-1} ([Fe]). To make Fe@Fe_3O_4 nanoparticles more stable, Peng *et al.* coated a crystalline Fe_3O_4 shell via controlled oxidation process, which is mediated by an oxidizing agent $(CH_3)_3NO$.[197] This controlled oxidation results in an Fe_3O_4 shell with an inverse spinel crystal structure. In this technique, the thickness of the shell is modulated by adjusting the amount of $(CH_3)_3NO$. The M_0 value of resulting MNPs is stably maintained upon air exposure.

Based on the synthetic methods mentioned above, 16 nm elemental iron-based MNPs, known as “cannonballs”, were developed by Lee *et al.*[44] The cannonballs (CBs) had an 11 nm elemental Fe core coated with a 2.5 nm thick Fe_3O_4 shell. The CBs showed a superior magnetization of 139 emu g^{-1}, which was 1.6-fold higher than that of 16 nm Fe_3O_4 nanoparticles. To further enhance the magnetic properties, Yoon and co-workers utilized a

synthetic approach that enables tuning of the shell composition.[128] Instead of oxidizing the surface of the Fe core, Fe MNPs are annealed in the presence of an iron-oleate complex. In this method, transition metals (Mn^{2+} or Co^{2+}) can easily be doped into a ferrite shell by co-injecting a stoichiometric amount of Mn-oleate or Co-oleate with Fe-oleate. This facile control of the shell composition allows for tailoring the magnetic properties of MNPs. For example, the high magnetic moment of $MnFe_2O_4$ allows $Fe@MnFe_2O_4$ MNPs to exhibit the highest M_0 value of 145 emu g^{-1} of MNPs with other shell compositions. Consequently, the $Fe@MnFe_2O_4$ MNPs are successfully used in magnetic resonance-based sensing applications.[128]

In addition to those iron nanoparticles covered with oxides, there are few other types of elemental iron-based MNPs such as iron silicide (Fe_3Si) and iron carbides (Fe_3C). In their bulk state, Fe_3Si and Fe_3C possess a relatively high saturation magnetization value of 84 emu g^{-1} and 130 emu g^{-1}.[202, 203] These materials are known to be more resistant to oxidation than iron nanoparticles. They can therefore maintain their original magnetic properties for long-term biomedical applications. Fe_3Si and Fe_3C can be prepared via various synthetic means including a gas-phase method (*e.g.*, chemical vapor deposition),[204] laser pyrolysis,[205, 206] and other high-temperature methods (*e.g.*, calcination)[207]. Recently, non-hydrolytic thermal decomposition routes have been reported for Fe_3Si and Fe_3C MNPs. Dahal *et al.* prepared Fe_3Si MNPs by refluxing $Fe(CO)_5$ and silicone tetrachloride ($SiCl_4$) in a mixture of solvent and surfactants.[202] The size of Fe_3Si MNPs was controlled from 4.2 to 7.5 nm by increasing the concentration of precursors at fixed molar ratios for iron to silicon. The 7.5 nm Fe_3Si MNPs showed an M_0 value of 60 emu g^{-1}, which is similar with that of ferrite MNPs. Shultz *et al.* synthesized 2.7 nm Fe_3C MNPs by injecting $Fe(CO)_5$ into a refluxing trioctylphosphine oxide.[203] The Fe_3C MNPs are further coated with a thin layer of iron oxide and gold for more enhanced resistance to oxidation. The resulting $Fe_3C@FeO_x@Au$ MNPs yielded a high M_0 value of 110 emu g^{-1}, which is comparable to that of 12 nm Mn-doped ferrite MNP.[147]

4.3. Iron-based bimetallic alloy MNPs

Bimetallic alloy nanoparticles are another important class of MNPs.[143, 144, 146, 208, 209] Unlike ferrite-based MNPs, all magnetic spins in the bimetallic alloy MNPs align parallel to the external magnetic field. Therefore, in general, the magnetic moments of bimetallic alloy MNPs are higher than that of ferrite MNPs. For example, the magnetic moment of FeCo nanoparticles is 2.4 μ_B per magnetic atom, which is about two-fold larger than that of Fe_3O_4 nanoparticles.[190, 210] This superior magnetic property makes bimetallic alloy MNPs possible candidates for bio-medical applications.

The bimetallic MNPs are classically fabricated by a physical deposition process, including vacuum-deposition technique and gas-phase evaporation.[144, 211, 212] However, MNPs produced by these physical methods often suffer from several limitations, such as particle aggregation, wide size distribution, and poor colloidal stability.[208] In contrast, solution phase chemical synthesis offers an effective means of synthesizing monodisperse bimetallic MNPs. The most established chemical synthesis route is reduction decomposition of metal precursors.[143, 145, 208] In this method, iron pentacarbonyl is thermally decomposed to Fe and

carbon monoxides and metal acetylacetonate ($M(acac)_2$, M = Pt or Co) is reduced by 1,2-alkanediol to pure metal. These two metal atoms are combined, forming bimetallic clusters (Fe-M), which act as nuclei. As more Fe-M species are deposited around the nuclei, the growth continues, leading to the formation of bimetallic alloy MNPs. Surfactants, such as oleic acid and oleylamine, are commonly introduced for particle stabilization. The composition of MNPs is controlled by the ratio between $Fe(CO)_5$ and $M(acac)_2$.[213] Due to the difference in the rate of decomposition and reduction, the stoichiometric level of metal sources will lead to an unequal atomic percentage of Fe and M. To have bimetallic MNPs with near-equal levels of Fe and M, the compositional relation between $Fe(CO)_5/M(acac)_2$ ratio and x in $Fe_xM_{(100-x)}$ should be experimentally investigated. For better control of composition, $Na_2Fe(CO)_4$, which acts as not only an Fe source but also a reducing agent, can be used instead of $Fe(CO)_5$.[214] The Fe^{2-} from $Na_2Fe(CO)_4$ is oxidized to Fe, and M^{2+} is reduced to M by two electrons transferred from Fe^{2-}. In this sense, bimetallic alloy nanoparticles with 1:1 stoichiometry can be obtained.

The size of bimetallic alloy MNPs is tuned by modulating the molar ratio between metal sources and surfactants, level of reducing agents, and reaction temperatures. Satoru *et al.* achieved fine-tuning of the FePt MNP size through simply changing the amount of surfactants.[215] As the amount of surfactants increases, the nanoparticle size proportionally increases from 2 to 5 nm, which is due to a decrease in the nucleation rate caused by surfactants. Chen *et al.* excluded reducing agent from the reaction mixture to modulate the size of the nanoparticles.[216] Because the reduction of $M(acac)_2$ is essential to form nuclei, the exclusion of reducing agent slows down the nucleation rate, allowing more metals to deposit around the nuclei, leading to a larger particle. The authors demonstrated that the reaction temperature also critically affects to the nucleation rate and the size of MNPs. The higher reaction temperature induces the faster nucleation and smaller nanoparticles. For example, the size of MNPs synthesized at 240 °C is 6 nm, while the nanoparticles produced at 225 °C are 9 nm.

5. Physical Characterization

The physical properties of MNPs can be measured using conventional material characterization tools. When measurements are performed on large number of MNPs, the acquired data should be interpreted as size-weighted ensemble average.

5.1. Particle size

The most widely used methods to measure MNP size include transmission electron microscopy (TEM) and dynamic light scattering (DLS). These two modalities are complementary: TEM images the MNP cores in a dried powder form, whereas DLS measures the hydrodynamic diameter of particles in a suspension.

TEM is a versatile method that can provide morphological, compositional, and crystalline information of MNPs. The technique images electrical interactions between MNP crystals and a beam of electrons. The imaging resolution can be down to atomic scale (a few angstroms), due to the small wavelength of the electron beam (Fig. 13a).[44] TEM can visualize many individual MNPs cores, and thereby facilitates the assessment of particle size

distribution (Fig. 13b). In the electron diffraction mode, TEM can project reciprocal crystal lattice into concentric ring patterns (Fig. 13c), which is useful to quickly identify crystal structures. When combined with spectroscopic instruments (*e.g.*, energy-dispersive X-ray/ EDX spectrometer, electron energy-loss/ EEL spectrometer), TEM can generate atomic-scale elemental maps for compositional analysis (Fig. 13d).[217]

DLS measures the scattered light from MNPs upon their illumination with a monochromatic light source. The intensity of the scattered light fluctuates over time, as particles undergo Brownian motion. The fluctuation rate can be converted into the diffusivity of particles, and eventually into hydrodynamic diameter (d_h) through the Stokes-Einstein relationship. Consequently, DLS estimates the effective particle size in fluid, which encompasses the magnetic core and its surface molecules. The data, however, should be carefully inspected. The original size distribution measured by DLS is intensity-weighted ($\sim d_h 6$), and therefore can be dominated by the presence of MNP aggregates or oversized particles. To spot such distortion, the volume and the number distributions, mathematically derived from the intensity distribution, should be objectively compared as well for consistency.

5.2. Crystal structure

Similar to the electron diffraction in TEM, the crystal structure of MNPs can be analyzed through X-ray diffraction (XRD). The method measures X-ray waves reflected from solid crystals. When the X-ray incident on a crystal satisfies the Bragg's condition, the reflected waves from the lattice planes undergo constructive interferences, producing strong intensity peaks. By using powdered MNPs and scanning the incidence angle of the X-ray, diffraction peaks from all possible lattice orientations can be obtained. The measured diffractogram is then compared with standard patterns, to identify the crystal structure. The average crystal size (d_{XRD}) can be further estimated from the Scherrer formula, $d_{XRD} \approx \lambda \cdot (\beta \cos\theta)$, where λ is the x-ray wavelength, β is the peak width at half the maximum intensity, and θ is the Bragg angle.[218] Figure 14 shows an XRD diffractogram of Fe_3O_4 MNPs (16 nm in diameter under TEM), with each peak assigned to a distinct lattice plane of a spinel group. The estimated crystal size (d_{XRD}) from the (311) peak was 15.4 nm (Fig. 14, inset), close to that by TEM (16 nm). This indicates that the prepared MNPs are mostly composed of single domain crystals.[44]

5.3. Composition

Particle composition can be measured in several ways. To quickly obtain stoichiometric ratios of different elements within the particle, electron spectroscopies (*e.g.*, EDX, EEL) can be applied during electron microscopy. For the quantification of absolute amounts, however, inductively coupled plasma-atomic emission spectroscopy (ICP-AES) is often used. In this method, MNPs are chemically dissolved into constituent atoms, and the atomic electrons are thermally excited by Ar-plasma. When the excited electrons return to ground state, they emit light at specific wavelengths that are characteristic of a given atom. ICP-AES has exquisite sensitivity, down to part-per-million level, and can identify multiple elements in a single measurement.

5.4. Magnetic properties

For comprehensive magnetic characterization of MNPs, both the temperature (T) and the field (H) dependent magnetizations are measured. Superconducting quantum interference device (SQUID) or vibrating sample magnetometers are typically used.

5.4.1. Temperature-dependent magnetization—To measure temperature-dependent magnetization $M(T)$, samples are first cooled down from high (≈ 300 K) to low temperature (<4 K) in the absence of external magnetic fields. The process, called zero-field cooling (ZFC), locks the magnetic moments of MNPs, that are randomized by thermal fluctuation at high temperature. Samples are then heated back to high temperature in the presence of a small measuring field (~100 G), and the magnetization is measured at different temperature.

A salient feature of $M(T)$ is the existence of a characteristic temperature at which M has the maximum value (Fig. 15a). This temperature, defined as the blocking temperature (T_B), indicates the onset of the superparamagnetic state.[219] When $T < T_B$, the M values monotonically increase with temperature, because thermal energy helps the magnetic moments of individual particles to align with the external magnetic fields. Beyond T_B, thermal energy becomes large enough to randomly flip the magnetic moments, leading to a decrease of M. For a given MNP type, the blocking temperature is proportional to the particle volume (V), since MNPs become superparamagnetic when the thermal and the anisotropy energies are comparable to each other ($k_B \cdot T_B \approx K \cdot V$). As an example, Fig. 15a shows the $M(T)$ curves of Fe_3O_4 MNPs with different core sizes.[119] All particles are superparamagnetic at room temperature (T_B< 300 K), and T_B increases linearly with the particle volume (Fig. 15b).

5.4.2. Field-dependent magnetization—In this measurement, samples are subjected to sweeping external magnetic fields (H), and their induced magnetization $M(H)$ is monitored. The resulting $M(H)$ curve provides many important information:[116, 220, 221] (i) the saturation magnetization (M_0), the maximum magnetization value; (ii) the remanence (M_R), the residual M at $H = 0$; and (iii) the coercivity (H_c), the external field required to reduce $M = 0$. When particles assume permeant magnetic moments, M_R and H_c are non-zero, and the resulting $M(H)$ displays a hysteresis loop. MNPs below the blocking temperature shows such behavior, consistent with the ferromagnetic state of particles (Fig. 15c). For superparamagnetic particles, however, $M(H)$ collapses into a single curve (Fig. 15d) as both M_R and H_c vanish. MNPs thus assume magnetic moments only in the presence of external fields.

6. Surface Coating Strategies of magnetic nanoparticles

Most biomedical applications require long-term stability of MNPs without aggregation or precipitation (i) in physiological media (high salt concentrations and/or proteins), (ii) at different pH, and (iii) at room/body temperature. Because the interactions of MNPs with the surrounding media are governed by the chemical properties of the nanoparticle surface, it is necessary to develop efficient surface coating methods. The stability of nanoparticles depends on the equilibrium between inter-particle attractive and repulsive forces (Fig. 16a).[222-224] The MNPs tend to aggregate due to the attractive interaction originating from van der

Waals force and a magnetic dipolar force under an external magnetic field. Therefore, endowing MNPs with repulsive forces that exceed an attractive forces is crucial in stabilizing MNPs. The MNPs can have adequate repulsive forces of electrostatic and steric repulsion by modifying their surface with adequate coating materials.[133, 158, 159, 225]

The surface coating not only provides colloidal stability but also allows for the generation of biocompatible MNPs. Several ferrite MNPs such as maghemite and magnetite are generally regarded as non-toxic and biologically tolerated because they can be incorporated into the natural metabolic pathways of the body.[226] Indeed, there currently exists an MNP which is approved for clinical trials (*i.e.*, ferumoxytol; dextran-coated magnetite nanoparticle).[155] However, when those MNPs are naked, they can induce various toxic effects including reactive-oxygen species generation and radical formation via Fenton reaction.[227] Fe-based MNPs containing transition metals (*e.g.*, Co, Ni, Mn, etc.) can induce toxicity as a result of biodegradation followed by leaching of transition metals.[228] Rapid oxidation of elemental iron MNPs also cause toxicity by resulting in oxidative stress.[229] In this sense, MNPs can be protected from rapid degradation and/or oxidation in physiological environments by employing adequate surface coating strategies reducing the risk of toxicity. The surface coatings also provide chemical functionalities for (i) conjugation of affinity ligands and (ii) serve to reduce non-specific serum protein adsorption in the form of a nanoparticle corona (opsonization).[230, 231]

Depending on the synthetic routes, the as-synthesized MNPs are initially stabilized by either hydrophilic or hydrophobic surface ligands. For example, the ferrite MNPs fabricated by the co-precipitation method in the presence of water-soluble ligands (*e.g.*, dextran, starch, albumin, alginate or chitosan) are readily dispersible in aqueous solution due to the *in situ* hydrophilic surface coatings.[160, 161, 232-234] On the contrary, the non-hydrolytically synthesized MNPs are usually surrounded by a layer of hydrophobic surfactants and are only soluble in non-polar organic solvents. Therefore, additional hydrophilic surface coatings are required.

This section focuses on surface coating strategies for stabilizing, protecting, and functionalizing non-hydrolytically produced MNPs. The coating methods depend on the type of MNPs, nature of coating materials, and intended applications. The MNP surface modification is achieved via ligand exchange or encapsulation. A diverse group of materials, such as small molecule organic ligands, polymeric ligands, amphiphilic micellar ligands, dense polymer matrix, and inorganic materials, are utilized in such coating processes.

6.1. Ligand exchange

Metallic atoms on the MNP surface are electron deficient as they are coordinatively unsaturated; thus, they have an affinity for electron rich functional groups, such as amino, carboxyl, hydroxyl, phosphate, and sulfhydryl. In this sense, hydrophobic surfactants on the MNP surface can be replaced with hydrophilic ligands by reacting MNPs with excess hydrophilic molecules (Fig. 16b). Such hydrophilic ligands consist of (i) an electron rich functional group that binds to the MNPs and (ii) a secondary functional group or hydrophilic region, which is exposed to the aqueous solution. The ligand exchange has several advantages, including the simple reaction procedure, thin coating layer, and small overall

MNP size. There has been extensive research on the development of ligand systems that can effectively bind to MNPs.

6.1.1. Small molecule ligand—Among a variety of small molecules, dopamine and its derivatives are unique because of their robust binding to ferrite-based MNPs. The catechol unit of dopamine can be effectively coordinated with iron atoms on the nanoparticle surface by forming a stable five-membered ring.[235] The first case study of MNP ligand exchange using dopamine is reported by Xu *et al.*[235] They transferred the $Co@Fe_2O_3$ MNPs from hydrophobic to hydrophilic by using dopamine, which is pre-modified with nitrilotriacetic acid. Wei *et al.* synthesized a dopamine sulfonate ligand to improve the stability.[236] The combination of the amine and sulfonate groups gives dopamine sulfonate a zwitterionic character, which enhances the pH stability and prevents non-specific interaction with proteins. Recently, Liu and colleagues converted hydrophobic Fe_3O_4 to an aqueous phase using a dopamine derivative (3,4-dihydroxyhydrocinnamic acid) without any complicated organic synthesis. The resultant hydrophilic MNPs show high colloidal stability over a wide pH range (pH= 3–12).[237]

Another example of small molecule ligands are carboxylates, one example being citric acid. Citric acid binds to the surface metal atoms by coordinating one or two carboxylic acid groups. As a result, at least one carboxylic acid group is exposed to the aqueous solvent, making the nanoparticle surface negatively charged and water-soluble. Taupitz and co-workers utilized citric acid to coated very small iron oxide nanoparticles (VSOP).[238] The MNPs had a compact hydrodynamic size of 8.6 nm and are robustly utilized as blood-pool MRI contrast agents. 2,3-dimercaptosuccinic acid (DMSA), which contains two carboxyl groups and two sulfhydryl groups, is another representative small molecule ligand.[147, 239, 240] The carboxylic acid groups at one end coordinatively bind to the nanoparticle surface, while the thiol groups at the other end stabilize nanoparticles by disulfide cross-linkage between other DMSA molecules. Jun *et al.* reported DMSA-coated Fe_3O_4 MNPs with high colloidal stability and their in vivo MRI applications.[239] Yoon *et al.* also utilized DMSA to stabilize $Fe@MnFe_2O_4$ MNPs.[128] The DMSA-coated MNPs are further conjugated with affinity ligands, such as antibody and biotin, and utilized in μNMR sensing applications.

6.1.2. Polymeric ligand—Organic polymers are widely used as stabilizing ligands due to their distinctive characteristics, including multi-dentate binding capability and steric repulsion effects. Compared to small molecules, organic polymers attach to nanoparticles via multiple functional groups resulting in a stronger steric repulsive force.

Polyethylene glycol (PEG) is one of the most common polymeric ligands in MNP surface coating. PEG is an FDA-approved, biocompatible synthetic polymer that can be prepared with a wide range of sizes and functional groups.[241] PEGylated MNPs not only show high colloidal stability, they are protein resistant. With these characteristics, PEGylated MNPs are not easily recognized by the immune system and, therefore, they are often regarded as “stealth” nanoparticles.[242, 243] PEGylated MNPs are especially effective for selective detection of biological targets, which is highly desirable for biomedical applications, such as in vivo targeted imaging, drug delivery, or magnetic-based biosensing. For the PEGylation

of MNPs, one or both ends of PEG are usually modified with functional groups that have affinity to the nanoparticle surface. Xie *et al.* reported surface modification of Fe_3O_4 MNPs using dopamine (DOPA) terminated PEG.[244] Hydrophobic surfactants, such as oleate and oleylamine are replaced with DOPA-PEG molecules via a ligand exchange reaction. To obtain better colloidal stability, Amstad and co-workers introduced a nitro group to DOPA-PEG molecules.[245] Although the exact mechanism has not yet be determined, nitro-dopamines bind more tightly to MNPs with a significantly lower desorption rate compared to other dopamine derivatives. PEGs functionalized with a multi-dentate functional group have an enhanced ability to bind to nanoparticles. For example, polymeric phosphine oxide-modified PEG can effectively bind to maghemite nanoparticles via a number of coordinative oxygen atoms.[246, 247] Kohler *et al.* utilized a silane-terminated PEG ligand for PEGylation.[248] The use of a silane binding group increases the PEG packing density by hydrogen bonding between the carbonyl and amine groups present within the ligand. Na *et al.* devised an oligo PEG-DOPA, which consists of a short poly(acrylic acid) backbone laterally appended with several catechol binding groups and PEGs.[249] The resulting nanoparticles are stably dispersed in phosphate buffered saline (PBS) solution with a pH at 7.4.

Another widely utilized polymer is dextran. Dextran possesses excellent biocompatibility and has been used in other biomedical applications.[250] Dextran and its derivatives (*e.g.*, carboxy dextran and carboxymethyl dextran) can be naturally degraded into biocompatible glucose by endogenous dextranse enzyme.[251] Most clinical type MNPs have used dextrans as a surface coating (Combidex®, dextran; Feraheme®, carboxymethyl dextran; Feridex®, dextran; and Resovist®, carboxydextran).[150-153, 174] As described in the previous section, dextran is usually coated *in situ* during the co-precipitation synthesis process. However, some studies describe post-synthesis dextran coating methods. Creixell and co-workers coated carboxymethyl dextran on the surface of peptized iron oxide nanoparticles.[252]

In addition to PEG and dextran, numerous other polymeric systems are available for ligand exchange. Here we briefly introduce some of the widely used polymers, including poly(vinylpyrrolidone) (PVP), poly(vinylalcohol) (PVA), and poly(ethyleneimine) (PEI). PVP is an FDA-approved, water-soluble polymer that has been used as a plasma volume expander.[253] Dong and colleagues coated Fe_3O_4 MNPs with PVP after removing previously bound surfactants with nitrosonium tetrafluoroborate ($NOBF_4$), which facilitates the removal through protonating the metal binding functional groups.[254] The PVP-coated MNPs in an aqueous media are stably dispersed without aggregation or precipitation for several months. Another FDA-approved synthetic polymer, PVA, has been widely used in medical applications (e.g., surgical sutures) due to its biodegradability and high water-solubility. One typical example of PVA coated MNP is AminoSpark® which is a commercial probe for *in vitro* or *in vivo* imaging.[35] To increase PVP coating stability, Liong *et al.* reported the use of carboxymethyl modified PVA (CMPVA).[255] Hydrophobic ligands on $MnFe_2O_4$ MNPs are first replaced with tetramethylammonium hydroxide (TMAOH) and then further coated with CMPVA. The resulting CMPVA-coated MNPs are highly stable in aqueous condition. PEI is a multi-dentate, water-soluble cationic polymer containing abundant primary amine and secondary amine groups that show strong affinity to surface metal atoms.[256] PEI has been widely used as transfection agent because PEI can electrostatically bind to the negatively charged phosphate backbone of DNA.[257] Therefore, MNPs coated with PEI can be

effectively utilized for therapeutic gene delivery.[258] Duan *et al.* functionalized magnetite nanoparticles using PEI and PEG-modified PEI (PEI-co-PEG). Both surface coated MNPs are well dispersed in aqueous solution for more than three months.[259]

6.2. Encapsulation

Encapsulating MNPs in a biocompatible, hydrophilic shell is another method of phase transfer of non-hydrolytically produced MNPs. There are several nanoparticle encapsulation methods that can be classified according to the shell materials and encapsulation processes (Fig. 16c). Amphiphilic ligands, water-soluble polymer matrix, and hydrophilic inorganic material (*i.e.*, silica) are commonly used as shell materials.

6.2.1. Amphiphilic micellar ligand—The encapsulation of nanoparticles with amphiphilic ligands can be achieved by simply mixing the nanoparticles with amphiphilic ligands in an adequate solvent. This can result in highly stable, micellar-coated nanoparticles. In this process, the hydrophobic region of amphiphilic ligand is intercalated with hydrophobic surfactants on nanoparticles by hydrophobic interactions, while the remaining hydrophilic region solubilizes the nanoparticles in aqueous solvent. A number of amphiphilic molecules have been used for the phase transfer of MNPs. One typical example is PEG-phospholipid block-copolymer. Lee *et al.* prepared MNPs with a high colloidal stability, good cell biocompatibility, and strong T_2 MRI contrast effects by encapsulating magnetite nanoparticles with PEG-phospholipid.[260] Seo and colleagues encapsulated FeCo MNPs in PEG-phospholipid micelles and demonstrated their colloidal stability which is sufficient for *in vivo* MRI application.[144] In addition to PEG-phospholipid, many of other block-copolymers, such as PEG-2-tetradecylether,[261] polylactide-PEG,[262] poly(maleic anhydride-*alt*-1-octadecene)-PEG,[263] polystyrene-poly(acrylic acid) (PS-PAA),[264] and tetradecylphosphonate[261] can be used as amphiphilic ligands. However, MNPs encapsulated in block-copolymers have a relatively large hydrodynamic size compared to those MNPs prepared by the ligand exchange method. This is due to large micelle coating thickness originating from the high molecular weight of block-copolymers. Considering the hydrodynamic size is highly related to the physical properties (*e.g.*, Brownian relaxation) of MNPs, it is crucial to develop a method for controlling the thickness of micelle coating while maintaining the colloidal stability of MNPs.[265, 266] Oligomeric or dendritic molecules can be a good candidate for providing a thin, micellar shell. In a study by Wang *et al*, micellar-coated MNPs with a thin coating is prepared using α-cyclodextrin (α-CD), which is a naturally occurring, cyclic oligosaccharide containing hydrophobic cavities and hydrophilic rims.[267]

6.2.2. Polymeric matrix—The incorporation of MNPs in a hydrophilic, dense polymeric matrix is an additional way of generating water-soluble MNPs. Various block-copolymers, such as polystyrene-co-PEG (PS-co-PEG),[268] poly(lactic-co-glycolic acid)-co-PEG (PLGA-co-PEG),[269, 270] polystyrene-co-poly(acrylic acid) (PS-co-PAA),[271, 272] and poly(lactic acid)-co-PEG (PLA-co-PEG),[273] have been used as a matrix. Because single polymer matrix particles can contain a large number of MNPs, the nanoparticles-polymer hybrids can have a significantly high magnetic moment.[274-276] Typically, such hybrids can be fabricated by polymerization of monomers in the presence of MNPs. Xu and colleagues prepared PS/silica

matrix particles containing hydrophobic Fe_3O_4 MNPs *via* oil-in-water emulsion polymerization.[277] The MNPs-PS/silica hybrid has an average size of 134 nm with a polydispersity of 7.5%. Kaewsaneha *et al.* embedded magnetite MNPs in a water-soluble PS-co-PAA matrix through polymerization of styrene and acrylic acid monomers in the presence of MNPs and azobisisobutyronitrile (AIBN) initiator.[278] The resulting end product with a hydrodynamic size of 250 nm shows adequate colloidal stability. The application of such MNP-polymer hybrids in POC diagnostics has been demonstrated by Neely and co-workers.[279] They developed a highly sensitive T_2 magnetic resonance sensor system using carboxylated polymer matrix (800 nm) embedded with numerous iron oxide MNPs. They successfully detected bloodstream infections of *Candida spp.* with sensitivity ~100-fold higher than that of conventional techniques.

6.2.3. Hydrophilic inorganic material—Inorganic materials, such as silica and precious metal, have been used to prepare water-soluble MNPs. In particular, silica has been extensively studied as an efficient coating material due to its advantages of hydrophilicity, high density of surface functional groups, and easily controllable shell thickness.[280-283] The surface of silica is negatively charged as a result of proton dissociation of terminal silanol groups. Therefore, electrostatic repulsive forces stabilize MNPs encapsulated in silica. Silica can also protect MNPs from an undesirable chemical transformation, such as oxidation of elemental metallic nanoparticles.[201]

A common approach for encapsulating MNPs in silica is sol-gel reaction (stöber process), where silica is synthesized via the hydrolysis and condensation of silicon orthoester ($Si(OR)_4$) (*e.g.*, tetraethyl orthosilicate (TEOS) and tetramethyl orthosilicate (TMOS)).[281-284] In this process, silicon orthoesters are first hydrolyzed, yielding silicic acids ($Si(OH)_4$); then, they undergo poly-condensation into a three-dimensional network of Si-O-Si. The reaction between uncondensed silanol and hydroxyl groups on the MNPs surface forms a Si-O-M bond, which facilitates silica coating on the MNP surface. This process can be catalyzed by either acid or base, and the shell thickness is controlled by varying the concentration of silicon precursors.[285] The surface silanol groups can further be modified with amine and sulfhydryl functional groups by employing respective aminoethoxy silane and mercaptoethoxy silane. Carboxylic acid groups can also be obtained by a reaction with aminoethoxy silane followed by succinic anhydride.

However, non-hydrolytically synthesized MNPs lack surface hydroxyl groups, which are essential to the formation of the Si-O-M bond. To overcome this limitation, Yi *et al.* utilized a base-catalyzed sol-gel reaction in an inverse micelle.[286] The use of base not only catalyzes the sol-gel process, it also peels off hydrophobic surfactants and provides MNPs with hydroxyl groups. Based on a modification of Yi's method, Cheon's research group synthesized metal-doped ferrite@SiO_2 MNPs with uniform and precisely controlled SiO_2 thickness.[287-289] Yoon and colleagues developed silica-coated multi-core MNPs with high magnetic properties.[128] The so-called pomegranate-shaped MNP@SiO_2 is prepared through clustering the $MnFe_2O_4$ MNPs with PVP followed by silica coating using the Stöber method. The resulting MNPs show high colloidal stability in aqueous media and exhibit high T_2 MRI relaxivity.

7. Conjugation Chemistries for magnetic nanoparticles

MNPs can easily be functionalized with targeting molecules, such as antibodies, proteins, peptides, nucleic acids and small molecules, and they can take advantage of the enhanced binding affinity conferred by multi-valency. Currently, various efficient conjugation strategies, which can be categorized into covalent conjugation and non-covalent conjugation, are utilized. The choice of conjugation strategy is determined by the nature of the MNP surface ligands and their available functional groups, the characteristics of targeting molecules, and the desired POC application. For example, understanding the functional groups available on an antibody is crucial to choosing the best method for modification. In particular, primary amines (lysines) are prominently found within the antigen-binding site of the antibody.[290] Therefore, labeling antibody through the primary amine can occasionally cause a significant decrease in the antigen-binding activity of the antibody. This drawback can be overcome by utilizing the hydroxyl group of the antibody.[291] The following paragraphs will highlight several conjugation strategies that are commonly used for MNP surface functionalization. In more recent years, bioorthogonal methods have become favored given the small footprint, rapid conjugation, site specific attachment capabilities and high efficiency.[292]

7.1. Covalent conjugation

The use of covalent linkages has been the primary methods of choice for introducing targeting molecules to MNPs. Covalent bonds can be formed between functional groups such as amine ($-NH_2$), carboxylic acid (-COOH), and sulfhydryl (-SH), at the MNP surface and targeting molecules. Bioorthogonal click chemistry that facilitates cross-linking between alkynes and azides ($-N_3$) is another widely utilized covalent conjugation method. Alternatively, a coordination bond, also called as a dative covalent bond, between metals and metal binding amino acids can be utilized. A number of straightforward protocols are available for linking those functional groups.

7.1.1. Conventional covalent linkage chemistry—The most common and versatile techniques for covalent conjugation involve the use of chemical groups that readily react with functional groups on MNPs (Fig. 17a). There are numerous synthetic reactive groups that form covalent bonds with functional groups.[293] Chemicals, including aldehydes, anhydrides, epoxides, isothiocyanates, and NHS ester (N-hydroxysuccinimide), are popular amine-specific reactive groups that are usually incorporated in MNP functionalization. In the case of carboxylic acid, few chemicals are known to conjugate to them. Carbodiimide compounds (*i.e.*, 1-Ethyl-3-[3-dimethylaminopropyl]carbodiimide hydrochloride (EDC)) are useful for labeling carboxylic acids. They can activate carboxylic acids for direct conjugation to primary amines via amide bonds. The sulfhydryl reactive groups include maleimides, haloacetyls, and pyridyl disulfides. These chemicals form stable thioether linkages or disulfide bonds upon reaction with sulfhydryl groups.

However, because targeting molecules usually lack reactive groups, they are modified prior to conjugation. In this sense, the most common strategies are the use of bifunctional cross-linkers, which possess two reactive groups at both ends.[293] They can be categorized into

homobifunctional or heterobifunctional molecules depending on the reactive groups. For example, bis(sulfosuccinimidyl)suberate, which has two NHS esters at each end of a carbon spacer arm, is a homobifunctional cross-linker that allows for amine-to-amine cross-linking. Sulfosuccinimidyl-4-(N-maleimidomethyl)cyclohexane-1-carboxylate (Sulfo-SMCC) containing a maleimide group and NHS ester is a heterobifunctional cross-linker for amine-to-sulfhydryl cross-linking. For carboxylic acid-to-amine coupling, zero-length cross-linker EDC can be utilized. EDC functions by converting carboxyls into amine-reactive isourea intermediates that bind to the primary amine. Unlike other heterobifunctional cross-linkers, EDC only serves as a catalyst for covalent bond formation.

The use of cross-linker molecules not only facilitates covalent bond formation, it also provides better conjugation efficiency. Steric hindrance around the MNPs can interfere with the cross-linking reactions, making it more difficult to label targeting molecules.[294] Highly flexible bifunctional cross-linkers with long carbon chain allow for bio-conjugation without steric hindrance, increasing the number and activity of targeting molecules attached on MNPs.[295-297] One typical drawback of cross-linkers is MNP clusterization, which is induced by inter-particle cross-linking.[223, 298] To prevent such undesirable cross-linking, several reaction steps, including functional group protection, stepwise modification, or a number of purification processes, are required. Nevertheless, those additional steps often result in a low product yield.

7.1.2. Bioorthogonal chemistry—An emerging concept in conjugation chemistry is bioorthogonality, which is defined by a chemical reaction that occurs inside living systems without interfering with native biochemical processes.[298, 299] Reactions are considered bioorthogonal when the two reactive groups are highly selective for each other and inert for the other functional groups present in biological systems.[300] The reaction should proceed in mild conditions, such as water at or near neutral pH, and temperature between 25 and 37 °C, and it does not involve cytotoxic reagents or by-products. Bioorthogonal conjugation has become one of the preferred methods of attaching targeting molecules to MNPs.

As a subclass of bioorthogonal chemistry, click chemistry is the most common approach for meeting the afore-mentioned requirements (Fig. 17b).[301] One of the classic click reactions is the Huisgen 1,3-dipolar cycloaddition of azides and alkynes to form 1,2,3-triazoles.[302-304] When Cu(I) is used as a catalyst, this process can be accelerated ~10^8-fold. Therefore, the reaction is commonly referred to as a Cu(I)-mediated [3 + 2] azide-alkyne cycloaddition (CuAAC). Compared to other conjugation strategies, CuAAC has distinctive advantages. Azide and alkyne have very high specificity for each other and they are unreactive to other functional groups, allowing for target-specific conjugation. Additionally, the resulting covalent bond is highly stable and not susceptible to harsh biological environments. However, the use of Cu(I) species as a catalyst requires an organic solvent or anaerobic conditions, which are not desirable in bioconjugation reactions.[304] One approach for tackling this issue is the utilization of water-soluble Cu(II) species (*e.g.*, $CuSO_4$) and ascorbic acids that reduce Cu(II) into Cu(I).[305, 306] This allows for CuAAC to proceed under mild aerobic aqueous conditions. The other approach is Cu-free click chemistry, which takes advantage of strained alkynes (*e.g.*, difluorinated cyclooctyne).[307, 308] The cyclooctyne is self-activated by its ring strain and electron-withdrawing fluorine, enabling the reaction to

take place with kinetics that are comparable to CuAAC. The elimination of cytotoxic copper catalyst makes Cu-free click chemistry biocompatible and suitable for application within various MNP bioconjugation processes. Nevertheless, the reaction is still limited by the poor aqueous solubility of substrates and tedious syntheses.[308]

Another example of a click reaction is Staudinger ligation.[309] This reaction utilizes an azide and ester containing aryl phosphine to induce an iminophosphorane (aza-ylide) intermediate. The aza-ylide undergoes spontaneous intra-molecular cyclization, resulting in a stable amide bond. This reaction is biocompatible because it can proceed in a mild aqueous environment and does not require any catalysts or organic solvents. One limitation of this chemistry is the oxidation of phosphine in ambient conditions, which will cause a decreased reactivity and low production yield. Excess amounts of reagents are required to overcome this issue.[310]

The other click reaction is the Diels-Alder reaction, which is [4 + 2]-cycloaddition between a dienophile and diene.[311] This reaction works in aqueous buffers, at or near room temperature, and in a highly selective and efficient manner without the formation of by-products. Recently, a reaction between a 1,2,4,5-tetrazine (Tz) and a trans-cyclooctene (TCO), which is a derivative of Dieal-Alder reaction, was introduced as an effective chemistry for MNP bioconjugation.[312-314] This Tz-TCO chemistry, pioneered by the Weissleder's research group, benefits from the high aqueous stability of Tz molecules, high reactivity of strained TCO, sufficiently rapid kinetics, and lack of a need for a catalyst. Termed bioorthogonal nanoparticle detection (BOND), this technique provides a novel targeting platform in which Tz and TCO act as the coupling agents between MNPs and targeting antibodies (Fig. 17c). Haun *et al.* demonstrated the utility of this reaction for cell-specific amplification of MNP binding which can be utilized to detect various biomolecules such as protein biomarkers.[292, 315, 316] To facilitate this process, amine-functionalized MNPs are first modified with an NHS ester derivative of Tz to create Tz-MNPs. Targeting antibodies are modified with NHS containing TCO. In a two-step labeling strategy (BOND-2), the TCO-modified antibodies are first used for target (e.g., cancer cell) binding followed by covalent reaction with Tz-MNP.[292, 317] The robust conjugation reaction of BOND-2 allows for higher MNP binding to targets compared to other conjugation techniques, resulting in a significantly improved detection sensitivity in the NMR-based sensor system. Moreover, this platform is capable of performing rapid, multiplexed analysis of human tumors and is broadly applicable for bio-medical use.[44, 315, 317]

7.1.3. Amino acid-metal dative bonding—A dative covalent bond (coordination bond) is a covalent bond in which both electrons come from the same atom. Several amino acids can form dative covalent bond with specific metals. For example, cysteine coordinatively binds to copper and gold through its sulfydryl side-chains.[318] This characteristic coordination bonding between amino acid and metal can serve as a novel bio-conjugation method. The most widely used combination is polyhistidine (His_n) and divalent nickel (Ni^{2+})-chelated nitrilotriacetic acid (NTA) (Fig. 18a).[319, 320] The high affinity of His_n and Ni-NTA interaction is characterized by a small dissociation constant of 10^{-13} M. To facilitate His_n-Ni-NTA mediated bio-conjugation, NTA is first labeled on the surface of MNPs using conventional covalent conjugation chemistry, which is followed by Ni^{2+} chelation.[235, 321, 322] Targeting molecules that contain a His_n-motif are then conjugated with MNPs.

Because a variety of biomolecules can be chemically modified to display a His_n tag, this conjugation strategy has applicability beyond proteins or peptides.[323]

In combination with MNPs, the His_n-Ni-NTA interaction can be an efficient and selective method for magnetic separation and purification of His_n-tagged proteins or cells. Xu and co-workers synthesized Ni-NTA-modified MNPs of FePt and $Co@Fe_2O_3$ and demonstrated their ability to separate His-tagged proteins.[235, 321] According to a study by Kim *et al.*, a high density of Ni-NTA present on the MNP surface enhances the protein purification capacity.[322] Kim and co-workers reported the use of Fe_2O_3@NiO MNPs for NTA free capture of His_n-tagged proteins.[324] In particular, the MNPs themselves have affinity to His tags, owing to the presence of Ni^{2+} ions on the surface.[324, 325] Therefore, no additional Ni-NTA conjugation process is required.

7.2. Non-covalent conjugation

Non-covalent conjugations differ from covalent conjugation in that they do not share electrons, but they take advantage of a variety of interactions, such as hydrogen bonding, van der Waals interaction, π-interaction, and hydrophobic interaction.[326] In general, non-covalent bonds are much weaker than covalent bonds. The bond-dissociation energy of noncovalent bonds is only 1–5 kcal/mol while that of a covalent bond is an order of magnitude larger.[326] However, cooperative, multiple non-covalent interactions can produce highly stable, specific linkages between different molecules.

Several non-covalent interactions, including affinity, electrostatic, and hydrophilic interactions, are available for conjugation of targeting molecules to MNPs (Fig. 18b).[225, 327] Among them, the avidin-biotin affinity interaction is one of the widely exploited strategies due to its exceptional bond strength (dissociation constant, $K_d = 10^{-15}$ M), which is comparable to that of a covalent bond.[328] The bond formation is very rapid, and once formed, the bond is stable under extreme pH, temperature, organic solvent, and other denaturing agent conditions.[293, 328, 329] The high affinity is originated from an extensive network of hydrogen bonds, and there is high shape complementarity between the avidin binding pocket and biotin.[321] Avidin can interact with up to four biotin molecules, owing to its homotetrameric subunit structure, and each subunit is capable of binding to one biotin. Avidin-biotin conjugation is usually conducted via a two-step reaction.[240, 292, 328, 330-332] First, targeting molecules and MNPs are functionalized with avidin and biotin (or *vice versa*). Because biotin is relatively small (244.3 Daltons), it can be labeled on many targeting molecules without significantly altering their functionalities.[333] Typically, biotin is cross-linked with amine or sulfhydryl functional groups using reactive biotin reagents, such as NHS-biotin and maleimide-biotin. Avidin can be labeled to the surface coatings of MNPs via various covalent conjugation chemistries. Then, avidin-coated MNPs are reacted with biotinylated molecules, leading to target molecule-conjugated MNPs. Although the avidin-biotin interaction is robust, it often suffers from the non-specific binding of avidin, which originates from avidin's high carbohydrate content and isoelectric point (pI, ~10).[334] This issue can be solved by chemical deglycosylation of avidin.[335] As an alternative, streptavidin, which lacks carbohydrates and has a low pI of 5–6 can be used.[336]

A number of studies utilizing avidin-biotin interactions have been reported. Most of them take advantage of the interaction to conjugate targeting molecules to MNPs.[240, 292, 330-332] Recently, the interaction was applied as a model system to demonstrate proof-of-concept of new MNP-based biosensing platforms.[23, 128, 337-340] The avidin-biotin system can be a good model in such sensing platforms due to its high affinity, albeit adding considerable bulk. Yoon *et al.* utilized avidin-biotin interactions to demonstrate a magnetic resonance-based biosensor.[128] In this system, biotinylated Fe@$MnFe_2O_4$ MNPs are clustered by avidin, resulting in an avidin dose-dependent change of the T_2. Ilyas and colleagues biotinylated Fe_3O_4 MNPs to detect streptavidin-functionalized proteins.[339] The strong affinity between biotin and streptavidin allows for sensitive detection of streptavidin-bearing horseradish peroxidase using a chemiluminescent assay. Ranzoni and co-workers conjugated biotinylated antibodies to streptavidin-coated MNPs for prostate specific antigen (PSA) detection.[340] In the presence of PSA, antibody-MNPs are clustered and those clusters are detected by optical scattering at applied magnetic rotation frequencies.

8. Clinical Applications

Magnetic POC technologies continue to evolve with ever increasing sensitivities, proffered by advances in MNP design, amplification strategies and sensitive detectors. Collectively, the different technologies have now been used to detect and phenotype whole cells, exosomes, bacteria, viruses, proteins, drugs and nucleic acids in unprocessed biological samples.[341-343] The main clinical applications to date have been for cancer and infectious disease detection. Some of these devices and assays are entering the market place (see Table 1). One example is T2Biosystems, a company using NMR to develop applications aimed at lowering mortality rates, improving patient outcomes and reducing the cost of healthcare. Their T2Dx Instrument and T2Candida Panel have already received marketing authorization from the U.S. Food and Drug Administration. Another platform, Magnotech by developed by Philips,[108] has been applied to detect cardiac troponin I (cTnI) for diagnosis of acute myocardial infarction. For the *ex-vivo* POC applications, the stringent requirement for MNP biodegradation and biocompatibility could be relaxed; more critical particle requirements are high magnetic moments, colloidal stability, and the ease of bioconjugation. As such, many commercially-available or custom-designed MNPs have been used in combination with these detection systems.

8.1. Infection

Several different approaches to bacterial detection have been explored, including antibody or protein-based diagnostics[344], magnetic Gram-staining,[49], antibiotic-based diagnostics,[48] and fast magnetogenetic profiling technologies.[50, 52] The latter approach is particularly robust and enables rapid bacterial analyses of 16S rRNA in minimally processed samples[50] as well as bacterial DNA.[52, 176, 345]. Figure 19 summarizes the principle of the magnetogenetic profiling technique.[52] Furthermore, fungal detection studies have shown that magnetogenetic detection is a rapid, automation-amenable opportunity for clinicians to detect and identify multiple human pathogens within hours of sample collection.[279] In essence, the magnetic detection technology, particularly the μNMR, is quite mature and consequently is being commercialized for molecular testings of other pathogens.[279, 346, 347]

8.2. Cancer

There is a need to more effectively detect and phenotype cancers. Such molecular analyses will rely on measuring multiple (dozens to hundreds of) proteins and nucleic acids (mRNA, miRNA, DNA) originating from cancer cells. Developments in this direction will be invaluable for earlier cancer detection, mapping of heterogeneity, analysis of drug response and resistance or recurrence. For example, the μNMR technology has been used clinically to detect cancer cells and to perform rapid profiling during fine needle aspirations in 70 patients.[315] These studies were expanded to apply the same technology to the detection of circulating tumor cells in blood of 25 patients[46] and to lung cancer phenotyping in 47 patients.[47] The technology has also been used successfully for exosome profiling in glioblastoma.[43] It is likely that related technologies, also relying on nanoparticles,[348] will continue to emerge to further improve the detection sensitivities.

8.3. Coagulation

Rapidly assessing hemostatic parameters is an important task in hospital settings (surgical and interventional practices) as well as in the battlefield and trauma settings. For example, approximately 25% of trauma patients have impaired hemostasis, which frequently goes undetected during the initial hospitalization. According to a study in the Journal of the American College of Surgeons, for trauma patients with symptoms of impaired hemostasis, mortality was reduced from 45% to 19% with more rapid delivery of therapy. Existing approaches, however, require multiple platform, generally consume 1–25 mL of sample and take hours to provide results. NMR system has been used to provide comprehensive blood clotting measurements in less than 20 minutes Commercialized by T2Biosystems as T2 HemoStat, the system measures clotting time, fibrinolysis, platelet activity, clot contraction and clot lysis. The test is based on the unique fact that in normal clots, paramagnetic red blood cells form closely packed polyhedral structures (polyhedrocytes) with platelets and fibrin, which leads to concomitant changes in transverse relaxation time.[349] The platform allows for comprehensive assessment of hemostatic parameters on a single instrument and provides results within 15 min using 0.04 mL of blood with minimal sample handling.

8.4. Other applications

The above clinical applications represent a few examples of what is possible. We expect that many more applications will be developed, now that highly efficient magnetic nanoparticles, sensors and imaging systems have become mainstream. These applications include measurements of circulating protein biomarker,[62, 350] exosomes[43], viruses[179], drugs,[108] and metabolites[351] among others.

9. Conclusion and Perspectives

Magnetic POC technologies have seen a spectacular rise over the last few years for good reasons. Compared to other approaches, they enable analyses in “dirty” samples, i.e, without major purification. This is possible because human tissue samples are usually devoid of superparamagnetism. Because measurements can be directly done in virtually any body fluids and samples, it eliminates potential sample loss and speeds up the analysis. Combined with genetic detection technologies,[52, 176, 345] the analytical possibilities are endless.

We believe that there are a number of future developments which could make magnetic detection technologies even more widespread: (i) for early disease detection where lives can be saved and treatments are affordable, (ii) for the detection of diseases other than cancer and infection, (iii) for the use in consumer goods, agriculture and food/water safety, (iv) in applications where magnetic separation and analysis are integrated in a single chip, and (v) for multi-functional sensors combining magnetism with other modalities. It is these specific applications that will drive the need for new nanoparticle characteristics, affinity ligands and magnetic sensing devices.

Acknowledgments

The authors thank Dr. Huilin Shao (MGH) for reviewing the manuscript. This work was supported in part by NIH Grants R01EB004626, R01EB010011, HHSN268201000044C, R01HL113156, U54-CA119349, and K12CA087723-09; DoD OCRP Award W81XWH-14-1-0279; the National Creative Research Initiative (2010-0018286 J.C.), and the Korea Healthcare Technology R&D Project, Ministry for Health & Welfare Affairs (HI08C2149 J.C.).

References

1. Gubala V, Harris LF, Ricco AJ, Tan MX, Williams DE. Point of Care Diagnostics: Status and Future. Anal Chem. 2012; 84:487–515. [PubMed: 22221172]
2. Ryan F, O'Shea S, Byrne S. The 'Carry-Over' Effects of Patient Self-Testing: Positive Effects on Usual Care Management by an Anticoagulation Management Service. Thromb Res. 2010; 126:e345–e348. [PubMed: 20828796]
3. von Lode P. Point-of-Care Immunotesting: Approaching the Analytical Performance of Central Laboratory Methods. Clin Biochem. 2005; 38:591–606. [PubMed: 16009140]
4. Varmus H, Kumar HS. Addressing the Growing International Challenge of Cancer: A Multinational Perspective. Sci Transl Med. 2013; 5:175cm2.
5. Wang J. Electrochemical Glucose Biosensors. Chem Rev. 2008; 108:814–825. [PubMed: 18154363]
6. Beneteau-Burnat B, Bocque MC, Lorin A, Martin C, Vaubourdolle M. Evaluation of the Blood Gas Analyzer GEM PREMIER 3000. Clin Chem Lab Med. 2004; 42:96–101. [PubMed: 15061388]
7. Christenson RH, Azzazy HM. Cardiac Point of Care Testing: A Focused Review of Current National Academy of Clinical Biochemistry Guidelines and Measurement Platforms. Clin Biochem. 2009; 42:150–157. [PubMed: 18929551]
8. McDonnell B, Hearty S, Leonard P, O'Kennedy R. Cardiac Biomarkers and the Case for Point-of-Care Testing. Clin Biochem. 2009; 42:549–561. [PubMed: 19318022]
9. Lewandrowski K, Flood J, Finn C, Tannous B, Farris AB, Benzer TI, Lee-Lewandrowski E. Implementation of Point-of-Care Rapid Urine Testing for Drugs of Abuse in the Emergency Department of an Academic Medical Center: Impact on Test Utilization and Ed Length of Stay. Am J Clin Pathol. 2008; 129:796–801. [PubMed: 18426741]
10. Cervinski MA, Gronowski AM. Reproductive-Endocrine Point-of-Care Testing: Current Status and Limitations. Clin Chem Lab Med. 2010; 48:935–942. [PubMed: 20446758]
11. Kok L, Elias SG, Witteman BJ, Goedhard JG, Muris JW, Moons KG, de Wit NJ. Diagnostic Accuracy of Point-of-Care Fecal Calprotectin and Immunochemical Occult Blood Tests for Diagnosis of Organic Bowel Disease in Primary Care: The Cost-Effectiveness of a Decision Rule for Abdominal Complaints in Primary Care (CEDAR) Study. Clin Chem. 2012; 58:989–998. [PubMed: 22407858]
12. Curtis CM, Kost GJ, Louie RF, Sonu RJ, Ammirati EB, Sumner S. Point-of-Care Hematology and Coagulation Testing in Primary, Rural Emergency, and Disaster Care Scenarios. Point Care. 2012; 11:140–145. [PubMed: 23843728]
13. Taylor JR, Lopez LM. Cholesterol: Point-of-Care Testing. Ann Pharmacother. 2004; 38:1252–1257. [PubMed: 15178733]

14. Dheda K, Ruhwald M, Theron G, Peter J, Yam WC. Point-of-Care Diagnosis of Tuberculosis: Past, Present and Future. Respirology. 2013; 18:217–232. [PubMed: 23190246]
15. Park S, Zhang Y, Lin S, Wang TH, Yang S. Advances in Microfluidic PCR for Point-of-Care Infectious Disease Diagnostics. Biotechnol Adv. 2011; 29:830–839. [PubMed: 21741465]
16. Castro CM, Ghazani AA, Chung J, Shao H, Issadore D, Yoon TJ, Weissleder R, Lee H. Miniaturized Nuclear Magnetic Resonance Platform for Detection and Profiling of Circulating Tumor Cells. Lab Chip. 2014; 14:14–23. [PubMed: 23835814]
17. Curtis CM, Louie RF, Vy JH, Ferguson WJ, Lam M, Truong AT, Rust MJ, Kost GJ. Innovations in Point-of-Care Testing for Enhanced United States Disaster Caches. Am J Disaster Med. 2013; 8:181–204. [PubMed: 24352993]
18. Cheng MM, Cuda G, Bunimovich YL, Gaspari M, Heath JR, Hill HD, Mirkin CA, Nijdam AJ, Terracciano R, Thundat T, Ferrari M. Nanotechnologies for Biomolecular Detection and Medical Diagnostics. Curr Opin Chem Biol. 2006; 10:11–19. [PubMed: 16418011]
19. Giljohann DA, Mirkin CA. Drivers of Biodiagnostic Development. Nature. 2009; 462:461–464. [PubMed: 19940916]
20. Sun T, Holmes D, Gawad S, Green NG, Morgan H. High Speed Multi-Frequency Impedance Analysis of Single Particles in a Microfluidic Cytometer Using Maximum Length Sequences. Lab Chip. 2007; 7:1034–1040. [PubMed: 17653346]
21. Ellerbee AK, Phillips ST, Siegel AC, Mirica KA, Martinez AW, Striehl P, Jain N, Prentiss M, Whitesides GM. Quantifying Colorimetric Assays in Paper-Based Microfluidic Devices by Measuring the Transmission of Light through Paper. Anal Chem. 2009; 81:8447–8452. [PubMed: 19722495]
22. Myers FB, Lee LP. Innovations in Optical Microfluidic Technologies for Point-of-Care Diagnostics. Lab Chip. 2008; 8:2015–2031. [PubMed: 19023464]
23. Lee H, Sun E, Ham D, Weissleder R. Chip-NMR Biosensor for Detection and Molecular Analysis of Cells. Nat Med. 2008; 14:869–874. [PubMed: 18607350]
24. Issadore D, Chung J, Shao H, Liong M, Ghazani AA, Castro CM, Weissleder R, Lee H. Ultrasensitive Clinical Enumeration of Rare Cells Ex Vivo Using a Micro-Hall Detector. Sci Transl Med. 2012; 4:141ra92.
25. Gaster RS, Xu L, Han SJ, Wilson RJ, Hall DA, Osterfeld SJ, Yu H, Wang SX. Quantification of Protein Interactions and Solution Transport Using High-Density GMR Sensor Arrays. Nat Nanotechnol. 2011; 6:314–320. [PubMed: 21478869]
26. Gijs MA, Lacharme F, Lehmann U. Microfluidic Applications of Magnetic Particles for Biological Analysis and Catalysis. Chem Rev. 2010; 110:1518–1563. [PubMed: 19961177]
27. Plouffe BD, Murthy SK, Lewis LH. Fundamentals and Application of Magnetic Particles in Cell Isolation and Enrichment: A Review. Rep Prog Phys. 2014; 78:016601. [PubMed: 25471081]
28. Chalmers JJ, Zborowski M, Sun L, Moore L. Flow through, Immunomagnetic Cell Separation. Biotechnol Prog. 1998; 14:141–148. [PubMed: 9496679]
29. Zborowski M, Chalmers JJ. Magnetic cell separation; Elsevier: Amsterdam; Boston. 2008:xviii. 454 p., [14] p. of plates.
30. Miltenyi S, Muller W, Weichel W, Radbruch A. High Gradient Magnetic Cell Separation with MACS. Cytometry. 1990; 11:231–238. [PubMed: 1690625]
31. Harisinghani MG, Barentsz J, Hahn PF, Deserno WM, Tabatabaei S, van de Kaa CH, de la Rosette J, Weissleder R. Noninvasive Detection of Clinically Occult Lymph-Node Metastases in Prostate Cancer. N Engl J Med. 2003; 348:2491–2499. [PubMed: 12815134]
32. Weissleder R, Reimer P, Lee AS, Wittenberg J, Brady TJ. MR Receptor Imaging: Ultrasmall Iron Oxide Particles Targeted to Asialoglycoprotein Receptors. Am J Roentgenol. 1990; 155:1161–1167. [PubMed: 2122660]
33. Weissleder R, Elizondo G, Wittenberg J, Lee AS, Josephson L, Brady TJ. Ultrasmall Superparamagnetic Iron Oxide: An Intravenous Contrast Agent for Assessing Lymph Nodes with MR Imaging. Radiology. 1990; 175:494–498. [PubMed: 2326475]
34. Harisinghani M, Ross RW, Guimaraes AR, Weissleder R. Utility of a New Bolus-Injectable Nanoparticle for Clinical Cancer Staging. Neoplasia. 2007; 9:1160–1165. [PubMed: 18084623]

35. Shaw SY, Westly EC, Pittet MJ, Subramanian A, Schreiber SL, Weissleder R. Perturbational Profiling of Nanomaterial Biologic Activity. Proc Natl Acad Sci U S A. 2008; 105:7387–7392. [PubMed: 18492802]
36. Krishnan KM. Biomedical Nanomagnetics: A Spin through Possibilities in Imaging, Diagnostics, and Therapy. IEEE Trans Magn. 2010; 46:2523–2558. [PubMed: 20930943]
37. Pankhurst QA, Connolly J, Jones SK, Dobson J. Applications of Magnetic Nanoparticles in Biomedicine. J Phys D: Appl Phys. 2003; 36:R167–R181.
38. Issadore D, Park YI, Shao H, Min C, Lee K, Liong M, Weissleder R, Lee H. Magnetic Sensing Technology for Molecular Analyses. Lab Chip. 2014; 14:2385–2397. [PubMed: 24887807]
39. Gillis P, Koenig SH. Transverse Relaxation of Solvent Protons Induced by Magnetized Spheres: Application to Ferritin, Erythrocytes, and Magnetite. Magn Reson Med. 1987; 5:323–345. [PubMed: 2824967]
40. Danieli E, Perlo J, Blumich B, Casanova F. Small Magnets for Portable NMR Spectrometers. Angew Chem Int Ed Engl. 2010; 49:4133–4135. [PubMed: 20446281]
41. Liu Y, Sun N, Lee H, Weissleder R, Ham D. CMOS Mini Nuclear Magnetic Resonance System and Its Application for Biomolecular Sensing. IEEE ISSCC Dig Tech Papers. 2008; 1:140–602.
42. Massin C, Vincent F, Homsy A, Ehrmann K, Boero G, Besse PA, Daridon A, Verpoorte E, de Rooij NF, Popovic RS. Planar Microcoil-Based Microfluidic NMR Probes. J Magn Reson. 2003; 164:242–255. [PubMed: 14511593]
43. Shao H, Chung J, Balaj L, Charest A, Bigner DD, Carter BS, Hochberg FH, Breakefield XO, Weissleder R, Lee H. Protein Typing of Circulating Microvesicles Allows Real-Time Monitoring of Glioblastoma Therapy. Nat Med. 2012; 18:1835–1840. [PubMed: 23142818]
44. Lee H, Yoon TJ, Figueiredo JL, Swirski FK, Weissleder R. Rapid Detection and Profiling of Cancer Cells in Fine-Needle Aspirates. Proc Natl Acad Sci U S A. 2009; 106:12459–12464. [PubMed: 19620715]
45. Issadore D, Min C, Liong M, Chung J, Weissleder R, Lee H. Miniature Magnetic Resonance System for Point-of-Care Diagnostics. Lab Chip. 2011; 11:2282–2287. [PubMed: 21547317]
46. Ghazani AA, Castro CM, Gorbatov R, Lee H, Weissleder R. Sensitive and Direct Detection of Circulating Tumor Cells by Multimarker μ-Nuclear Magnetic Resonance. Neoplasia. 2012; 14:388–395. [PubMed: 22745585]
47. Ghazani AA, McDermott S, Pectasides M, Sebas M, Mino-Kenudson M, Lee H, Weissleder R, Castro CM. Comparison of Select Cancer Biomarkers in Human Circulating and Bulk Tumor Cells Using Magnetic Nanoparticles and a Miniaturized Micro-NMR System. Nanomedicine. 2013; 9:1009–1017. [PubMed: 23570873]
48. Chung HJ, Reiner T, Budin G, Min C, Liong M, Issadore D, Lee H, Weissleder R. Ubiquitous Detection of Gram-Positive Bacteria with Bioorthogonal Magnetofluorescent Nanoparticles. ACS Nano. 2011; 5:8834–8841. [PubMed: 21967150]
49. Budin G, Chung HJ, Lee H, Weissleder R. A Magnetic Gram Stain for Bacterial Detection. Angew Chem Int Ed Engl. 2012; 51:7752–7755. [PubMed: 22744868]
50. Chung HJ, Castro CM, Im H, Lee H, Weissleder R. A Magneto-DNA Nanoparticle System for Rapid Detection and Phenotyping of Bacteria. Nat Nanotechnol. 2013; 8:369–375. [PubMed: 23644570]
51. Liong M, Fernandez-Suarez M, Issadore D, Min C, Tassa C, Reiner T, Fortune SM, Toner M, Lee H, Weissleder R. Specific Pathogen Detection Using Bioorthogonal Chemistry and Diagnostic Magnetic Resonance. Bioconjug Chem. 2011; 22:2390–2394. [PubMed: 22043803]
52. Liong M, Hoang AN, Chung J, Gural N, Ford CB, Min C, Shah RR, Ahmad R, Fernandez-Suarez M, Fortune SM, Toner M, Lee H, Weissleder R. Magnetic Barcode Assay for Genetic Detection of Pathogens. Nat Commun. 2013; 4:1752. [PubMed: 23612293]
53. Rho J, Chung J, Im H, Liong M, Shao H, Castro CM, Weissleder R, Lee H. Magnetic Nanosensor for Detection and Profiling of Erythrocyte-Derived Microvesicles. ACS Nano. 2013; 7:11227–11233. [PubMed: 24295203]
54. Connolly J, St P, Timothy G. Proposed Biosensors Based on Time-Dependent Properties of Magnetic Fluids. J Magn Magn Mater. 2001; 225:156–160.

55. Stromberg M, Zardan Gomez de la Torre T, Goransson J, Gunnarsson K, Nilsson M, Svedlindh P, Stromme M. Multiplex Detection of DNA Sequences Using the Volume-Amplified Magnetic Nanobead Detection Assay. Anal Chem. 2009; 81:3398–3406. [PubMed: 19334737]
56. Park K, Harrah T, Goldberg EB, Guertin RP, Sonkusale S. Multiplexed Sensing Based on Brownian Relaxation of Magnetic Nanoparticles Using a Compact AC Susceptometer. Nanotechnology. 2011; 22:085501. [PubMed: 21242618]
57. Astalan AP, Ahrentorp F, Johansson C, Larsson K, Krozer A. Biomolecular Reactions Studied Using Changes in Brownian Rotation Dynamics of Magnetic Particles. Biosens Bioelectron. 2004; 19:945–951. [PubMed: 15128114]
58. Grossman HL, Myers WR, Vreeland VJ, Bruehl R, Alper MD, Bertozzi CR, Clarke J. Detection of Bacteria in Suspension by Using a Superconducting Quantum Interference Device. Proc Natl Acad Sci U S A. 2004; 101:129–134. [PubMed: 14688406]
59. Hall DA, Gaster RS, Makinwa K, Wang SX, Murmann B. A 256 Pixel Magnetoresistive Biosensor Microarray in 0.18 μm CMOS. IEEE J Solid-State Circuits. 2013; 48:1290–1301. [PubMed: 24761029]
60. Baselt DR, Lee GU, Natesan M, Metzger SW, Sheehan PE, Colton RJ. A Biosensor Based on Magnetoresistance Technology. Biosens Bioelectron. 1998; 13:731–739. [PubMed: 9828367]
61. Osterfeld SJ, Yu H, Gaster RS, Caramuta S, Xu L, Han SJ, Hall DA, Wilson RJ, Sun S, White RL, Davis RW, Pourmand N, Wang SX. Multiplex Protein Assays Based on Real-Time Magnetic Nanotag Sensing. Proc Natl Acad Sci U S A. 2008; 105:20637–20640. [PubMed: 19074273]
62. Gaster RS, Hall DA, Nielsen CH, Osterfeld SJ, Yu H, Mach KE, Wilson RJ, Murmann B, Liao JC, Gambhir SS, Wang SX. Matrix-Insensitive Protein Assays Push the Limits of Biosensors in Medicine. Nat Med. 2009; 15:1327–1332. [PubMed: 19820717]
63. Besse PA, Boero G, Demierre M, Pott V, Popovic R. Detection of a Single Magnetic Microbead Using a Miniaturized Silicon Hall Sensor. Appl Phys Lett. 2002; 80:4199.
64. Mihajlovik G, Xiong P, Stephan von M, Ohtani K, Ohno H, Field M, Sullivan GJ. Detection of Single Magnetic Bead for Biological Applications Using an InAs Quantum-Well Micro-Hall Sensor. Appl Phys Lett. 2005; 87:112502.
65. Togawa K, Sanbonsugi H, Lapicki A, Abe M, Handa H, Sandhu A. High-Sensitivity InSb Thin-Film Micro-Hall Sensor Arrays for Simultaneous Multiple Detection of Magnetic Beads for Biomedical Applications. IEEE Trans Magn. 2005; 41:3661–3663.
66. Aytur T, Foley J, Anwar M, Boser B, Harris E, Beatty PR. A Novel Magnetic Bead Bioassay Platform Using a Microchip-Based Sensor for Infectious Disease Diagnosis. J Immunol Methods. 2006; 314:21–29. [PubMed: 16842813]
67. Gambini S, Skucha K, Liu PP, Kim J, Krigel R. A 10 kPixel CMOS Hall Sensor Array with Baseline Suppression and Parallel Readout for Immunoassays. IEEE J Solid-State Circuits. 2013; 48:302–317.
68. Liu PP, Skucha K, Duan Y, Megens M, Kim J, Izyumin II, Gambini S, Boser B. Magnetic Relaxation Detector for Microbead Labels. IEEE J Solid-State Circuits. 2012; 47:1056–1064. [PubMed: 25308988]
69. Issadore D, Chung HJ, Chung J, Budin G, Weissleder R, Lee H. μHall Chip for Sensitive Detection of Bacteria. Adv Healthc Mater. 2013; 2:1224–1228. [PubMed: 23495188]
70. Balasubramanian G, Chan IY, Kolesov R, Al-Hmoud M, Tisler J, Shin C, Kim C, Wojcik A, Hemmer PR, Krueger A, Hanke T, Leitenstorfer A, Bratschitsch R, Jelezko F, Wrachtrup J. Nanoscale Imaging Magnetometry with Diamond Spins Under Ambient Conditions. Nature. 2008; 455:648–651. [PubMed: 18833276]
71. Maze JR, Stanwix PL, Hodges JS, Hong S, Taylor JM, Cappellaro P, Jiang L, Dutt MV, Togan E, Zibrov AS, Yacoby A, Walsworth RL, Lukin MD. Nanoscale Magnetic Sensing with an Individual Electronic Spin in Diamond. Nature. 2008; 455:644–647. [PubMed: 18833275]
72. Taylor JM, Cappellaro P, Childress L, Jiang L, Budker D, Hemmer PR, Yacoby A, Walsworth R, Lukin MD. High-Sensitivity Diamond Magnetometer with Nanoscale Resolution. Nat Phys. 2008; 4:810–816.

73. Waldherr G, Beck J, Neumann P, Said RS, Nitsche M, Markham ML, Twitchen DJ, Twamley J, Jelezko F, Wrachtrup J. High-Dynamic-Range Magnetometry with a Single Nuclear Spin in Diamond. Nat Nanotechnol. 2012; 7:105–108.
74. Budker, D., Jackson, K., Derek, F. Optical magnetometry. Cambridge University Press; 2013. p. xvii412 pages
75. Le Sage D, Arai K, Glenn DR, DeVience SJ, Pham LM, Rahn-Lee L, Lukin MD, Yacoby A, Komeili A, Walsworth RL. Optical Magnetic Imaging of Living Cells. Nature. 2013; 496:486–489. [PubMed: 23619694]
76. Mamin HJ, Kim M, Sherwood MH, Rettner CT, Ohno K, Awschalom DD, Rugar D. Nanoscale Nuclear Magnetic Resonance with a Nitrogen-Vacancy Spin Sensor. Science. 2013; 339:557–560. [PubMed: 23372008]
77. Staudacher T, Shi F, Pezzagna S, Meijer J, Du J, Meriles CA, Reinhard F, Wrachtrup J. Nuclear Magnetic Resonance Spectroscopy on a (5-Nanometer)^3 Sample Volume. Science. 2013; 339:561–563. [PubMed: 23372009]
78. Lara O, Tong X, Zborowski M, Chalmers JJ. Enrichment of Rare Cancer Cells through Depletion of Normal Cells Using Density and Flow-through, Immunomagnetic Cell Separation. Exp Hematol. 2004; 32:891–904. [PubMed: 15504544]
79. Choi JW, Ahn CH, Bhansali S, Henderson HT. A New Magnetic Bead-Based, Filterless Bio-Separator with Planar Electromagnet Surfaces for Integrated Bio-Detection Systems. Sens Actuators, B. 2000; 68:34–39.
80. Dupont EP, Labonne E, Vandevyver C, Lehmann U, Charbon E, Gijs MA. Monolithic Silicon Chip for Immunofluorescence Detection on Single Magnetic Beads. Anal Chem. 2010; 82:49–52. [PubMed: 19911779]
81. Lee H, Purdon AM, Westervelt RM. Manipulation of Biological Cells Using a Microelectromagnet Matrix. Appl Phys Lett. 2004; 85:1063.
82. Pamme N. Magnetism and Microfluidics. Lab Chip. 2006; 6:24–38. [PubMed: 16372066]
83. Gijs MAM. Magnetic Bead Handling On-Chip: New Opportunities for Analytical Applications. Microfluid Nanofluid. 2004; 1:22–40.
84. Xia N, Hunt TP, Mayers BT, Alsberg E, Whitesides GM, Westervelt RM, Ingber DE. Combined Microfluidic-Micromagnetic Separation of Living Cells in Continuous Flow. Biomed Microdevices. 2006; 8:299–308. [PubMed: 17003962]
85. Smistrup K, Lund-Olesen T, Hansen MF, Tang PT. Microfluidic Magnetic Separator Using an Array of Soft Magnetic Elements. J Appl Phys. 2006; 99:08P102.
86. Inglis DW, Riehn R, Austin RH, Sturm JC. Continuous Microfluidic Immunomagnetic Cell Separation. Appl Phys Lett. 2004; 85:5093.
87. Csordas A, Gerdon AE, Adams JD, Qian J, Oh SS, Xiao Y, Soh HT. Detection of Proteins in Serum by Micromagnetic Aptamer PCR (MAP) Technology. Angew Chem Int Ed Engl. 2010; 49:355–358. [PubMed: 19967683]
88. Adams JD, Kim U, Soh HT. Multitarget Magnetic Activated Cell Sorter. Proc Natl Acad Sci U S A. 2008; 105:18165–18170. [PubMed: 19015523]
89. Berger M, Castelino J, Huang R, Shah M, Austin RH. Design of a Microfabricated Magnetic Cell Separator. Electrophoresis. 2001; 22:3883–3892. [PubMed: 11700717]
90. Tibbe AG, de Grooth BG, Greve J, Liberti PA, Dolan GJ, Terstappen LW. Optical Tracking and Detection of Immunomagnetically Selected and Aligned Cells. Nat Biotechnol. 1999; 17:1210–1213. [PubMed: 10585720]
91. Choi JW, Liakopoulos TM, Ahn CH. An On-Chip Magnetic Bead Separator Using Spiral Electromagnets with Semi-Encapsulated Permalloy. Biosens Bioelectron. 2001; 16:409–416. [PubMed: 11672655]
92. Lee CS, Lee H, Westervelt RM. Microelectromagnets for the Control of Magnetic Nanoparticles. Appl Phys Lett. 2001; 79:3308.
93. Cardoso F, Jankovic J, Grossman RG, Hamilton WJ. Outcome After Stereotactic Thalamotomy for Dystonia and Hemiballismus. Neurosurgery. 1995; 36:501–7. [PubMed: 7753350]

94. Gossett DR, Weaver WM, Mach AJ, Hur SC, Tse HT, Lee W, Amini H, Di Carlo D. Label-Free Cell Separation and Sorting in Microfluidic Systems. Anal Bioanal Chem. 2010; 397:3249–3267. [PubMed: 20419490]
95. Tibbe AG, de Grooth BG, Greve J, Liberti PA, Dolan GJ, Terstappen LW. Cell Analysis System Based on Immunomagnetic Cell Selection and Alignment Followed by Immunofluorescent Analysis Using Compact Disk Technologies. Cytometry. 2001; 43:31–37. [PubMed: 11122482]
96. Chung J, Issadore D, Ullal A, Lee K, Weissleder R, Lee H. Rare Cell Isolation and Profiling on a Hybrid Magnetic/Size-Sorting Chip. Biomicrofluidics. 2013; 7:54107. [PubMed: 24404070]
97. Issadore D, Shao H, Chung J, Newton A, Pittet M, Weissleder R, Lee H. Self-Assembled Magnetic Filter for Highly Efficient Immunomagnetic Separation. Lab Chip. 2011; 11:147–151. [PubMed: 20949198]
98. Rozenfel'd EV. Calculation of the Field of a Lattice of Point Magnetic Dipoles. Phys Solid State. 2000; 42:1680–1687.
99. Pamme N, Wilhelm C. Continuous Sorting of Magnetic Cells via On-Chip Free-Flow Magnetophoresis. Lab Chip. 2006; 6:974–980. [PubMed: 16874365]
100. Kang JH, Super M, Yung CW, Cooper RM, Domansky K, Graveline AR, Mammoto T, Berthet JB, Tobin H, Cartwright MJ, Watters AL, Rottman M, Waterhouse A, Mammoto A, Gamini N, Rodas MJ, Kole A, Jiang A, Valentin TM, Diaz A, Takahashi K, Ingber DE. An Extracorporeal Blood-Cleansing Device for Sepsis Therapy. Nat Med. 2014; 20:1211–1216. [PubMed: 25216635]
101. Ramadan Q, Samper V, Poenar DP, Yu C. An Integrated Microfluidic Platform for Magnetic Microbeads Separation and Confinement. Biosens Bioelectron. 2006; 21:1693–1702. [PubMed: 16203127]
102. Lee H, Liu Y, Ham D, Westervelt RM. Integrated Cell Manipulation System-CMOS/Microfluidic Hybrid. Lab Chip. 2007; 7:331–337. [PubMed: 17330164]
103. Lehmann U, Vandevyver C, Parashar VK, Gijs MA. Droplet-Based DNA Purification in a Magnetic Lab-On-a-Chip. Angew Chem Int Ed Engl. 2006; 45:3062–3067. [PubMed: 16555359]
104. Pipper J, Inoue M, Ng LF, Neuzil P, Zhang Y, Novak L. Catching Bird Flu in a Droplet. Nat Med. 2007; 13:1259–1263. [PubMed: 17891145]
105. Koh I, Hong R, Weissleder R, Josephson L. Sensitive NMR Sensors Detect Antibodies to Influenza. Angew Chem Int Ed Engl. 2008; 47:4119–4121. [PubMed: 18428168]
106. Yang J, Wei F, Schafer C, Wong DT. Detection of Tumor Cell-Specific mRNA and Protein in Exosome-Like Microvesicles from Blood and Saliva. PLoS One. 2014; 9:e110641. [PubMed: 25397880]
107. van Reenen A, de Jong AM, den Toonder JM, Prins MW. Integrated Lab-On-Chip Biosensing Systems Based on Magnetic Particle Actuation - A Comprehensive Review. Lab Chip. 2014; 14:1966–1986. [PubMed: 24806093]
108. Bruls DM, Evers TH, Kahlman JA, van Lankvelt PJ, Ovsyanko M, Pelssers EG, Schleipen JJ, de Theije FK, Verschuren CA, van der Wijk T, van Zon JB, Dittmer WU, Immink AH, Nieuwenhuis JH, Prins MW. Rapid Integrated Biosensor for Multiplexed Immunoassays Based on Actuated Magnetic Nanoparticles. Lab Chip. 2009; 9:3504–3510. [PubMed: 20024029]
109. Ashcroft, NW., Mermin, ND. Solid State Physics. Holt, Rinehart and Winston; 1976.
110. Morales MP, Veintemillas-Verdaguer S, Montero MI, Serna CJ, Roig A, Casas L, Martínez B, Sandiumenge F. Surface and Internal Spin Canting in γ-Fe_2O_3 Nanoparticles. Chem Mater. 1999; 11:3058–3064.
111. Kim BH, Lee N, Kim H, An K, Park YI, Choi Y, Shin K, Lee Y, Kwon SG, Na HB, Park JG, Ahn TY, Kim YW, Moon WK, Choi SH, Hyeon T. Large-Scale Synthesis of Uniform and Extremely Small-Sized Iron Oxide Nanoparticles for High-Resolution T_1 Magnetic Resonance Imaging Contrast Agents. J Am Chem Soc. 2011; 133:12624–12631. [PubMed: 21744804]
112. Jun YW, Seo JW, Cheon J. Nanoscaling Laws of Magnetic Nanoparticles and Their Applicabilities in Biomedical Sciences. Acc Chem Res. 2008; 41:179–189. [PubMed: 18281944]
113. Kim D, Lee N, Park M, Kim BH, An K, Hyeon T. Synthesis of Uniform Ferrimagnetic Magnetite Nanocubes. J Am Chem Soc. 2009; 131:454–455. [PubMed: 19099480]

114. Noh SH, Na W, Jang JT, Lee JH, Lee EJ, Moon SH, Lim Y, Shin JS, Cheon J. Nanoscale Magnetism Control via Surface and Exchange Anisotropy for Optimized Ferrimagnetic Hysteresis. Nano Lett. 2012; 12:3716–3721. [PubMed: 22720795]
115. Bean CP, Livingston JD. Superparamagnetism. J Appl Phys. 1959; 30:S120.
116. Kittel C. Physical Theory of Ferromagnetic Domains. Rev Mod Phys. 1949; 21:541–583.
117. Brown W. Thermal Fluctuations of a Single-Domain Particle. Phys Rev. 1963; 130:1677–1686.
118. Standley, KJ. Oxide magnetic materials. Clarendon Press; 1972.
119. Park J, An K, Hwang Y, Park JG, Noh HJ, Kim JY, Park JH, Hwang NM, Hyeon T. Ultra-Large-Scale Syntheses of Monodisperse Nanocrystals. Nat Mater. 2004; 3:891–895. [PubMed: 15568032]
120. Chung SH, Hoffmann A, Bader SD, Liu C, Kay B, Makowski L, Chen L. Biological Sensors Based on Brownian Relaxation of Magnetic Nanoparticles. Appl Phys Lett. 2004; 85:2971.
121. Walker M, Mayo PI, O'Grady K, Charles SW, Chantrell RW. The Magnetic Properties of Single-Domain Particles with Cubic Anisotropy. I. Hysteresis Loops. J Phys Cond Mat. 1993; 5:2779–2792.
122. Rosensweig RE. Heating Magnetic Fluid with Alternating Magnetic Field. J Magn Magn Mater. 2002; 252:370–374.
123. Koenig SH, Kellar KE. Theory of $1/T_1$ and $1/T_2$ NMRD Profiles of Solutions of Magnetic Nanoparticles. Magn Reson Med. 1995; 34:227–233. [PubMed: 7476082]
124. Gossuin Y, Gillis P, Hocq A, Vuong QL, Roch A. Magnetic Resonance Relaxation Properties of Superparamagnetic Particles. Wiley Interdiscip Rev Nanomed Nanobiotechnol. 2009; 1:299–310. [PubMed: 20049798]
125. Gueron M. Nuclear Relaxation in Macromolecules by Paramagnetic Ions: A Novel Mechanism. J Magn Reson. 1975; 19:58–66.
126. Brooks RA. T_2-Shortening by Strongly Magnetized Spheres: A Chemical Exchange Model. Magn Reson Med. 2002; 47:388–391. [PubMed: 11810684]
127. Yablonskiy DA, Haacke EM. Theory of NMR Signal Behavior in Magnetically Inhomogeneous Tissues: The Static Dephasing Regime. Magn Reson Med. 1994; 32:749–763. [PubMed: 7869897]
128. Yoon TJ, Lee H, Shao H, Hilderbrand SA, Weissleder R. Multicore Assemblies Potentiate Magnetic Properties of Biomagnetic Nanoparticles. Adv Mater. 2011; 23:4793–4797. [PubMed: 21953810]
129. Leslie-Pelecky DL, Rieke RD. Magnetic Properties of Nanostructured Materials. Chem Mater. 1996; 8:1770–1783.
130. McCurrie, RA. The Structure and Properties of Ferromagnetic Materials. Academic Press; 1994.
131. Jun YW, Choi JS, Cheon J. Heterostructured Magnetic Nanoparticles: Their Versatility and High Performance Capabilities. Chem Commun. 2007:1203–1214.
132. Hyeon T. Chemical Synthesis of Magnetic Nanoparticles. Chem Commun. 2003:927–934.
133. Gupta AK, Gupta M. Synthesis and Surface Engineering of Iron Oxide Nanoparticles for Biomedical Applications. Biomaterials. 2005; 26:3995–4021. [PubMed: 15626447]
134. Sun S, Murray CB. Synthesis of Monodisperse Cobalt Nanocrystals and Their Assembly into Magnetic Superlattices. J Appl Phys. 1999; 85:4325.
135. Puntes VF, Krishnan KM, Alivisatos AP. Colloidal Nanocrystal Shape and Size Control: The Case of Cobalt. Science. 2001; 291:2115–2117. [PubMed: 11251109]
136. Osuna J, Dominique de C, Amiens C, Chaudret B, Snoeck E, Respaud M, Broto JM, Fert A. Synthesis, Characterization, and Magnetic Properties of Cobalt Nanoparticles from an Organometallic Precursor. J Phys Chem. 1996; 100:14571–14574.
137. Huber DL. Synthesis, Properties, and Applications of Iron Nanoparticles. Small. 2005; 1:482–501. [PubMed: 17193474]
138. Cordente N, Respaud M, Senocq F, Casanove MJ, Amiens C, Chaudret B. Synthesis and Magnetic Properties of Nickel Nanorods. Nano Lett. 2001; 1:565–568.
139. Dumestre F, Chaudret B, Amiens C, Renaud P, Fejes P. Superlattices of Iron Nanocubes Synthesized From $Fe[N(SiMe_3)_2]_2$. Science. 2004; 303:821–823. [PubMed: 14764874]

140. Ziolo RF, Giannelis EP, Weinstein BA, O'horo MP, Ganguly BN, Mehrotra V, Russell MW, Huffman DR. Matrix-Mediated Synthesis of Nanocrystalline γ-Fe_2O_3: A New Optically Transparent Magnetic Material. Science. 1992; 257:219–223. [PubMed: 17794752]
141. Rockenberger J, Scher EC, Alivisatos AP. A New Nonhydrolytic Single-Precursor Approach to Surfactant-Capped Nanocrystals of Transition Metal Oxides. J Am Chem Soc. 1999; 121:11595–11596.
142. Castro C, Millan A, Palacio F. Nickel Oxide Magnetic Nanocomposites in an Imine Polymer Matrix. J Mater Chem. 2000; 10:1945–1947.
143. Shevchenko EV, Talapin DV, Rogach AL, Kornowski A, Haase M, Weller H. Colloidal Synthesis and Self-Assembly of CoPt Nanocrystals. J Am Chem Soc. 2002; 124:11480–11485. [PubMed: 12236762]
144. Seo WS, Lee JH, Sun X, Suzuki Y, Mann D, Liu Z, Terashima M, Yang PC, McConnell MV, Nishimura DG, Dai H. FeCo/Graphitic-Shell Nanocrystals as Advanced Magnetic-Resonance-Imaging and Near-Infrared Agents. Nat Mater. 2006; 5:971–976. [PubMed: 17115025]
145. Sun S. Monodisperse FePt Nanoparticles and Ferromagnetic FePt Nanocrystal Superlattices. Science. 2000; 287:1989–1992. [PubMed: 10720318]
146. Zeng H, Rice PM, Wang SX, Sun S. Shape-Controlled Synthesis and Shape-Induced Texture of $MnFe_2O_4$ Nanoparticles. J Am Chem Soc. 2004; 126:11458–11459. [PubMed: 15366890]
147. Lee JH, Huh YM, Jun YW, Seo JW, Jang JT, Song HT, Kim S, Cho EJ, Yoon HG, Suh JS, Cheon J. Artificially Engineered Magnetic Nanoparticles for Ultra-Sensitive Molecular Imaging. Nat Med. 2007; 13:95–99. [PubMed: 17187073]
148. Jang JT, Nah H, Lee JH, Moon SH, Kim MG, Cheon J. Critical Enhancements of MRI Contrast and Hyperthermic Effects by Dopant-Controlled Magnetic Nanoparticles. Angew Chem Int Ed Engl. 2009; 48:1234–1238. [PubMed: 19137514]
149. Jain TK, Reddy MK, Morales MA, Leslie-Pelecky DL, Labhasetwar V. Biodistribution, Clearance, and Biocompatibility of Iron Oxide Magnetic Nanoparticles in Rats. Mol Pharm. 2008; 5:316–327. [PubMed: 18217714]
150. Weissleder R, Stark DD, Engelstad BL, Bacon BR, Compton CC, White DL, Jacobs P, Lewis J. Superparamagnetic Iron Oxide: Pharmacokinetics and Toxicity. Am J Roentgenol. 1989; 152:167–173. [PubMed: 2783272]
151. Reimer P, Rummeny EJ, Daldrup HE, Balzer T, Tombach B, Berns T, Peters PE. Clinical Results with Resovist: A Phase 2 Clinical Trial. Radiology. 1995; 195:489–496. [PubMed: 7724772]
152. Jung CW, Jacobs P. Physical and Chemical Properties of Superparamagnetic Iron Oxide MR Contrast Agents: Ferumoxides, Ferumoxtran, Ferumoxsil. Magn Reson Imaging. 1995; 13:661–674. [PubMed: 8569441]
153. Bullivant JP, Zhao S, Willenberg BJ, Kozissnik B, Batich CD, Dobson J. Materials Characterization of Feraheme/Ferumoxytol and Preliminary Evaluation of Its Potential for Magnetic Fluid Hyperthermia. Int J Mol Sci. 2013; 14:17501–17510. [PubMed: 24065092]
154. Häfeli, U. Scientific and Clinical Applications of Magnetic Carriers. Springer; 1997.
155. Weissleder R, Nahrendorf M, Pittet MJ. Imaging Macrophages with Nanoparticles. Nat Mater. 2014; 13:125–138. [PubMed: 24452356]
156. Carter, CB., Norton, G. Ceramic Materials: Science and Engineering. Springer; 2013.
157. Varadan, VK., Chen, LF., Xie, J. Nanomedicine: Design and Applications of Magnetic Nanomaterials, Nanosensors and Nanosystems. Wiley; 2008.
158. Lu AH, Salabas EL, Schuth F. Magnetic Nanoparticles: Synthesis, Protection, Functionalization, and Application. Angew Chem Int Ed Engl. 2007; 46:1222–1244. [PubMed: 17278160]
159. Laurent S, Forge D, Port M, Roch A, Robic C, Vander Elst L, Muller RN. Magnetic Iron Oxide Nanoparticles: Synthesis, Stabilization, Vectorization, Physicochemical Characterizations, and Biological Applications. Chem Rev. 2008; 108:2064–2110. [PubMed: 18543879]
160. Josephson L, Tung CH, Moore A, Weissleder R. High-Efficiency Intracellular Magnetic Labeling with Novel Superparamagnetic-Tat Peptide Conjugates. Bioconjug Chem. 1999; 10:186–191. [PubMed: 10077466]
161. Kim DK, Mikhaylova M, Zhang Y, Muhammed M. Protective Coating of Superparamagnetic Iron Oxide Nanoparticles. Chem Mater. 2003; 15:1617–1627.

162. Lutz JF, Stiller S, Hoth A, Kaufner L, Pison U, Cartier R. One-Pot Synthesis of PEGylated Ultrasmall Iron-Oxide Nanoparticles and Their In Vivo Evaluation as Magnetic Resonance Imaging Contrast Agents. Biomacromolecules. 2006; 7:3132–3138. [PubMed: 17096542]
163. Li Z, Tan B, Allix M, Cooper AI, Rosseinsky MJ. Direct Coprecipitation Route to Monodisperse Dual-Functionalized Magnetic Iron Oxide Nanocrystals without Size Selection. Small. 2008; 4:231–239. [PubMed: 18213671]
164. Pardoe H, Chua-anusorn W, Pierre TGS, Dobson J. Detection Limits for Ferrimagnetic Particle Concentrations Using Magnetic Resonance Imaging Based Proton Transverse Relaxation Rate Measurements. Phys Med Biol. 2003; 48:N89–N95. [PubMed: 12699196]
165. Cornell, RM., Schwertmann, U. The Iron Oxides: Structure, Properties, Reactions, Occurrences and Uses. Wiley; 2006.
166. Tartaj P, Morales MP, Veintemillas-Verdaguer S, Gonzalez-Carreño T, Serna CJ. Chapter 5 synthesis, properties and biomedical applications of magnetic nanoparticles. Handb Magn Mater. 2006; 16:403–482.
167. Massart R, C V. Effect of Some Parameters on the Formation of Colloidal Magnetite in Alkaline-Medium-Yield and Particle-Size Control. J Chim Phys Phys-Chim Biol. 1987; 84:967.
168. Jolivet JP, Froidefond C, Pottier A, Chanéac C, Cassaignon S, Tronc E, Euzen P. Size Tailoring of Oxide Nanoparticles by Precipitation in Aqueous Medium. A Semi-Quantitative Modelling. J Mater Chem. 2004; 14:3281.
169. Babes L, Denizot B, Tanguy G, Le Jeune JJ, Jallet P. Synthesis of Iron Oxide Nanoparticles Used as MRI Contrast Agents: A Parametric Study. J Colloid Interface Sci. 1999; 212:474–482. [PubMed: 10092379]
170. Gribanov NM, Bibik EE, Buzunov OV, Naumov VN. Physico-Chemical Regularities of Obtaining Highly Dispersed Magnetite by the Method of Chemical Condensation. J Magn Magn Mater. 1990; 85:7–10.
171. Tronc E, Belleville P, Jolivet JP, Livage J. Transformation of Ferric Hydroxide into Spinel by Iron(II) Adsorption. Langmuir. 1992; 8:313–319.
172. Shen T, Weissleder R, Papisov M, Bogdanov A, Brady TJ. Monocrystalline Iron Oxide Nanocompounds (MION): Physicochemical Properties. Magn Reson Med. 1993; 29:599–604. [PubMed: 8505895]
173. Constantinides CD, Rogers J, Herzka DA, Boada FE, Bolar D, Kraitchman D, Gillen J, Bottomley PA. Superparamagnetic Iron Oxide MION as a Contrast Agent for Sodium MRI in Myocardial Infarction. Magn Reson Med. 2001; 46:1164–1168. [PubMed: 11746583]
174. Weissig V, Pettinger TK, Murdock N. Nanopharmaceuticals (Part 1): Products on the Market. Int J Nanomedicine. 2014; 9:4357–4373. [PubMed: 25258527]
175. Ferguson RM, Khandhar AP, Krishnan KM. Tracer Design for Magnetic Particle Imaging. J Appl Phys. 2012; 111:7B318.
176. Perez JM, Josephson L, O'Loughlin T, Hogemann D, Weissleder R. Magnetic Relaxation Switches Capable of Sensing Molecular Interactions. Nat Biotechnol. 2002; 20:816–820. [PubMed: 12134166]
177. Josephson L, Kircher MF, Mahmood U, Tang Y, Weissleder R. Near-Infrared Fluorescent Nanoparticles as Combined MR/Optical Imaging Probes. Bioconjugate Chem. 2002; 13:554–560.
178. Perez JM, O'Loughin T, Simeone FJ, Weissleder R, Josephson L. DNA-Based Magnetic Nanoparticle Assembly Acts as a Magnetic Relaxation Nanoswitch Allowing Screening of DNA-Cleaving Agents. J Am Chem Soc. 2002; 124:2856–2857. [PubMed: 11902860]
179. Perez JM, Simeone FJ, Saeki Y, Josephson L, Weissleder R. Viral-Induced Self-Assembly of Magnetic Nanoparticles Allows the Detection of Viral Particles in Biological Media. J Am Chem Soc. 2003; 125:10192–10193. [PubMed: 12926940]
180. Perez JM, Simeone FJ, Tsourkas A, Josephson L, Weissleder R. Peroxidase Substrate Nanosensors for MR Imaging. Nano Lett. 2004; 4:119–122.
181. Perez JM, Josephson L, Weissleder R. Use of Magnetic Nanoparticles as Nanosensors to Probe for Molecular Interactions. ChemBioChem. 2004; 5:261–264. [PubMed: 14997516]

182. Tassa C, Shaw SY, Weissleder R. Dextran-Coated Iron Oxide Nanoparticles: A Versatile Platform for Targeted Molecular Imaging, Molecular Diagnostics, and Therapy. Acc Chem Res. 2011; 44:842–852. [PubMed: 21661727]
183. Colombo M, Carregal-Romero S, Casula MF, Gutierrez L, Morales MP, Bohm IB, Heverhagen JT, Prosperi D, Parak WJ. Biological Applications of Magnetic Nanoparticles. Chem Soc Rev. 2012; 41:4306–4334. [PubMed: 22481569]
184. Hyeon T, Lee SS, Park J, Chung Y, Na HB. Synthesis of Highly Crystalline and Monodisperse Maghemite Nanocrystallites without a Size-Selection Process. J Am Chem Soc. 2001; 123:12798–12801. [PubMed: 11749537]
185. Sun S, Zeng H, Robinson DB, Raoux S, Rice PM, Wang SX, Li G. Monodisperse MFe_2O_4 (M = Fe, Co, Mn) Nanoparticles. J Am Chem Soc. 2004; 126:273–279. [PubMed: 14709092]
186. Cheon J, Kang NJ, Lee SM, Lee JH, Yoon JH, Oh SJ. Shape Evolution of Single-Crystalline Iron Oxide Nanocrystals. J Am Chem Soc. 2004; 126:1950–1951. [PubMed: 14971924]
187. Jun YW, Choi JS, Cheon J. Shape Control of Semiconductor and Metal Oxide Nanocrystals through Nonhydrolytic Colloidal Routes. Angew Chem Int Ed Engl. 2006; 45:3414–3439. [PubMed: 16642516]
188. Sun S, Zeng H. Size-Controlled Synthesis of Magnetite Nanoparticles. J Am Chem Soc. 2002; 124:8204–8205. [PubMed: 12105897]
189. Sugimoto, T. Monodispersed Particles. Elsevier Science; 2001.
190. Jun YW, Lee JH, Cheon J. Chemical Design of Nanoparticle Probes for High-Performance Magnetic Resonance Imaging. Angew Chem Int Ed Engl. 2008; 47:5122–5135. [PubMed: 18574805]
191. Giersig M, Hilgendorff M. Magnetic Nanoparticle Superstructures. Eur J Inorg Chem. 2005; 2005:3571–3583.
192. Lee N, Hyeon T. Designed Synthesis of Uniformly Sized Iron Oxide Nanoparticles for Efficient Magnetic Resonance Imaging Contrast Agents. Chem Soc Rev. 2012; 41:2575–2589. [PubMed: 22138852]
193. Wonterghem, van J., Mørup, S., Charles, SW., Wells, S., Villadsen, J. Formation of a Metallic Glass by Thermal Decomposition of $Fe(CO)_5$. Phys Rev Lett. 1985; 55:410–413. [PubMed: 10032343]
194. Wilcoxon JP, Provencio PP. Use of Surfactant Micelles to Control the Structural Phase of Nanosize Iron Clusters. J Phys Chem B. 1999; 103:9809–9812.
195. Rudge SR, Kurtz TL, Vessely CR, Catterall LG, Williamson DL. Preparation, Characterization, and Performance of Magnetic Iron–Carbon Composite Microparticles for Chemotherapy. Biomaterials. 2000; 21:1411–1420. [PubMed: 10872770]
196. Cabot A, Puntes VF, Shevchenko E, Yin Y, Balcells L, Marcus MA, Hughes SM, Alivisatos AP. Vacancy Coalescence During Oxidation of Iron Nanoparticles. J Am Chem Soc. 2007; 129:10358–10360. [PubMed: 17676738]
197. Peng S, Wang C, Xie J, Sun S. Synthesis and Stabilization of Monodisperse Fe Nanoparticles. J Am Chem Soc. 2006; 128:10676–10677. [PubMed: 16910651]
198. Ban Z, Barnakov YA, Li F, Golub VO, O'Connor CJ. The Synthesis of Core–Shell Iron@Gold Nanoparticles and Their Characterization. J Mater Chem. 2005; 15:4660–4662.
199. Lu Z, Prouty MD, Guo Z, Golub VO, Kumar CS, Lvov YM. Magnetic Switch of Permeability for Polyelectrolyte Microcapsules Embedded with Co@Au Nanoparticles. Langmuir. 2005; 21:2042–2050. [PubMed: 15723509]
200. Wilson JL. Synthesis and Magnetic Properties of Polymer Nanocomposites with Embedded Iron Nanoparticles. J Appl Phys. 2004; 95:1439.
201. Tang NJ, Chen W, Zhong W, Jiang HY, Huang SL, Du YW. Highly Stable Carbon-Coated Fe/SiO_2 Composites: Synthesis, Structure and Magnetic Properties. Carbon. 2006; 44:423–427.
202. Dahal N, Chikan V. Phase-Controlled Synthesis of Iron Silicide (Fe_3Si and $FeSi_2$) Nanoparticles in Solution. Chem Mater. 2010; 22:2892–2897.
203. Shultz MD, Calvin S, Gonzalez-Jimenez F, Mujica V, Alleluia BC, Carpenter EE. Gold-Coated Cementite Nanoparticles: An Oxidation-Resistant Alternative to α-Iron. Chem Mater. 2009; 21:5594–5600.

204. Jing Y, He SH, Wang JP. Fe_3Si Nanoparticles for Alternating Magnetic Field Heating. J Nanopart Res. 2013; 15:1–8.
205. Amendola V, Riello P, Meneghetti M. Magnetic Nanoparticles of Iron Carbide, Iron Oxide, Iron@Iron Oxide, and Metal Iron Synthesized by Laser Ablation in Organic Solvents. J Phys Chem C. 2011; 115:5140–5146.
206. Wrobel RJ, Hełminiak A, Arabczyk W, Narkiewicz U. Studies on the Kinetics of Carbon Deposit Formation on Nanocrystalline Iron Stabilized with Structural Promoters. J Phys Chem C. 2014; 118:15434–15439.
207. Sharma M, Mantri S, Bahadur D. Study of Carbon Encapsulated Iron Oxide/Iron Carbide Nanocomposite for Hyperthermia. J Magn Magn Mater. 2012; 324:3975–3980.
208. Sun S. Recent Advances in Chemical Synthesis, Self-Assembly, and Applications of FePt Nanoparticles. Adv Mater. 2006; 18:393–403.
209. Park JI, Cheon J. Synthesis of “Solid Solution” and “Core-Shell” Type Cobalt-Platinum Magnetic Nanoparticles via Transmetalation Reactions. J Am Chem Soc. 2001; 123:5743–5746. [PubMed: 11403607]
210. Cullity, BD., Graham, CD. Introduction to Magnetic Materials. Wiley; 2011.
211. Ristau RA, Barmak K, Lewis LH, Coffey KR, Howard JK. On the Relationship of High Coercivity and $L1_0$ Ordered Phase in CoPt and FePt Thin Films. J Appl Phys. 1999; 86:4527.
212. Stappert S, Rellinghaus B, Acet M, Wassermann EF. Gas-Phase Preparation of $L1_0$ Ordered FePt Nanoparticles. J Cryst Growth. 2003; 252:440–450.
213. Sun S, Fullerton EE, Weller D, Murray CB. Compositionally Controlled FePt Nanoparticle Materials. IEEE Trans Magn. 2001; 37:1239–1243.
214. Howard LE, Nguyen HL, Giblin SR, Tanner BK, Terry I, Hughes AK, Evans JS. A Synthetic Route to Size-Controlled FCC and FCT FePt Nanoparticles. J Am Chem Soc. 2005; 127:10140–10141. [PubMed: 16028904]
215. Momose S, Kodama H, Uzumaki T, Tanaka A. Fine Tuning of the Sizes of FePt Nanoparticles. Jpn J Appl Phys. 2005; 44:1147–1149.
216. Chen M, Liu JP, Sun S. One-Step Synthesis of Fept Nanoparticles with Tunable Size. J Am Chem Soc. 2004; 126:8394–8395. [PubMed: 15237993]
217. Lee JH, Jang JT, Choi JS, Moon SH, Noh SH, Kim JW, Kim JG, Kim IS, Park KI, Cheon J. Exchange-Coupled Magnetic Nanoparticles for Efficient Heat Induction. Nat Nanotechnol. 2011; 6:418–422. [PubMed: 21706024]
218. Patterson A. The Scherrer Formula for X-Ray Particle Size Determination. Phys Rev. 1939; 56:978–982.
219. Hansen MF, Mørup S. Estimation of Blocking Temperatures From ZFC/FC Curves. J Magn Magn Mater. 1999; 203:214–216.
220. Joffe I, Heubregbr R. Hysteresis Properties of Distributions of Cubic Single-Domain Ferromagnetic Particles. Philos Mag. 1974; 29:1051–1059.
221. Stoner EC, Wohlfarth EP. A Mechanism of Magnetic Hysteresis in Heterogeneous Alloys. Phil Trans R Soc Lond A. 1948; 240:599–642.
222. Derjaguin B, Landau LD. Theory of the Stability of Strongly Charged Lyophobic Sols and of the Adhesion of Strongly Changed Particles in Solution of Electrolytes. Acta Physicochim URSS. 1941; 14:633–662.
223. Verwey, EJW., Overbeek, JTG. Theory of the Stability of Lyophobic Colloids (Dover Books on Chemistry). Dover Publications; 1999.
224. Vincent B, Edwards J, Emmett S, Jones A. Depletion Flocculation in Dispersions of Sterically-Stabilised Particles (“Soft Spheres”). Colloids Surf. 1986; 18:261–281.
225. Veiseh O, Gunn JW, Zhang M. Design and Fabrication of Magnetic Nanoparticles for Targeted Drug Delivery and Imaging. Adv Drug Deliv Rev. 2010; 62:284–304. [PubMed: 19909778]
226. Ling D, Hyeon T. Chemical Design of Biocompatible Iron Oxide Nanoparticles for Medical Applications. Small. 2013; 9:1450–1466. [PubMed: 23233377]
227. Nel A, Xia T, Mädler L, Li N. Toxic Potential of Materials at the Nanolevel. Science. 2006; 311:622–627. [PubMed: 16456071]

228. Blackman ML, Royzen M, Fox JM. Tetrazine Ligation: Fast Bioconjugation Based on Inverse-Electron-Demand Diels-Alder Reactivity. J Am Chem Soc. 2008; 130:13518–13519. [PubMed: 18798613]

229. Mocan T, Clichici S, Agoşton-Coldea L, Mocan L, Şimon Ş, Ilie I, Biriş A, Mureşan A. Implications of Oxidative Stress Mechanisms in Toxicity of Nanoparticles (Review). Acta Physiologica Hungarica. 2010; 97:247–255. [PubMed: 20843763]

230. Salvati A, Pitek AS, Monopoli MP, Prapainop K, Bombelli FB, Hristov DR, Kelly PM, Aberg C, Mahon E, Dawson KA. Transferrin-Functionalized Nanoparticles Lose Their Targeting Capabilities when a Biomolecule Corona Adsorbs on the Surface. Nat Nanotechnol. 2013; 8:137–143. [PubMed: 23334168]

231. Nel AE, Madler L, Velegol D, Xia T, Hoek EM, Somasundaran P, Klaessig F, Castranova V, Thompson M. Understanding Biophysicochemical Interactions at the Nano-Bio Interface. Nat Mater. 2009; 8:543–557. [PubMed: 19525947]

232. Hadley MJ, Wright AJ, Rowson NA, Grover LM. Acicular Nanoparticles Formed through Coprecipitation of Iron Salts in the Presence of Bovine Serum Albumin. J Mater Chem. 2011; 21:13769.

233. Ma HL, Qi XR, Maitani Y, Nagai T. Preparation and Characterization of Superparamagnetic Iron Oxide Nanoparticles Stabilized by Alginate. Int J Pharm. 2007; 333:177–186. [PubMed: 17074454]

234. Javid A, Ahmadian S, Saboury AA, Kalantar SM, Rezaei-Zarchi S. Chitosan-Coated Superparamagnetic Iron Oxide Nanoparticles for Doxorubicin Delivery: Synthesis and Anticancer Effect Against Human Ovarian Cancer Cells. Chem Biol Drug Des. 2013; 82:296–306. [PubMed: 23594157]

235. Xu C, Xu K, Gu H, Zheng R, Liu H, Zhang X, Guo Z, Xu B. Dopamine as a Robust Anchor to Immobilize Functional Molecules on the Iron Oxide Shell of Magnetic Nanoparticles. J Am Chem Soc. 2004; 126:9938–9939. [PubMed: 15303865]

236. Wei H, Insin N, Lee J, Han HS, Cordero JM, Liu W, Bawendi MG. Compact Zwitterion-Coated Iron Oxide Nanoparticles for Biological Applications. Nano Lett. 2012; 12:22–25. [PubMed: 22185195]

237. Liu Y, Chen T, Wu C, Qiu L, Hu R, Li J, Cansiz S, Zhang L, Cui C, Zhu G, You M, Zhang T, Tan W. Facile Surface Functionalization of Hydrophobic Magnetic Nanoparticles. J Am Chem Soc. 2014; 136:12552–12555. [PubMed: 25140614]

238. Taupitz MW, W S, Schnorr J, Kravec I, Pilgrimm H, Bergmann-Fritsch H, Hamm B. Phase I Clinical Evaluation of Citrate-Coated Monocrystalline Very Small Superparamagnetic Iron Oxide Particles as a New Contrast Medium for Magnetic Resonance Imaging. Invest Radiol. 2004; 39:394–405. [PubMed: 15194910]

239. Jun YW, Huh YM, Choi JS, Lee JH, Song HT, Kim S, Yoon S, Kim KS, Shin JS, Suh JS, Cheon J. Nanoscale Size Effect of Magnetic Nanocrystals and Their Utilization for Cancer Diagnosis via Magnetic Resonance Imaging. J Am Chem Soc. 2005; 127:5732–5733. [PubMed: 15839639]

240. Huh YM, Jun YW, Song HT, Kim S, Choi JS, Lee JH, Yoon S, Kim KS, Shin JS, Suh JS, Cheon J. In Vivo Magnetic Resonance Detection of Cancer by Using Multifunctional Magnetic Nanocrystals. J Am Chem Soc. 2005; 127:12387–12391. [PubMed: 16131220]

241. Mahato, RI. Biomaterials for Delivery and Targeting of Proteins and Nucleic Acids. CRC Press Inc; 2004.

242. Otsuka H, Nagasaki Y, Kataoka K. PEGylated Nanoparticles for Biological and Pharmaceutical Applications. Adv Drug Deliv Rev. 2003; 55:403–419. [PubMed: 12628324]

243. Karakoti AS, Das S, Thevuthasan S, Seal S. PEGylated Inorganic Nanoparticles. Angew Chem Int Ed Engl. 2011; 50:1980–1994. [PubMed: 21275011]

244. Xie J, Xu C, Kohler N, Hou Y, Sun S. Controlled PEGylation of Monodisperse Fe_3O_4 Nanoparticles for Reduced Non-Specific Uptake by Macrophage Cells. Adv Mater. 2007; 19:3163–3166.

245. Amstad E, Gehring AU, Fischer H, Nagaiyanallur VV, Hähner G, Textor M, Reimhult E. Influence of Electronegative Substituents on the Binding Affinity of Catechol-Derived Anchors to Fe_3O_4 Nanoparticles. J Phys Chem C. 2011; 115:683–691.

246. Kim SW, Kim S, Tracy JB, Jasanoff A, Bawendi MG. Phosphine Oxide Polymer for Water-Soluble Nanoparticles. J Am Chem Soc. 2005; 127:4556–4557. [PubMed: 15796504]

247. Na HB, Lee IS, Seo H, Park YI, Lee JH, Kim SW, Hyeon T. Versatile PEG-Derivatized Phosphine Oxide Ligands for Water-Dispersible Metal Oxide Nanocrystals. Chem Commun. 2007:5167–5169.

248. Kohler N, Fryxell GE, Zhang M. A Bifunctional Poly(Ethylene Glycol) Silane Immobilized on Metallic Oxide-Based Nanoparticles for Conjugation with Cell Targeting Agents. J Am Chem Soc. 2004; 126:7206–7211. [PubMed: 15186157]

249. Na HB, Palui G, Rosenberg JT, Ji X, Grant SC, Mattoussi H. Multidentate Catechol-Based Polyethylene Glycol Oligomers Provide Enhanced Stability and Biocompatibility to Iron Oxide Nanoparticles. ACS Nano. 2012; 6:389–399. [PubMed: 22176202]

250. Juliano, RL. Drug delivery systems: characteristics and biomedical applications. Oxford University Press; 1980.

251. Sery TW, Hehre EJ. Degradation of Dextrans by Enzymes of Intestinal Bacteria. J Bacteriol. 1956; 71:373–380. [PubMed: 13306712]

252. Creixell M, Herrera AP, Latorre-Esteves M, Ayala V, Torres-Lugo M, Rinaldi C. The Effect of Grafting Method on the Colloidal Stability and In Vitro Cytotoxicity of Carboxymethyl Dextran Coated Magnetic Nanoparticles. J Mater Chem. 2010; 20:8539.

253. Moffitt EA. Blood Substitutes. Can Anaesth Soc J. 1975; 22:12–19. [PubMed: 1109702]

254. Dong A, Ye X, Chen J, Kang Y, Gordon T, Kikkawa JM, Murray CB. A Generalized Ligand-Exchange Strategy Enabling Sequential Surface Functionalization of Colloidal Nanocrystals. J Am Chem Soc. 2011; 133:998–1006. [PubMed: 21175183]

255. Liong M, Shao H, Haun JB, Lee H, Weissleder R. Carboxymethylated Polyvinyl Alcohol Stabilizes Doped Ferrofluids for Biological Applications. Adv Mater. 2010; 22:5168–5172. [PubMed: 20859943]

256. Kircheis R, Wightman L, Wagner E. Design and Gene Delivery Activity of Modified Polyethylenimines. Adv Drug Deliv Rev. 2001; 53:341–358. [PubMed: 11744176]

257. Boussif O, Lezoualc'h F, Zanta MA, Mergny MD, Scherman D, Demeneix B, Behr JP. A Versatile Vector for Gene and Oligonucleotide Transfer into Cells in Culture and In Vivo: Polyethylenimine. Proc Natl Acad Sci USA. 1995; 92:7297–7301. [PubMed: 7638184]

258. Kievit FM, Veiseh O, Bhattarai N, Fang C, Gunn JW, Lee D, Ellenbogen RG, Olson JM, Zhang M. PEI-PEG-Chitosan Copolymer Coated Iron Oxide Nanoparticles for Safe Gene Delivery: Synthesis, Complexation, and Transfection. Adv Funct Mater. 2009; 19:2244–2251. [PubMed: 20160995]

259. Duan H, Kuang M, Wang X, Wang YA, Mao H, Nie S. Reexamining the Effects of Particle Size and Surface Chemistry on the Magnetic Properties of Iron Oxide Nanocrystals: New Insights into Spin Disorder and Proton Relaxivity. J Phys Chem C. 2008; 112:8127–8131.

260. Lee N, Kim H, Choi SH, Park M, Kim D, Kim HC, Choi Y, Lin S, Kim BH, Jung HS, Kim H, Park KS, Moon WK, Hyeon T. Magnetosome-Like Ferrimagnetic Iron Oxide Nanocubes for Highly Sensitive MRI of Single Cells and Transplanted Pancreatic Islets. Proc Natl Acad Sci U S A. 2011; 108:2662–2667. [PubMed: 21282616]

261. Robinson DB, Persson HH, Zeng H, Li G, Pourmand N, Sun S, Wang SX. DNA-Functionalized MFe_2O_4 (M = Fe, Co, or Mn) Nanoparticles and Their Hybridization to DNA-Functionalized Surfaces. Langmuir. 2005; 21:3096–3103. [PubMed: 15779990]

262. Nasongkla N, Bey E, Ren J, Ai H, Khemtong C, Guthi JS, Chin SF, Sherry AD, Boothman DA, Gao J. Multifunctional Polymeric Micelles as Cancer-Targeted, MRI-Ultrasensitive Drug Delivery Systems. Nano Lett. 2006; 6:2427–2430. [PubMed: 17090068]

263. Yu WW, Chang E, Sayes CM, Drezek R, Colvin VL. Aqueous Dispersion of Monodisperse Magnetic Iron Oxide Nanocrystals through Phase Transfer. Nanotechnology. 2006; 17:4483–4487.

264. Kim BS, Qiu JM, Wang JP, Taton TA. Magnetomicelles: Composite Nanostructures from Magnetic Nanoparticles and Cross-Linked Amphiphilic Block Copolymers. Nano Lett. 2005; 5:1987–1991. [PubMed: 16218723]

265. Tanimoto A, Kuribayashi S. Application of Superparamagnetic Iron Oxide to Imaging of Hepatocellular Carcinoma. Eur J Radiol. 2006; 58:200–216. [PubMed: 16414230]
266. Gupta AK, Wells S. Surface-Modified Superparamagnetic Nanoparticles for Drug Delivery: Preparation, Characterization, and Cytotoxicity Studies. IEEE Trans Nanobioscience. 2004; 3:66–73. [PubMed: 15382647]
267. Wang Y, Wong JF, Teng X, Lin XZ, Yang H. "Pulling" Nanoparticles into Water: Phase Transfer of Oleic Acid Stabilized Monodisperse Nanoparticles into Aqueous Solutions of α-Cyclodextrin. Nano Lett. 2003; 3:1555–1559.
268. Muthiah M, Lee SJ, Moon M, Lee HJ, Bae WK, Chung IJ, Jeong YY, Park IK. Surface Tunable Polymersomes Loaded with Magnetic Contrast Agent and Drug for Image Guided Cancer Therapy. J Nanosci Nanotechnol. 2013; 13:1626–1630. [PubMed: 23755567]
269. Cheng J, Teply BA, Sherifi I, Sung J, Luther G, Gu FX, Levy-Nissenbaum E, Radovic-Moreno AF, Langer R, Farokhzad OC. Formulation of Functionalized PLGA-PEG Nanoparticles for In Vivo Targeted Drug Delivery. Biomaterials. 2007; 28:869–876. [PubMed: 17055572]
270. Li K, Ding D, Huo D, Pu KY, Thao NNP, Hu Y, Li Z, Liu B. Conjugated Polymer Based Nanoparticles as Dual-Modal Probes for Targeted In Vivo Fluorescence and Magnetic Resonance Imaging. Adv Funct Mater. 2012; 22:3107–3115.
271. Charoenmark L, Polpanich D, Thiramanas R, Tangboriboonrat P. Preparation of Superparamagnetic Polystyrene-Based Nanoparticles Functionalized by Acrylic Acid. Macromol Res. 2012; 20:590–596.
272. Verena H, Myriam L, Clemens Kilian W, Hubert S, Katharina L, Volker M. Synthesis and Biomedical Applications of Functionalized Fluorescent and Magnetic Dual Reporter Nanoparticles as Obtained in the Miniemulsion Process. J Phys Cond Matter. 2006; 18:S2581.
273. Ren J, Hong H, Ren T, Teng X. Preparation and Characterization of Magnetic PLA–PEG Composite Nanoparticles for Drug Targeting. React Funct Polym. 2006; 66:944–951.
274. Tan H, Xue JM, Shuter B, Li X, Wang J. Synthesis of PEOlated Fe_3O_4@SiO_2 Nanoparticles via Bioinspired Silification for Magnetic Resonance Imaging. Adv Funct Mater. 2010; 20:722–731.
275. Taboada E, Solanas R, Rodríguez E, Weissleder R, Roig A. Supercritical-Fluid-Assisted One-Pot Synthesis of Biocompatible Core(γ-Fe_2O_3)/Shell(SiO_2) Nanoparticles as High Relaxivity T_2-Contrast Agents for Magnetic Resonance Imaging. Adv Funct Mater. 2009; 19:2319–2324.
276. Taboada E, Gich M, Roig A. Nanospheres of Silica with an ε-Fe_2O_3 Single Crystal Nucleus. ACS Nano. 2009; 3:3377–3382. [PubMed: 19824669]
277. Xu X, Friedman G, Humfeld KD, Majetich SA, Asher SA. Synthesis and Utilization of Monodisperse Superparamagnetic Colloidal Particles for Magnetically Controllable Photonic Crystals. Chem Mater. 2002; 14:1249–1256.
278. Kaewsaneha C, Tangboriboonrat P, Polpanich D, Eissa M, Elaissari A. Anisotropic Janus Magnetic Polymeric Nanoparticles Prepared via Miniemulsion Polymerization. J Polym Sci Part A: Polym Chem. 2013; 51:4779–4785.
279. Neely LA, Audeh M, Phung NA, Min M, Suchocki A, Plourde D, Blanco M, Demas V, Skewis LR, Anagnostou T, Coleman JJ, Wellman P, Mylonakis E, Lowery TJ. T_2 Magnetic Resonance Enables Nanoparticle-Mediated Rapid Detection of Candidemia in Whole Blood. Sci Transl Med. 2013; 5:182ra54.
280. Ulman A. Formation and Structure of Self-Assembled Monolayers. Chem Rev. 1996; 96:1533–1554. [PubMed: 11848802]
281. Lu Y, Yin Y, Mayers BT, Xia Y. Modifying the Surface Properties of Superparamagnetic Iron Oxide Nanoparticles through a Sol−Gel Approach. Nano Lett. 2002; 2:183–186.
282. Tago T, Hatsuta T, Miyajima K, Kishida M, Tashiro S, Wakabayashi K. Novel Synthesis of Silica-Coated Ferrite Nanoparticles Prepared Using Water-in-Oil Microemulsion. J Am Ceram Soc. 2002; 85:2188–2194.
283. Graf C, Vossen DLJ, Imhof A, Alfons van B. A General Method to Coat Colloidal Particles with Silica. Langmuir. 2003; 19:6693–6700.
284. Stöber W, Fink A, Bohn E. Controlled Growth of Monodisperse Silica Spheres in the Micron Size Range. J Colloid Interface Sci. 1968; 26:62–69.
285. Hench LL, West JK. The Sol-Gel Process. Chem Rev. 1990; 90:33–72.

286. Yi DK, Lee SS, Papaefthymiou GC, Ying JY. Nanoparticle Architectures Templated by SiO_2/Fe_2O_3 Nanocomposites. Chem Mater. 2006; 18:614–619.

287. Choi JS, Lee JH, Shin TH, Song HT, Kim EY, Cheon J. Self-Confirming "AND" Logic Nanoparticles for Fault-Free MRI. J Am Chem Soc. 2010; 132:11015–11017. [PubMed: 20698661]

288. Yoo D, Jeong H, Preihs C, Choi JS, Shin TH, Sessler JL, Cheon J. Double-Effector Nanoparticles: A Synergistic Approach to Apoptotic Hyperthermia. Angew Chem Int Ed Engl. 2012; 51:12482–12485. [PubMed: 23139178]

289. Shin TH, Choi JS, Yun S, Kim IS, Song HT, Kim Y, Park KI, Cheon J. T_1 and T_2 Dual-Mode MRI Contrast Agent for Enhancing Accuracy by Engineered Nanomaterials. ACS Nano. 2014; 8:3393–3401. [PubMed: 24673493]

290. Misra, A. Challenges in Delivery of Therapeutic Genomics and Proteomics. Elsevier Science; 2010.

291. Trubetskoy VS, Torchilin VP, Kennel SJ, Huang L. Use of N-Terminal Modified Poly(L-Lysine)-Antibody Conjugate as a Carrier for Targeted Gene Delivery in Mouse Lung Endothelial Cells. Bioconjugate Chem. 1992; 3:323–327.

292. Haun JB, Devaraj NK, Hilderbrand SA, Lee H, Weissleder R. Bioorthogonal Chemistry Amplifies Nanoparticle Binding and Enhances the Sensitivity of Cell Detection. Nat Nanotechnol. 2010; 5:660–665. [PubMed: 20676091]

293. Hermanson, GT. Bioconjugate Techniques. Elsevier Science; 2013.

294. Högemann D, Josephson L, Weissleder R, Basilion JP. Improvement of MRI Probes to Allow Efficient Detection of Gene Expression. Bioconjugate Chem. 2000; 11:941–946.

295. Scarberry KE, Dickerson EB, McDonald JF, Zhang ZJ. Magnetic Nanoparticle-Peptide Conjugates for In Vitro and In Vivo Targeting and Extraction of Cancer Cells. J Am Chem Soc. 2008; 130:10258–10262. [PubMed: 18611005]

296. Liu CH, Sahoo SL, Tsao MH. Acridine Orange Coated Magnetic Nanoparticles for Nucleus Labeling and DNA Adsorption. Colloids Surf B Biointerfaces. 2014; 115:150–156. [PubMed: 24334267]

297. Long J, Jiao A, Wei B, Wu Z, Zhang Y, Xu X, Jin Z. A Novel Method for Pullulanase Immobilized onto Magnetic Chitosan/Fe_3O_4 Composite Nanoparticles by In Situ Preparation and Evaluation of the Enzyme Stability. J Mol Catal B: Enzym. 2014; 109:53–61.

298. Sletten EM, Bertozzi CR. Bioorthogonal Chemistry: Fishing for Selectivity in a Sea of Functionality. Angew Chem Int Ed Engl. 2009; 48:6974–6998. [PubMed: 19714693]

299. Sletten EM, Bertozzi CR. From Mechanism to Mouse: A Tale of Two Bioorthogonal Reactions. Acc Chem Res. 2011; 44:666–676. [PubMed: 21838330]

300. McKay CS, Finn MG. Click Chemistry in Complex Mixtures: Bioorthogonal Bioconjugation. Chem Biol. 2014; 21:1075–1101. [PubMed: 25237856]

301. Kolb HC, Finn MG, Sharpless KB. Click Chemistry: Diverse Chemical Function from a Few Good Reactions. Angew Chem Int Ed. 2001; 40:2004–2021.

302. Rostovtsev VV, Green LG, Fokin VV, Sharpless KB. A Stepwise Huisgen Cycloaddition Process: Copper(I)-Catalyzed Regioselective "Ligation" of Azides and Terminal Alkynes. Angew Chem Int Ed. 2002; 41:2596–2599.

303. Moses JE, Moorhouse AD. The Growing Applications of Click Chemistry. Chem Soc Rev. 2007; 36:1249–1262. [PubMed: 17619685]

304. Tornøe CW, Christensen C, Meldal M. Peptidotriazoles on Solid Phase: [1,2,3]-Triazoles by Regiospecific Copper(I)-Catalyzed 1,3-Dipolar Cycloadditions of Terminal Alkynes to Azides. J Org Chem. 2002; 67:3057–3064. [PubMed: 11975567]

305. Chan TR, Hilgraf R, Sharpless KB, Fokin VV. Polytriazoles as Copper(I)-Stabilizing Ligands in Catalysis. Org Lett. 2004; 6:2853–2855. [PubMed: 15330631]

306. Rodionov VO, Presolski SI, Gardinier S, Lim YH, Finn MG. Benzimidazole and Related Ligands for Cu-Catalyzed Azide-Alkyne Cycloaddition. J Am Chem Soc. 2007; 129:12696–12704. [PubMed: 17914816]

307. Baskin JM, Prescher JA, Laughlin ST, Agard NJ, Chang PV, Miller IA, Lo A, Codelli JA, Bertozzi CR. Copper-Free Click Chemistry for Dynamic In Vivo Imaging. Proc Natl Acad Sci U S A. 2007; 104:16793–16797. [PubMed: 17942682]

308. Jewett JC, Bertozzi CR. Cu-Free Click Cycloaddition Reactions in Chemical Biology. Chem Soc Rev. 2010; 39:1272. [PubMed: 20349533]

309. Saxon E. Cell Surface Engineering by a Modified Staudinger Reaction. Science. 2000; 287:2007–2010. [PubMed: 10720325]

310. Zhang H, Ma Y, Sun XL. Chemically-Selective Surface Glyco-Functionalization of Liposomes through Staudinger Ligation. Chem Commun. 2009:3032–3034.

311. de Araujo AD, Palomo JM, Cramer J, Kohn M, Schroder H, Wacker R, Niemeyer C, Alexandrov K, Waldmann H. Diels-Alder Ligation and Surface Immobilization of Proteins. Angew Chem Int Ed Engl. 2005; 45:296–301. [PubMed: 16315328]

312. Devaraj NK, Upadhyay R, Haun JB, Hilderbrand SA, Weissleder R. Fast and Sensitive Pretargeted Labeling of Cancer Cells through a Tetrazine/Trans-Cyclooctene Cycloaddition. Angew Chem Int Ed Engl. 2009; 48:7013–7016. [PubMed: 19697389]

313. Devaraj NK, Hilderbrand S, Upadhyay R, Mazitschek R, Weissleder R. Bioorthogonal Turn-On Probes for Imaging Small Molecules Inside Living Cells. Angew Chem Int Ed Engl. 2010; 49:2869–2872. [PubMed: 20306505]

314. Karver MR, Weissleder R, Hilderbrand SA. Synthesis and Evaluation of a Series of 1,2,4,5-Tetrazines for Bioorthogonal Conjugation. Bioconjug Chem. 2011; 22:2263–2270. [PubMed: 21950520]

315. Haun JB, Castro CM, Wang R, Peterson VM, Marinelli BS, Lee H, Weissleder R. Micro-NMR for Rapid Molecular Analysis of Human Tumor Samples. Sci Transl Med. 2011; 3:71ra16.

316. Haun JB, Devaraj NK, Marinelli BS, Lee H, Weissleder R. Probing Intracellular Biomarkers and Mediators of Cell Activation Using Nanosensors and Bioorthogonal Chemistry. ACS Nano. 2011; 5:3204–3213. [PubMed: 21351804]

317. Liong M, Tassa C, Shaw SY, Lee H, Weissleder R. Multiplexed Magnetic Labeling Amplification Using Oligonucleotide Hybridization. Adv Mater. 2011; 23:H254–H257. [PubMed: 21780311]

318. Vallee A, Humblot V, Pradier CM. Peptide Interactions with Metal and Oxide Surfaces. Acc Chem Res. 2010; 43:1297–1306. [PubMed: 20672797]

319. Hochuli E, Bannwarth W, Döbeli H, Gentz R, Stüber D. Genetic Approach to Facilitate Purification of Recombinant Proteins with a Novel Metal Chelate Adsorbent. Nat Biotechnol. 1988; 6:1321–1325.

320. Ueda EKM, Gout PW, Morganti L. Current and Prospective Applications of Metal Ion–Protein Binding. J Chromatogr A. 2003; 988:1–23. [PubMed: 12647817]

321. Xu C, Xu K, Gu H, Zhong X, Guo Z, Zheng R, Zhang X, Xu B. Nitrilotriacetic Acid-Modified Magnetic Nanoparticles as a General Agent to Bind Histidine-Tagged Proteins. J Am Chem Soc. 2004; 126:3392–3393. [PubMed: 15025444]

322. Kim JS, Valencia CA, Liu R, Lin W. Highly-Efficient Purification of Native Polyhistidine-Tagged Proteins by Multivalent NTA-Modified Magnetic Nanoparticles. Bioconjug Chem. 2007; 18:333–341. [PubMed: 17311440]

323. Durland RH, Eastman EM. Manufacturing and Quality Control of Plasmid-Based Gene Expression Systems. Adv Drug Deliv Rev. 1998; 30:33–48. [PubMed: 10837600]

324. Kim J, Piao Y, Lee N, Park YI, Lee IH, Lee JH, Paik SR, Hyeon T. Magnetic Nanocomposite Spheres Decorated with NiO Nanoparticles for a Magnetically Recyclable Protein Separation System. Adv Mater. 2010; 22:57–60. [PubMed: 20217697]

325. Lee IS, Lee N, Park J, Kim BH, Yi YW, Kim T, Kim TK, Lee IH, Paik SR, Hyeon T. Ni/NiO Core/Shell Nanoparticles for Selective Binding and Magnetic Separation of Histidine-Tagged Proteins. J Am Chem Soc. 2006; 128:10658–10659. [PubMed: 16910642]

326. Lodish, H., Berk, A., Kaiser, CA., Krieger, M., Bretscher, A., Ploegh, H., Amon, A., Scott, MP. Molecular Cell Biology. W H Freeman; 2012.

327. Sapsford KE, Algar WR, Berti L, Gemmill KB, Casey BJ, Oh E, Stewart MH, Medintz IL. Functionalizing Nanoparticles with Biological Molecules: Developing Chemistries that Facilitate Nanotechnology. Chem Rev. 2013; 113:1904–2074. [PubMed: 23432378]

328. Livnah O, Bayer EA, Wilchek M, Sussman JL. Three-Dimensional Structures of Avidin and the Avidin-Biotin Complex. Proc Natl Acad Sci U S A. 1993; 90:5076–5080. [PubMed: 8506353]

329. Green NM. Thermodynamics of the Binding of Biotin and Some Analogues by Avidin. Biochem J. 1966; 101:774–780. [PubMed: 16742458]

330. Tiefenauer LX, Kuehne G, Andres RY. Antibody-Magnetite Nanoparticles: In Vitro Characterization of a Potential Tumor-Specific Contrast Agent for Magnetic Resonance Imaging. Bioconjugate Chem. 1993; 4:347–352.

331. Guven B, Basaran-Akgul N, Temur E, Tamer U, Boyaci IH. SERS-Based Sandwich Immunoassay Using Antibody Coated Magnetic Nanoparticles for Escherichia Coli Enumeration. Analyst. 2011; 136:740–748. [PubMed: 21125089]

332. Artemov D. Molecular Magnetic Resonance Imaging with Targeted Contrast Agents. J Cell Biochem. 2003; 90:518–524. [PubMed: 14523986]

333. Miller BT, Collins TJ, Rogers ME, Kurosky A. Peptide Biotinylation with Amine-Reactive Esters: Differential Side Chain Reactivity. Peptides. 1997; 18:1585–1595. [PubMed: 9437720]

334. Wilchek M, Bayer EA, Livnah O. Essentials of Biorecognition: The Strept)avidin-Biotin System as a Model for Protein-Protein and Protein-Ligand Interaction. Immunol Lett. 2006; 103:27–32. [PubMed: 16325268]

335. Yao Z, Zhang M, Sakahara H, Nakamoto Y, Higashi T, Zhao S, Sato N, Arano Y, Konishi J. The Relationship of Glycosylation and Isoelectric Point with Tumor Accumulation of Avidin. J Nucl Med. 1999; 40:479–483. [PubMed: 10086714]

336. Chaiet L, Wolf FJ. The Properties of Streptavidin, a Biotin-Binding Protein Produced by Streptomycetes. Arch Biochem Biophys. 1964; 106:1–5. [PubMed: 14217155]

337. Nash MA, Yager P, Hoffman AS, Stayton PS. Mixed Stimuli-Responsive Magnetic and Gold Nanoparticle System for Rapid Purification, Enrichment, and Detection of Biomarkers. Bioconjug Chem. 2010; 21:2197–2204. [PubMed: 21070026]

338. Min C, Shao H, Liong M, Yoon TJ, Weissleder R, Lee H. Mechanism of Magnetic Relaxation Switching Sensing. ACS Nano. 2012; 6:6821–6828. [PubMed: 22762250]

339. Ilyas S, Ilyas M, van der Hoorn RA, Mathur S. Selective Conjugation of Proteins by Mining Active Proteomes through Click-Functionalized Magnetic Nanoparticles. ACS Nano. 2013; 7:9655–9663. [PubMed: 24143894]

340. Ranzoni A, Sabatte G, van Ijzendoorn LJ, Prins MW. One-Step Homogeneous Magnetic Nanoparticle Immunoassay for Biomarker Detection Directly in Blood Plasma. ACS Nano. 2012; 6:3134–3141. [PubMed: 22414272]

341. Haun JB, Yoon TJ, Lee H, Weissleder R. Magnetic Nanoparticle Biosensors. Wiley Interdiscip Rev Nanomed Nanobiotechnol. 2010; 2:291–304. [PubMed: 20336708]

342. Shao H, Yoon TJ, Liong M, Weissleder R, Lee H. Magnetic Nanoparticles for Biomedical NMR-Based Diagnostics. Beilstein J Nanotechnol. 2010; 1:142–154. [PubMed: 21977404]

343. Shao H, Min C, Issadore D, Liong M, Yoon TJ, Weissleder R, Lee H. Magnetic Nanoparticles and MicroNMR for Diagnostic Applications. Theranostics. 2012; 2:55–65. [PubMed: 22272219]

344. Lee H, Yoon TJ, Weissleder R. Ultrasensitive Detection of Bacteria Using Core-Shell Nanoparticles and an NMR-Filter System. Angew Chem Int Ed Engl. 2009; 48:5657–5660. [PubMed: 19554581]

345. Perez JM, O'Loughin T, Simeone FJ, Weissleder R, Josephson L. DNA-Based Magnetic Nanoparticle Assembly Acts as a Magnetic Relaxation Nanoswitch Allowing Screening of DNA-Cleaving Agents. J Am Chem Soc. 2002; 124:2856–2857. [PubMed: 11902860]

346. Beyda ND, Alam MJ, Garey KW. Comparison of the T2dx Instrument with T2Candida Assay and Automated Blood Culture in the Detection of Candida Species Using Seeded Blood Samples. Diagn Microbiol Infect Dis. 2013; 77:324–326. [PubMed: 24135411]

347. Ling Y, Vassiliou CC, Cima MJ. Magnetic Relaxation-Based Platform for Multiplexed Assays. Analyst. 2010; 135:2360–2364. [PubMed: 20625581]

348. Im H, Shao H, Park YI, Peterson VM, Castro CM, Weissleder R, Lee H. Label-Free Detection and Molecular Profiling of Exosomes with a Nano-Plasmonic Sensor. Nat Biotechnol. 2014; 32:490–495. [PubMed: 24752081]

349. Skewis LR, Lebedeva T, Papkov V, Thayer EC, Massefski W, Cuker A, Nagaswami C, Litvinov RI, Kowalska MA, Rauova L, Poncz M, Weisel JW, Lowery TJ, Cines DB. T_2 Magnetic Resonance: A Diagnostic Platform for Studying Integrated Hemostasis in Whole Blood. Clin Chem. 2014; 60:1174–1182. [PubMed: 24958814]

350. Dittmer WU, Evers TH, Hardeman WM, Huijnen W, Kamps R, de Kievit P, Neijzen JH, Nieuwenhuis JH, Sijbers MJ, Dekkers DW, Hefti MH, Martens MF. Rapid, High Sensitivity, Point-of-Care Test for Cardiac Troponin Based on Optomagnetic Biosensor. Clin Chim Acta. 2010; 411:868–873. [PubMed: 20211616]

351. Sun EY, Weissleder R, Josephson L. Continuous Analyte Sensing with Magnetic Nanoswitches. Small. 2006; 2:1144–1147. [PubMed: 17193579]

Biographies

Hakho Lee is Assistant Professor at Harvard Medical School, and Director of the Biomedical Engineering Program at the Center for Systems Biology, Massachusetts General Hospital (MGH). He received his Ph.D. in Physics from Harvard University, and completed his post-doctoral training at MGH. Dr. Lee has extensive experience in nanomaterials, biophysics, microfluidics, and electrical engineering. His research is multidisciplinary and focuses on developing novel biomedical sensors such as the world's smallest portable NMR device, integrated circuit (IC) chips for cancer cell detection, novel surface-plasmon-resonance chips for exosome profiling, and microfluidic devices for single cell analyses.

Tae-Hyun Shin received his B.S. degree in Chemistry from Yonsei University in 2010. He is currently a graduate student at Yonsei University. His research interest is in designing and constructing functionalized inorganic nanoparticles for molecular imaging.

Jinwoo Cheon is the Horace G. Underwood Professor at Yonsei University and the Director of the National Creative Research Initiative Center for Evolutionary Nanoparticles. He graduated from Yonsei University with a B.S. and received his Ph.D. from the University of Illinois at Urbana-Champaign. After his postdoctoral training at U.C. Berkeley and UCLA, he joined KAIST. In 2002, he moved to Yonsei University. He is a recipient of many awards, including the POSCO Prize, Inchon Prize, and Song-gok Science Award. Currently, he is a senior editor of Accounts of Chemical Research and a fellow of the American Chemical Society and the Royal Society of Chemistry.

Ralph Weissleder is the Thrall Professor of Radiology and Professor of Systems Biology at Harvard Medical School (HMS), Director of the Center for Systems Biology at Massachusetts General Hospital (MGH), senior faculty in the HMS Department of Systems Biology, and Attending Clinician (Interventional Radiology) at MGH. He graduated from Heidelberg University in 1985, obtained his postdoctoral and residency training at MGH (1986-91) and has been on faculty at HMS since 1991. He has published over >750 publications in peer-reviewed journals, authored several textbooks and been named one of the “The World's Most Influential Scientific Minds” by Thomson Reuters in 2014. His work has been honored with numerous awards including the J. Taylor International Prize in Medicine, the Millenium Pharmaceuticals Innovator Award, the AUR Memorial Award, the ARRS President's Award, The Society for Molecular Imaging Lifetime Achievement Award, the Academy of Molecular Imaging 2006 Distinguished Basic Scientist Award among others. In 2009 he was elected member of the US National Institute of Medicine.

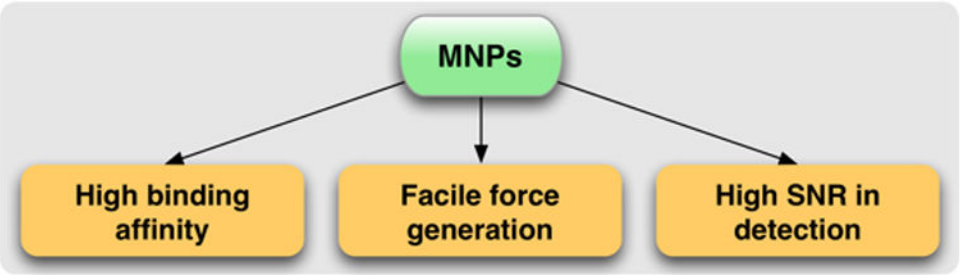

Figure 1. Unique advantages of magnetic nanoparticles (MNPs) in diagnostic applications

Affinity functionalized MNPs can efficiently bind to biological targets. The resultant magnetically-labeled targets (cells, proteins, nucleic acids) can be mechanically manipulated by applying external magnetic fields (magnetic actuation), or detected by using magnetometers (magnetic sensing). These operations achieve high contrast against the biological background, and can be performed in native, *i.e.,* non-purified clinical specimens.

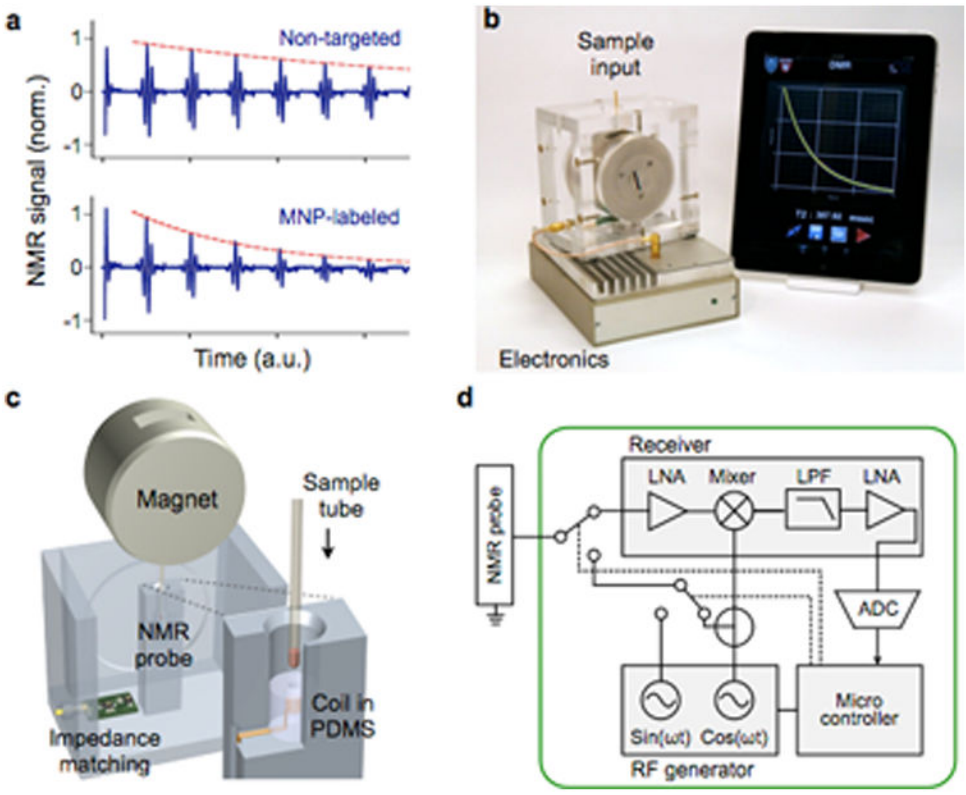

Figure 2. MicroNMR (μNMR) magnetometer

(a) Sensing mechanism. Samples containing MNP-labeled biological targets have higher transverse relaxation rate of ^{1}H NMR signal. **(b)** Prototype portable μNMR system, developed for clinical applications. This system has a capacity for automatic system tuning and features a user-friendly interface. **(c)** Magnet assembly and the NMR probe design. The microcoil is embedded in a polydimethylsiloxane (PDMS) substrate. The entire coil-bore is accessible by a sample, which maximizes the sample-filing factor. A thin-walled tube is used for sample-loading. **(d)** The NMR electronics is implemented using a field-programmable-gate-array (FPGA) chip that offers standalone operation and high programability. LNA, low-noise amplifier; LPF, low-pass filter; ADC, analog-to-digital converter. Reproduced with permission from Ref. 45. Copyright 2011 RSC Publishing.

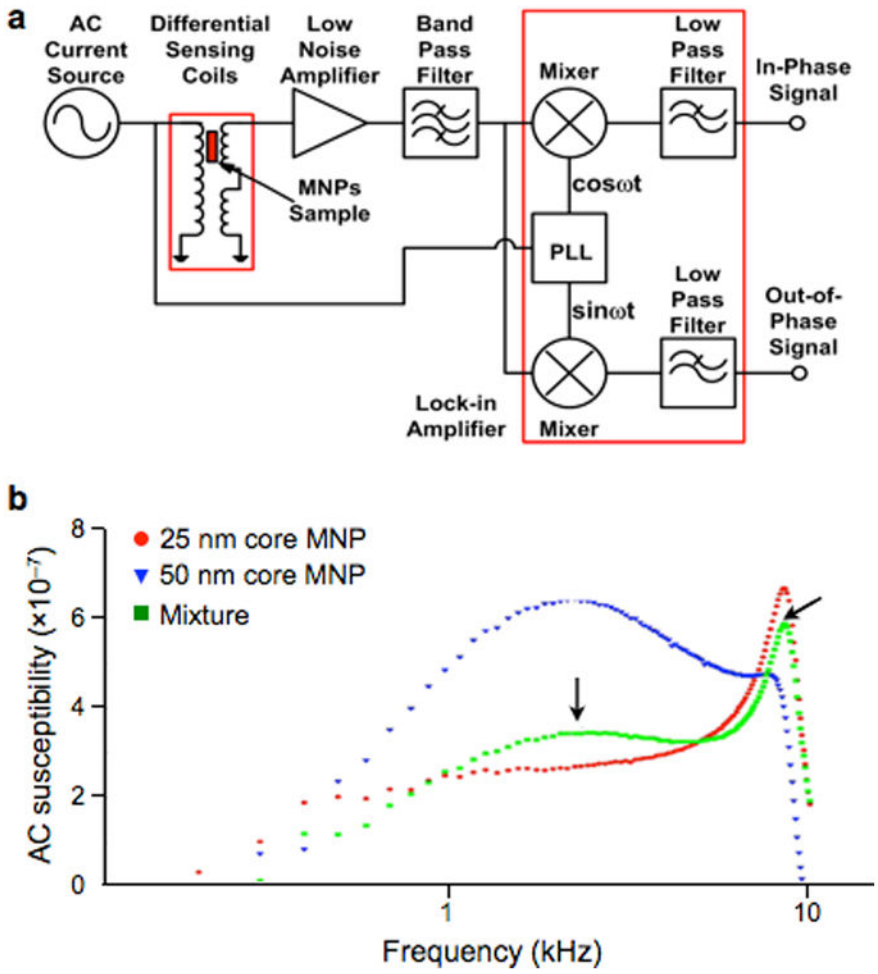

Figure 3. Magnetic susceptometer biosensor

(a) A quadrature detector was developed to sense alternating current (AC) magnetic susceptibility in solution. PLL, phase-locked loop. **(b)** The peak in the magnetic susceptibility shifts with particle size. The magnetic responses of two differently sized MNPs were measured (red, 25-nm core; blue, 50-nm core). This information was used to distinguish the composition in the mixture (green). Reprinted with permission from Ref. 56. Copyright 2011 IOP Publishing Ltd.

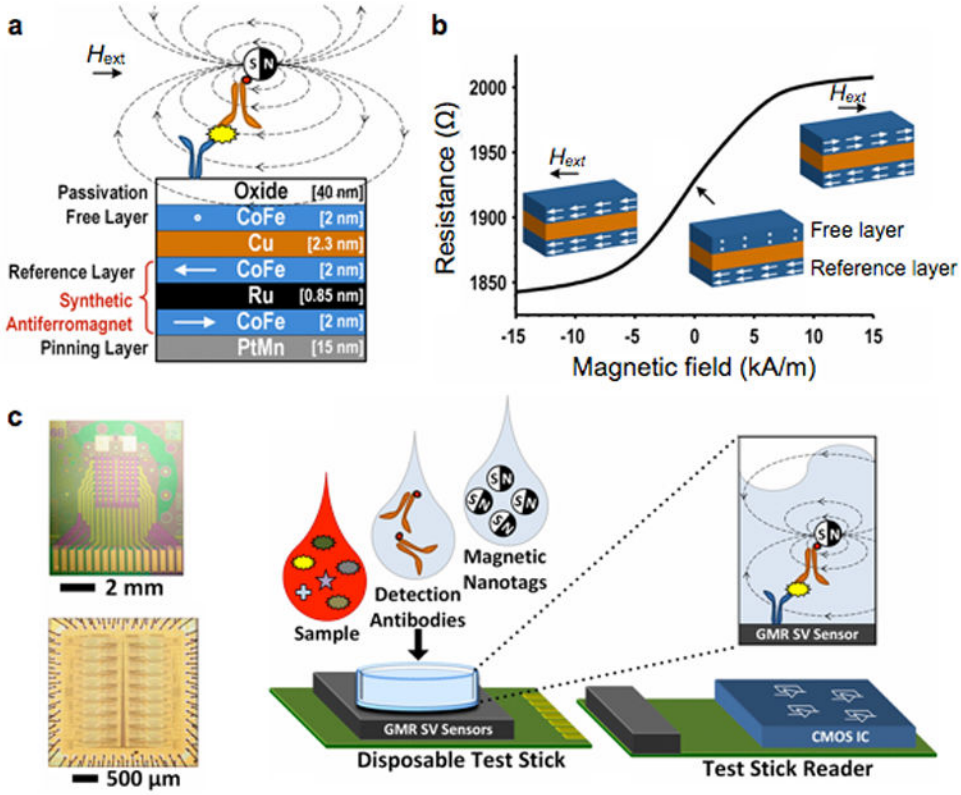

Figure 4. Giant magnetoresistance (GMR) magnetometer

(a) GMR sensors have multiple layers of magnetic and non-magnetic materials. The magnetization of a reference layer is fixed through indirect exchange coupling in the synthetic antiferromagnet. The magnetization of the free layer, however, can rotate in response to the external magnetic field strength (H_{ext}). **(b)** Due to the spin-dependent electron scattering, the electrical resistance of a GMR sensor changes as a function of the relative magnetization angle between the free and the reference layers. **(c)** An array of 256 GMR sensors (top) and its interface CMOS chip (bottom) were separately fabricated. The GMR sensor was mounted on a disposable test stick, and interfaces with the stick reader. A sandwich assay was used to detect protein markers. CMOS, complementary metal-oxide-semiconductor. Reproduced with permission from Ref. 59. Copyright 2013 IEEE.

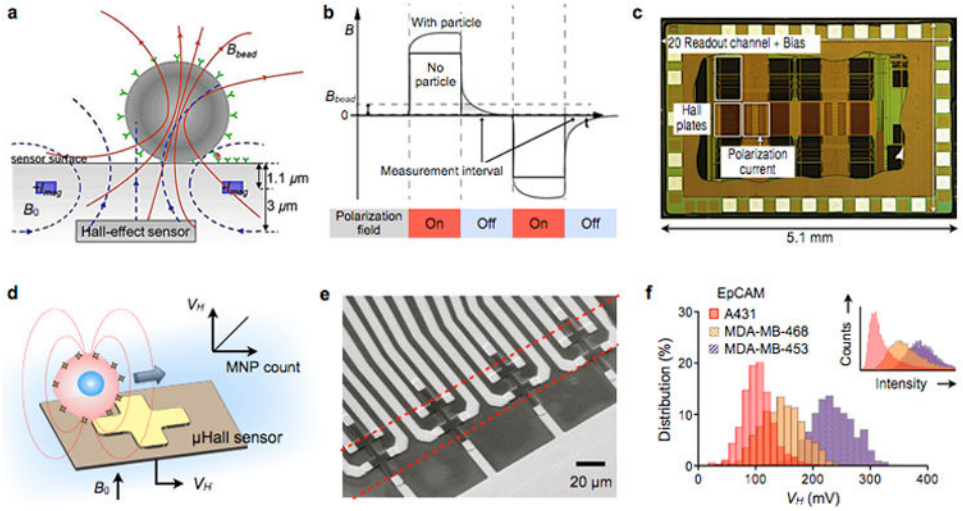

Figure 5. Hall magnetometer

Two types of Hall sensor operation are illustrated. **(a)** Detection of stationary magnetic beads. A pair of metal wires on both sides of the Hall-effect sensor are used to generate the polarizing field (B_0) that magnetizes the magnetic bead. The magnetic field emanating from the bead is measured. $\pm I_{mag}$, electrical currents to generate B_0. **(b)** The beads are detected via relaxation measurement to eliminate the large offset coming from the polarizing field. The polarization magnetic field is applied, and then switched off. Subsequently, the remnant decaying magnetic field (B_{bead}) from the bead is detected by the Hall sensor. **(c)** Die photograph of a Hall sensor integrate circuit (IC). The chip contains 10240 Hall-effect sensors, control electronics, and electromagnets for polarizing field generation. **(d)** MicroHall (μHall) sensor for single cell detection in flow condition. Each cell, targeted with MNPs, generates magnetic fields that are detected by the μHall sensor. The Hall voltage (V_H) is proportional to the MNP counts. B_0, external magnetic field. **(e)** Eight μHall sensors are arranged into an overlapping 2 × 4 array across the fluidic channel width. The dotted lines indicate the location of the sample flow. **(f)** The μHall system measured the expression levels of epithelial cell adhesion molecule (EpCAM) in different cell lines, which agreed with measurements by flow cytometry (inset). Reproduced with permission from Refs. 68 and 67. Copyright 2012, 2013 IEEE. Reproduced with permission from Ref. 24. Copyright 2012 American Association for the Advancement of Science AAAS.

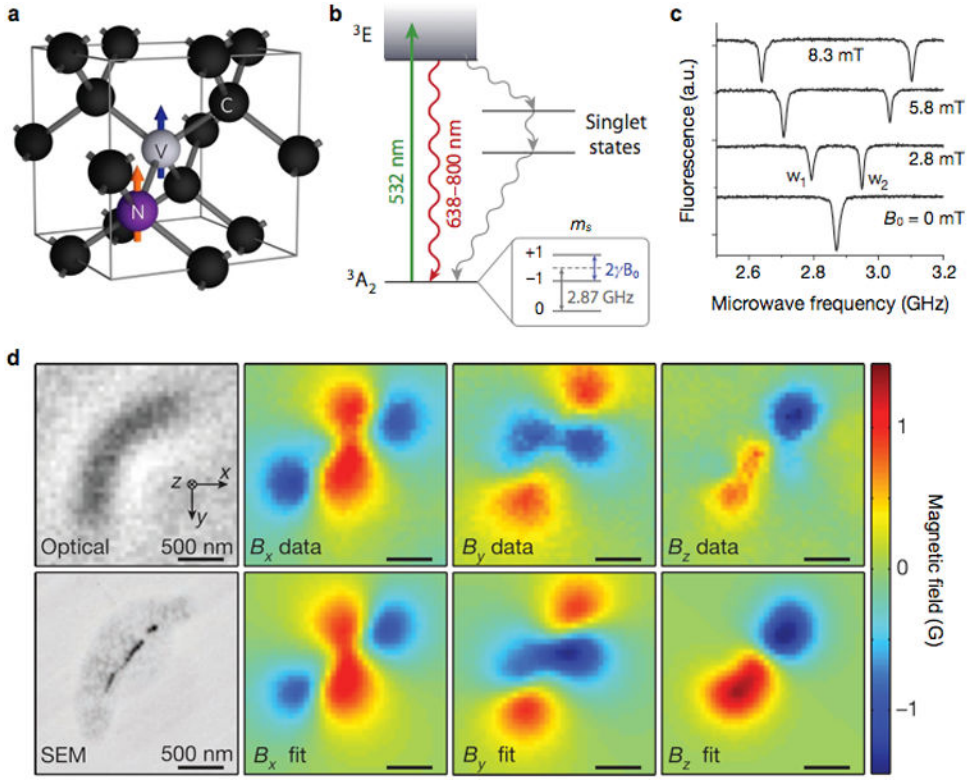

Figure 6. Diamond-based magnetometer

(a) Structure of nitrogen (N) and vacancy (*V*) inside a diamond lattice. C, carbon. The blue and orange arrows indicate the electron and nitrogen nuclear spins, respectively. **(b)** Energy state diagram. The N-*V* center has a spin-triplet ground state ($^3A_2$) with a 2.87 GHz zero-field splitting between the $m_s = 0$ and $m_s = \pm 1$ spin states. Optical excitation (532 nm) produces the excitation state (^3E) which decays back to the ground state by emitting a photon (638–800 nm wavelength). The $m_s = 0$ spin state has a stronger fluorescence than the $m_s = \pm 1$ states, because the $m_s = \pm 1$ excited states also decay non-radiatively via metastable singlet states. When an external field (B_0) is applied, the $m_s = \pm 1$ states are split by $2\gamma B_0$, where γ is the gyromagnetic ratio of the N-*V* electronic spin. **(c)** Optically detected magnetic resonance spectra for a single nitrogen-vacancy. The splitting between w_1 and w_2 is linearly proportional to B_0. **(d)** Detection of magnetotactic bacteria with a N-*V* diamond sensor. Left top and bottom images are from optical and scanning electron microscopy (SEM), respectively. Measured magnetic field projections of the bacterium along the x (B_x), y (B_y) and z axes (B_z) are shown in the top row. The bottom row shows simulated magnetic field projections, assuming that MNP locations match those in the SEM image. Reproduced with permission from Refs. 73, 70, and 75. Copyright 2008, 2012, 2013 Nature Publishing Group.

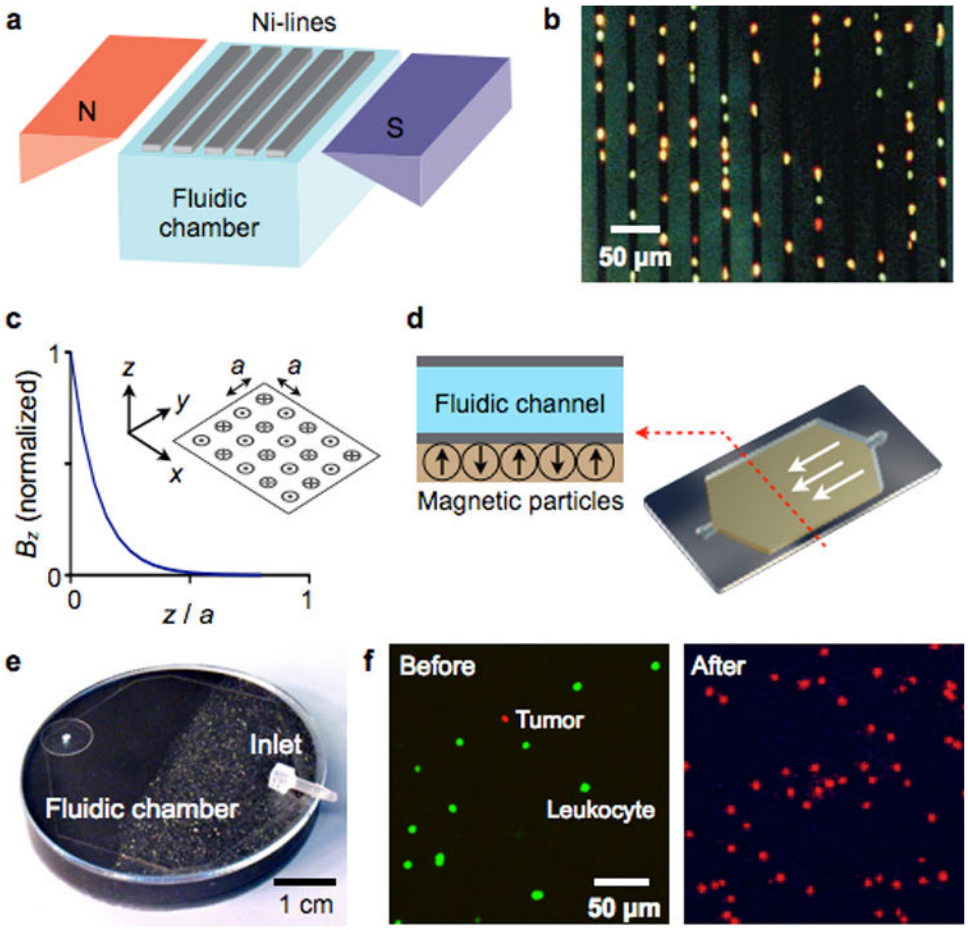

Figure 7. Magnetic retention devices

(a) Magnetic wire system. The separation chamber is optically transparent, but has ferromagnetic lines of nickel (Ni) deposited by lithography. The spacing between these lines is approximately the diameter of one white blood cell. When the chamber is placed between two angular-shaped magnets, the field gradients from the external magnets force the magnetically labeled cells upward to the top of the chamber. When the cells are in close proximity to Ni line, they are subjected to a high local gradient induced by the Ni lines. **(b)** The device in (a) was used to capture leukocytes that were labeled with CD45-specific MNPs. Because cells are aligned on the edge of Ni lines and counterstained with acridine orange, they can be easily observed by a microscope. **(c)** Alternating magnetic dipoles. This configuration creates magnetic fields that are tightly confined on the device surface. **(d)** When magnetic materials are allowed to self-assemble, the magnetic moments align into a similar pattern as in (c). The magnetic structure can easily cover the entire fluidic path to increase the throughput and the capturing efficiency. **(e)** A prototype device was implemented, that consisted of self-assembled layers of 125 μm grain (close to inlet) and 8 μm grain of NdFeB powder. **(f)** A suspension of leukocytes (stained green) and tumor cells were incubated with a mixture of magnetic beads conjugated with anti-CD45 antibodies and fluorescent antibodies against the tumor (anti-HER2/*neu*). The suspension was then flown through the magnetic device shown in (e). Fluorescence micrographs show the enrichment

of tumor cells after the negative selection of leukocytes. The initial concentration of tumor cells to leukocytes was 1:10. Reproduced with permission from Ref. 90. Copyright 1999 Nature Publishing Group. Reproduced with permission from Ref. 97. Copyright 2011 RSC Publishing.

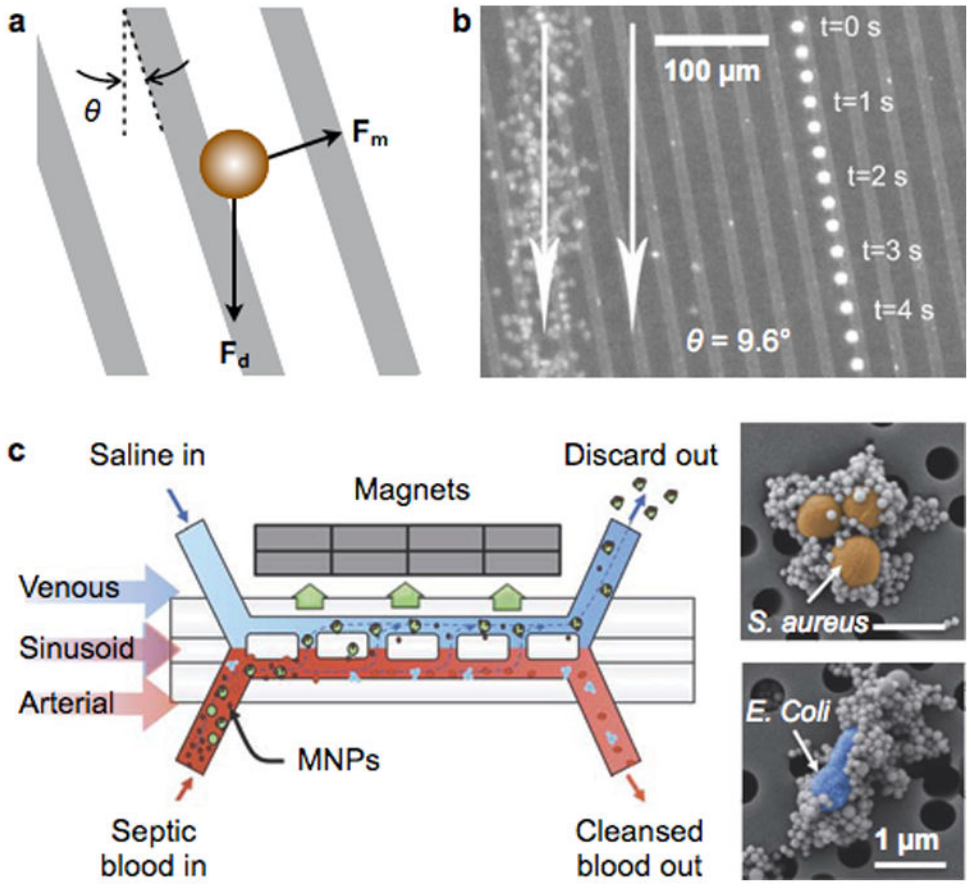

Figure 8. In-flow magnetic separation devices

(a) An array of magnetic lines are used to divert the trajectory of magnetic objects in flow. The magnetic lines are magnetized out of plane, and aligned at an angle θ with respect to the flow direction. The net force on the object is the vector sum of the in-plane magnetic force ($\mathbf{F_m}$) and the fluid drag force ($\mathbf{F_d}$). **(b)** Time lapse image showing a single magnetically-tagged leukocyte. Red blood cells on the left are from a single image. The leukocyte tracks a magnetic line oriented at an angle of 9.6° to the fluidic flow (white arrow). **(c)** A two-channel microfluidic device to separate MNP-labeled bacteria in blood, mimicking the spleen structure. The device mimics the structure of the spleen by incorporating a high-flow vascular arterial channel interconnected by open slits to a parallel low- or intermittent-flow venous sinusoid channel. Magnetic particles are mixed with blood sample to label pathogens (inset), and the mixture is introduced to the arterial channel. Reprinted with permission from Ref. 86. Copyright 2004 American Institute of Physics. Reprinted with permission from Ref. 100. Copyright 2014 Nature Publishing Group.

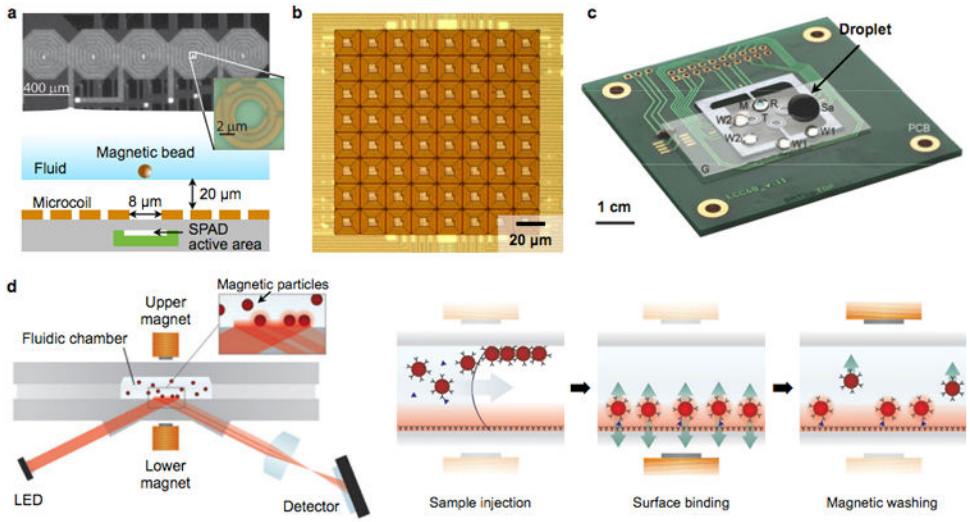

Figure 9. Magnetic manipulator

(a) A linear array of microcoils are implemented in a CMOS chip. Underneath the center of each coil, a single-photon-avalanche diode (SPAD, inset) is placed to detect magnetic beads. Using the combined actuation of adjacent coils, a single bead can be positioned over a SPAD. **(b)** A two dimensional matrix of microcoils is integrated in a CMOS chip along with current sources and control electronics. Through dynamic control of electrical current in each coil, versatile magnetic field patterns can be created to trap and move magnetic objects at micrometer resolutions. **(c)** Magnetic droplet system. A droplet (Sa, 100 μl) containing biological specimen, magnetic particles and reagents, is manipulated by a permanent magnet (M). The droplet goes though a series of mixing, splitting, merging and washing processes to extract RNA from virus. Target RNA is then amplified on chip via RT-PCR. PCB, printed circuit board; G, perfluorinated glass substrate; T, (one of four donut-shaped) miniaturized thermocycler; W1 and W2, washing solution; R, RT-PCR mixture covered by mineral oil. **(d)** Magnetic actuation is exploited to facilitate diagnostic assays. (Left) A fluidic reaction chamber is placed between a pair of electromagnets. A sandwich-type immunoassay with magnetic particles are performed, and the analytical signal is optically readout. (Right) Assay procedure. By sequentially actuating the electromagnets, the immunomagnetic particles are concentrated to the sensor surface for binding, and excess and weakly-bound particles are removed. Reprinted with permission from Ref. 80. Copyright 2010 American Chemical Society. Reprinted with permission from Ref. 102. Copyright 2007 RSC Publishing. Reprinted with permission from Ref. 104. Copyright 2007 Nature Publishing Group. Reprinted with permission from Ref. 108. Copyright 2009 RSC Publishing.

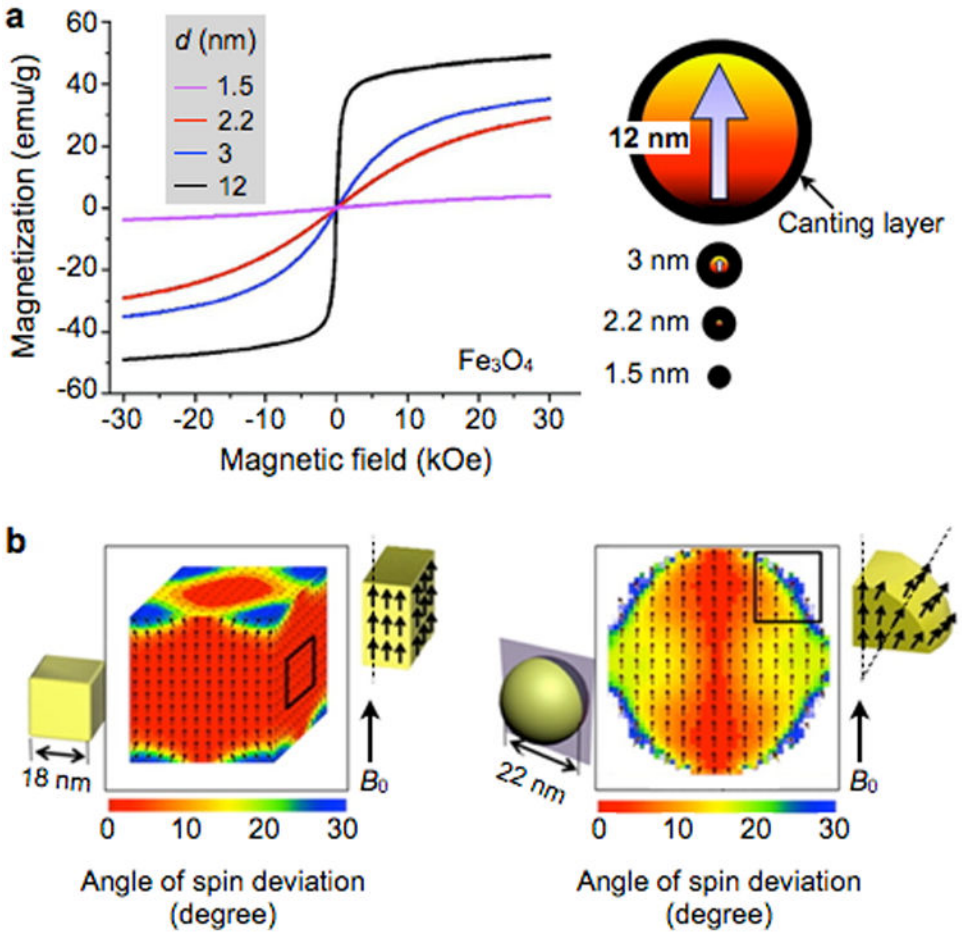

Figure 10. Size and shape dependent magnetization

(a) As the particle size increases, the relative effect of canted spins on the particle surface decreases, which results in an increase of net magnetization. The thickness of the scanted spin layer is ~0.9 nm for spherical Fe_3O_4 MNPs. **(b)** Cubic MNPs assume higher saturation magnetization than spherical particles, because the cubic geometry allows more spins to align in the same direction of the applied magnetic fields. Reproduced with permission from Refs. 111 and 114. Copyright 2011 2012 American Chemical Society.

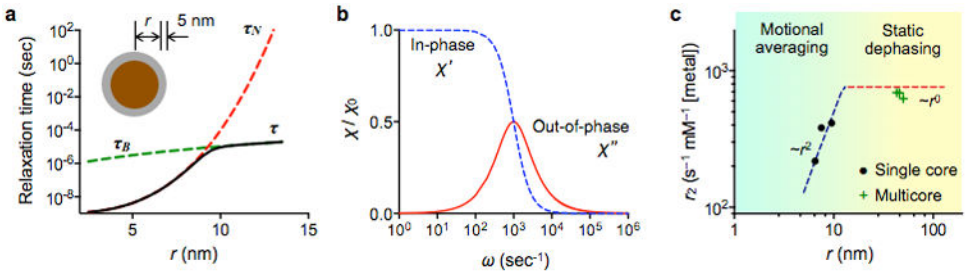

Figure 11. Different magnetic relaxation modes

(a) An ensemble MNPs in solution can lose net magnetic moments through Neel and Brownian relaxation mechanisms. The Neel relaxation, namely the spontaneous flipping of magnetic moments inside a particle, is dominant for small MNPs. The Brown relaxation, caused by the physical rotation of particles, takes over as the particle size increases. Shown here are the Neel (τ_N) and the Brownian (τ_B) relaxation times calculated for Fe_3O4 MNPs with 5-nm surface coating. The effective relaxation time (τ) can be obtained from $1/\tau_N = 1/\tau_N + 1/\tau_B$. **(b)** The alternating current (AC) magnetic susceptibility has two components, the in-phase and the 90° out-of-phase with respect to the AC excitation source. The out-of-phase component has its maximum when the excitation frequency is close to the relaxation time of the particle. **(c)** In the NMR detection, MNPs accelerate the transverse relaxation of ^1H signal. The transverse relaxivity (r_2) is the capacity of MNPs to shorten the transverse relaxation time. The r_2 values of single and multicore $MnFe_2O_4$ MNPs were measured. While the r_2 values of single core MNPs increased steeply with increasing particle size ($\sim r^2$), the r_2 values for multicore MNPs showed little dependence on particle size ($\sim r^0$). Theoretical modeling, based on motional averaging and static dephasing, accurately describes the observed r_2-behavior (dotted lines): due to their small particle size, single-core MNPs are in the motional averaging regime (blue line), whereas multicore MNPs fall into the static dephasing regime (horizontal red line).

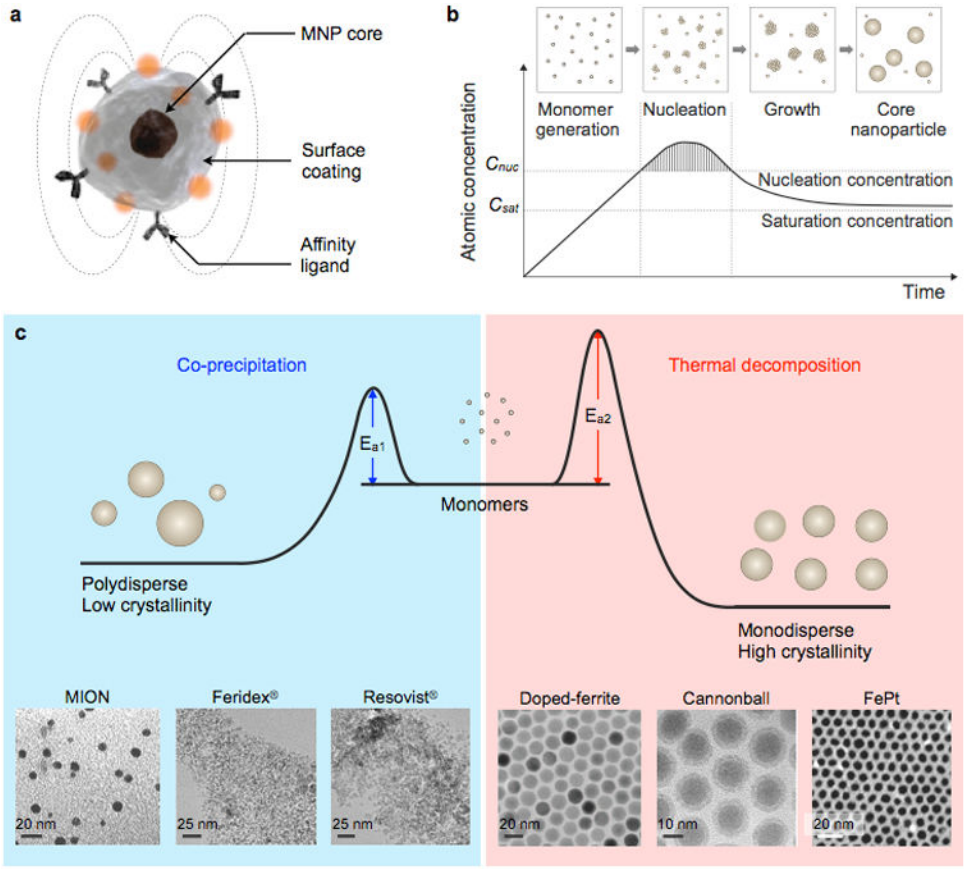

Figure 12. Synthesis of Core MNPs

(a) Representative structure of a MNP. **(b)** Crystal-growth diagram. When the monomers are supersaturated and exceed the nucleation concentration, seed nucleation is induced and monomers are continuously aggregated onto the seeds, leading to crystal growth. C_{nuc}, nucleation concentration; C_{sat}, saturation concentration. **(c)** Comparison of co-precipitation and non-hydrolytic thermal decomposition methods. The co-precipitation method results in kinetically favored MNPs which generally have a polydisperse size and relatively low crystallinity. Conversely, the thermal decomposition method produces thermodynamically stable MNPs with a monodisperse size and high crystallinity.Examples of transmission electron microscope (TEM) images of MNPs synthesized by co-precipitation (MION, Feridex®, Resovist®) or thermal decomposition methods (Doped-ferrite, Cannonball, FePt) are shown. Reprinted with permission from Ref. 155. Copyright 2014 Nature Publishing Group. Reprinted with permission from Ref. 175. Copyright 2012 American Institute of Physics. Reprinted with permission from Ref. 216. Copyright 2004 American Chemical Society.

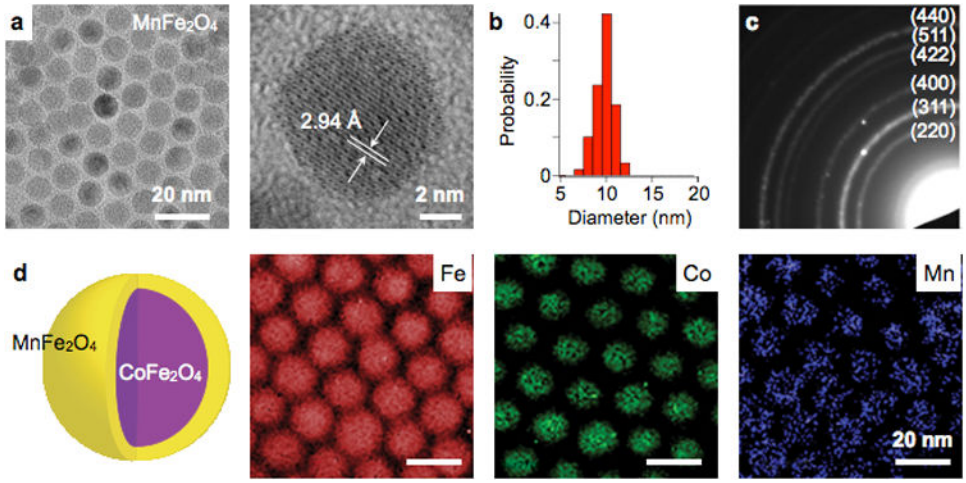

Figure 13. MNP analysis by TEM

(a) TEM imaging allows for fast assessment of particle shape (magnetic core), down to the atomic length scale. A crystal lattice plane of a ferrite MNP is shown. **(b)** Size distribution of particles in (a) were obtained. **(c)** In the diffraction mode, TEM can be used to display the reciprocal lattice pattern. Shown here is the electron diffraction pattern of $MnFe_2O_4$ MNPs. Concentric ring patterns corresponding to the spinel structure are identified. **(d)** By scanning the electron beam and performing spectroscopic measurements, the composition of particles can be mapped. The element of $CoFe_2O_4$ (core) / $MnFe_2O_4$ (shell) MNPs were imaged using the electron energy loss spectroscopy (EELS) method. Reproduced with permission from Ref. 44. Copyright 2009 National Academy of Sciences, USA. Reproduced with permission from Ref. 217. Copyright 2011 Nature Publishing Group.

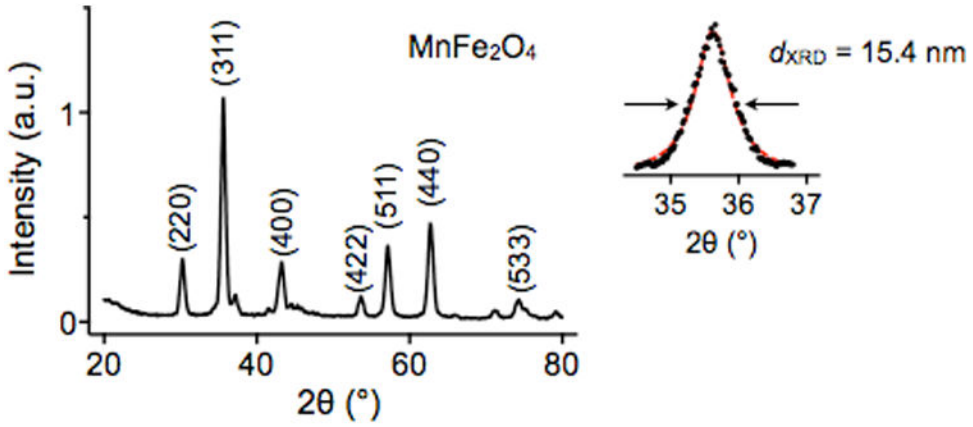

Figure 14. Structural analysis by X-ray diffraction (XRD)

By scanning the incident angle (θ) of an X-ray beam and using powdered MNPs, the diffraction peaks of different lattice planes are measured. A diffraction pattern from powdered $MnFe_2O_4$ MNPs is shown, which confirms to that of a typical spinel structure of ferrite. The crystal size is also estimated by fitting the major peaks (311) to Scherrer's formula. Reproduced with permission from Ref. 44. Copyright 2009 National Academy of Sciences, USA.

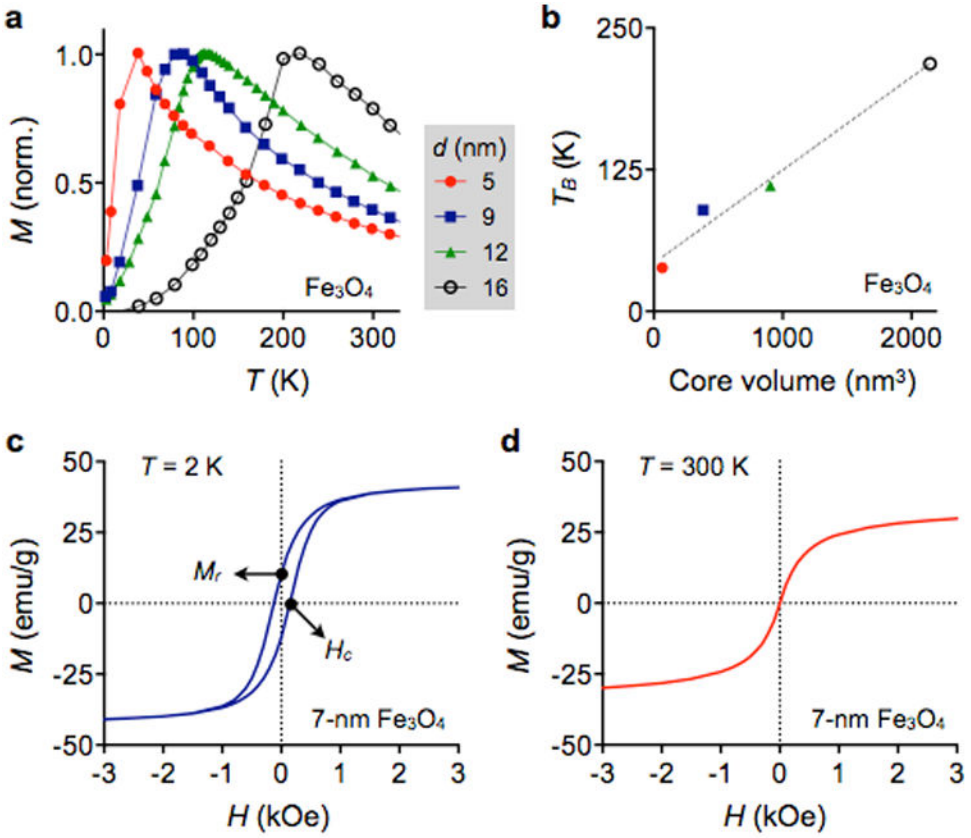

Figure 15. Magnetic characterization

(a) Temperature-dependent magnetization curves $M(T)$ of differently sized Fe_3O_4 MNPs are shown. The temperature at which M has its maximum is defined as the blocking temperature (T_B). When $T < T_B$, the magnetization increases with T, because thermal energy helps magnetic domains to rotate and align with the external magnetic fields. When $T > T_B$, thermal energy is large enough to cause random fluctuations of magnetic domains, which leads to a decrease of M. **(b)** T_B from (a) is plotted against the core volume. T_B for a given material is generally proportional to the particle volume, because the anisotropy energy barrier scales with the particle volume. **(c)** Field-dependent magnetization $M(H)$. Below the blocking temperature, MNPs display hysteresis in response to the applied magnetic field (H). The non-zero magnetization at $H = 0$ is called remanence (M_r), and the field strength to reduce $M = 0$ is defined as coercivity (H_c). **(d)** MNPs in a superparamagnetic state displays negligible M_r and H_c. The M value monotonically increases with H as in paramagnetic material. Reproduced with permission from Ref. Copyright 2004 Nature Publishing Group.

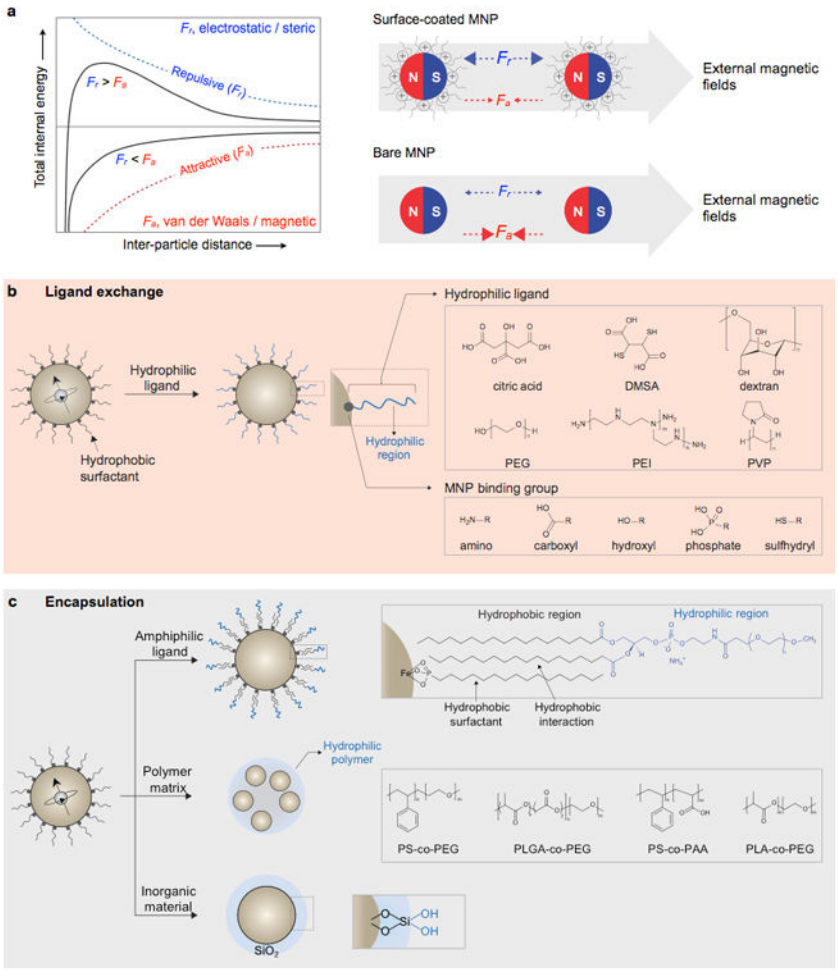

Figure 16. Surface modification methods for thermally grown MNPs

(a) Total interaction energy between two MNPs as a function of the inter-particle distance. The stability of MNPs results from the equilibrium between attractive (F_a: van der Waals and magnetic dipolar) and repulsive (F_r: electrostatic and steric) forces. Surface-coated MNPs are stabilized with electrostatic and steric repulsion provided by coating materials, while bare MNPs are aggregated. **(b)** Schematic illustration of ligand exchange. Hydrophobic surfactants of MNPs are replaced with hydrophilic ligands, which consist of an MNP binding group and hydrophilic region. Grey-lined boxes show several examples of hydrophilic ligands and MNP binding functional groups. DMSA, dimercaptosuccinic acid; PEG, polyethylene glycol; PEI, polyethyleneimine; and PVP, polyvinylpyrrolidone. **(c)** Schematic illustration of MNP encapsulation strategies. Hydrophobic MNPs are made hydrophilic by encapsulation with an amphiphilic ligand, embedding in polymer matrix, or coating with an inorganic material. Amphiphilic ligands possess hydrophobic and hydrophilic regions. The hydrophobic chains are intercalated into the layer of hydrophobic surfactants through hydrophobic interaction, while the hydrophilic regions interact with aqueous solution (grey-lined box, top). Several polymers are utilized as a hydrophilic matrix for MNP embedding. PS-co-PEG, polystyrene-co-PEG; PLGA-co-PEG, poly(lactic-co-glycolic acid)-co-PEG; PS-co-PAA, polystyrene-co-poly(acrylic acid); and PLA-co-PEG,

poly(lactic acid)-co-PEG(grey-lined box, middle). Hydrophilic silanol groups (Si-OH) on the SiO_2 surface make silica-coated MNPs water-soluble (grey-lined box, bottom).

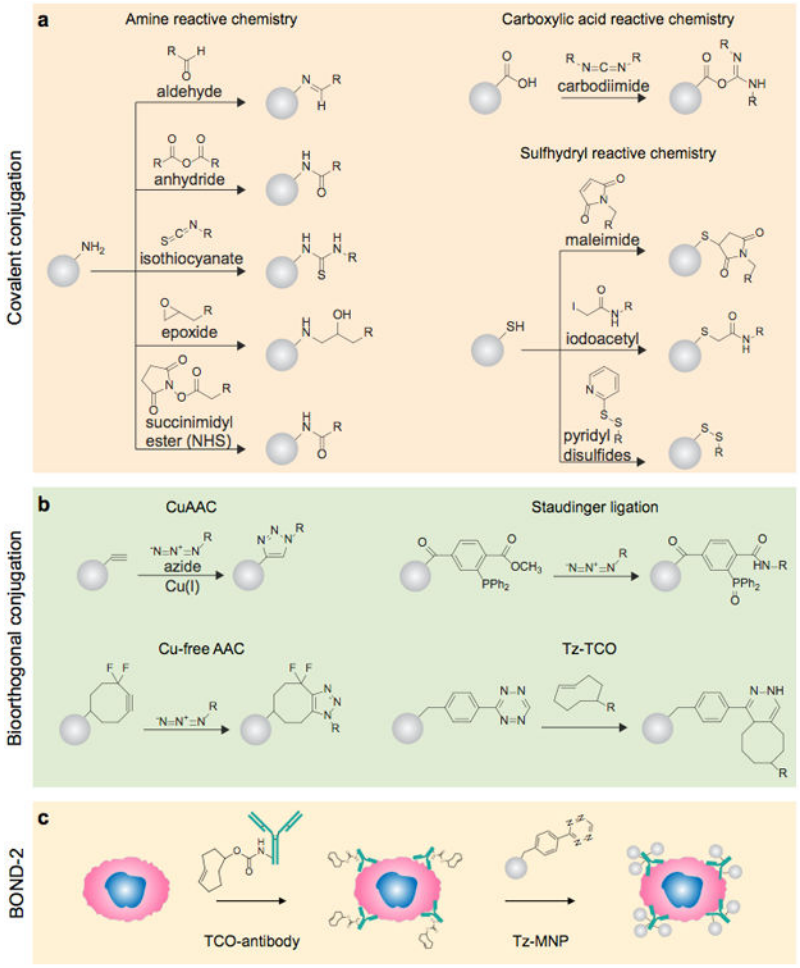

Figure 17. MNP surface conjugation chemistries

(a) Schematic illustration of covalent conjugation strategies, including amine, carboxylic acid, and sulfhydryl reactive chemistries. **(b)** Representative bioorthogonal covalent conjugation chemistries. CuAAC, Cu(I)-mediated [3 + 2] azide-alkyne cycloaddition; Tz, teterazine; and TCO, trans-cyclooctene. **(c)** The schematics of the bioorthogonal nanoparticle detection (BOND) technique, which utilizes Tz-TCO cycloaddition as the conjugation mechanism. Antibodies are modified with TCO and used as scaffolds to label more Tz modified MNPs onto target cells.

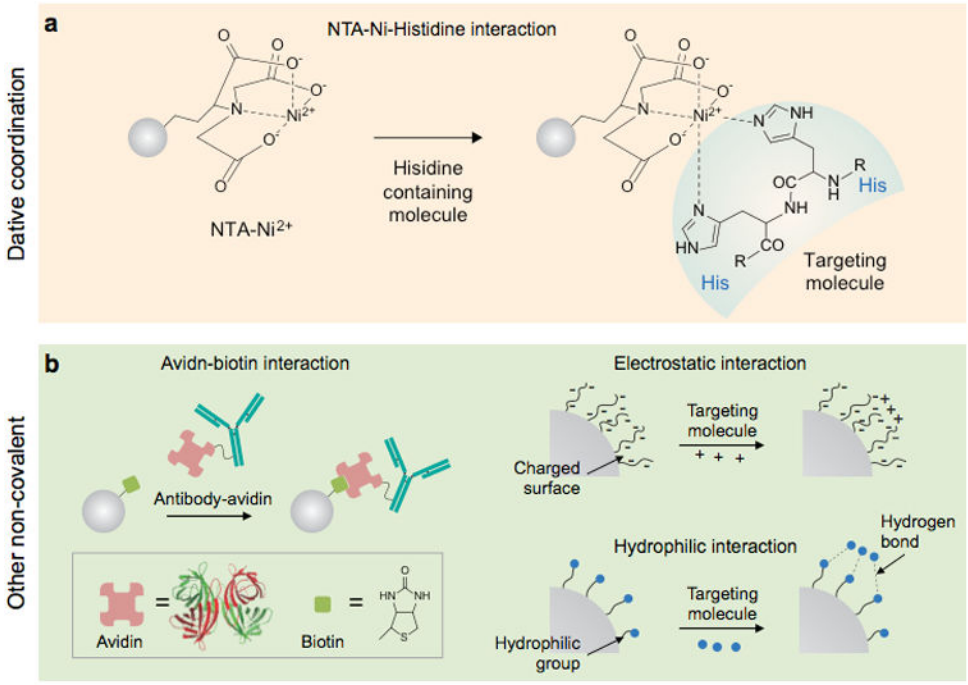

Figure 18. Alternative MNP surface conjugation chemistries

(a) Example of representative dative coordination binding. **(b)** Schematic illustration of non-covalent conjugation commonly used for bioconjugation.

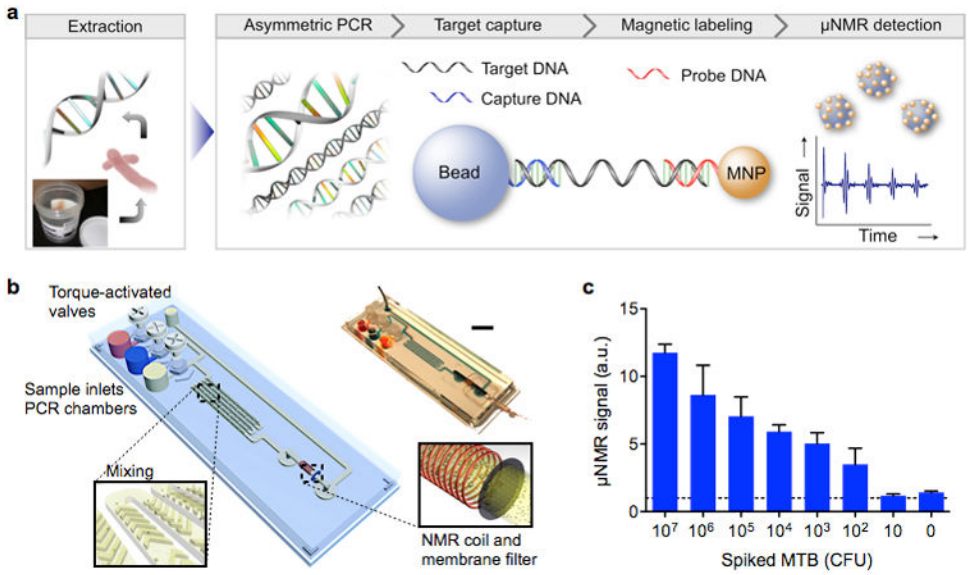

Figure 19. Magnetic barcode assay for bacterial detection

(a) Assay procedure. From unprocessed specimen, bacterial 16sRNA or DNA is extracted though an off-chip stressing. Extracted DNA samples are then loaded into a fluidic device. The target DNA sequences are amplified by asymmetric RT-PCR and captured by polymer beads modified with capture DNA. MNPs are then used to specifically coat the beads via complementary sequences, and the samples are subjected to NMR measurements. **(b)** A fluidic cartridge was developed to streamline the assay. The device integrates PCR chambers, mixing channels and a microcoil for NMR measurements. **(c)** *Mycobacterium tuberculosis* targets in sputum samples were detected. The sensitivity was 10^2 – 10^3 CFU/mL. CFU, colony forming unit. Reproduced with permission from Ref. 52. Copyright 2013 Nature Publishing Group.

Table 1

Comparison of magnetic sensors.

Mode	Sensor type	Key MNP requirement	Detection limit	Disease detection (demonstrated)	Note	Commercial partner
Volumetric detection	μNMR	• High transverse relaxivity	• Single bacterium • ~10 mammalian cells • ~10 pM proteins	• Cancer • Infection • Metabolic disorders	• Versatile • Portable device or desktop system	T2BioSystems
	Magnetic susceptometer	• Brownian relaxation • Colloidal stability • Monodispersity	• ~1 pM DNA (PCR-amplified)	• Infection	• Limited to soluble targets • Low sensitivity • Desktop system	DynoMag
Surface sensor	GMR	• High magnetic moment • Colloidal stability	• ~5 fM proteins	• Cancer • Cardiovascular disease	• Limited to soluble targets • Portable device	MagArray
	μHall	• High magnetic moment	• Single cell • Single bacterium	• Cancer • Infection	• CMOS compatible • Lower sensitivity than GMR • Poratble device	
	NV-diamond	• High magnetic moment	• Single MNP	• Cancer • Infection	• Highest sensitivity • Exploratory phase • Desktop system	
Magnetic actuation	Optical sensor	• High magnetic moment	• ~1 pM proteins	• Controlled substance • Cardiovascular disease	• Limited to soluble targets	Philips

Mode	Sensor type	Key MNP requirement	Detection limit	Disease detection (demonstrated)	Note	Commercial partner
					• Portable device	

Table 2

Magnetic properties of selected magnetic crystals

Material	Saturation magnetization ($kA \cdot m^{-1}$)[a]	Anisotropy constant ($kJ \cdot m^{-3}$)[b]	d_{sp} (nm)[c]
Fe	1752	42	17
Co	1446	410	8
Ni	510	-5.8	32
Fe_3O_4	510	-11	26
$CoFe_2O_4$	475	180	10
$MnFe_2O_4$	560	-2.8	41
$NiFe_2O_4$	300	-5.1	33

[a] Bulk values at $T = 0$ K. Adopted from Ref. [109].

[b] The first order anisotropy constant at room temperature. Adopted from Ref. [118].

[c] Calculated maximum diameter for spherical superparamagnetic MNPs.